Single Electron Spin Detection at Millikelvin Temperatures: Requirements and Setup Improvements

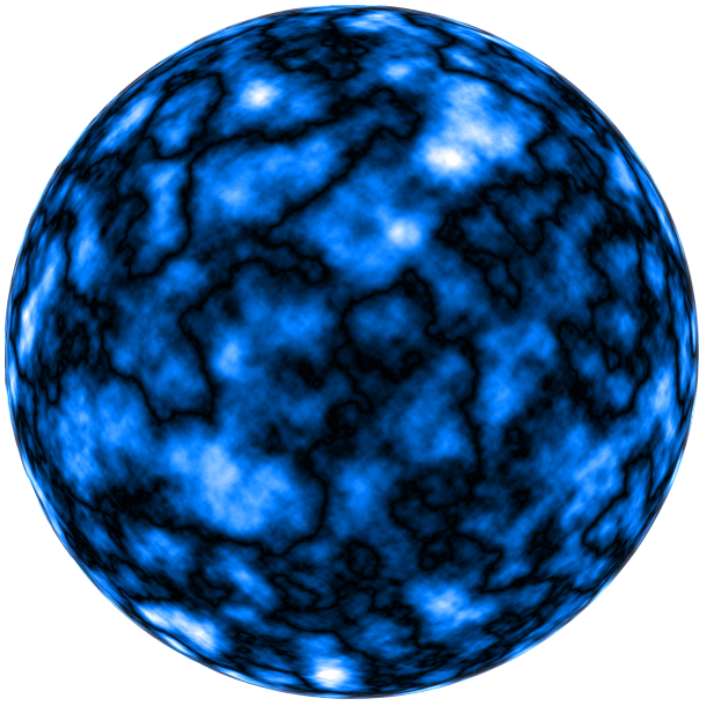

THESIS

submitted in partial fulfillment of the
requirements for the degree of

MASTER OF SCIENCE
in
PHYSICS

Author :	Timothy van den Berg
Student ID :	s1530666
Supervisor :	Prof. dr. ir. Tjerk Oosterkamp
2^{nd} corrector :	dr. Martina Huber

Leiden, The Netherlands, June 15, 2020

Single Electron Spin Detection at Millikelvin Temperatures: Requirements and Setup Improvements

Timothy van den Berg

Huygens-Kamerlingh Onnes Laboratory, Leiden University
P.O. Box 9500, 2300 RA Leiden, The Netherlands

June 15, 2020

Abstract

Magnetic resonance force microscopy (MRFM) is a scanning probe technique capable of producing three-dimensional images with nanometer-scale spatial resolution. MRFM relies on the mechanical detection of a weak and oscillating magnetic force between a tip magnet attached to a high compliance cantilever and magnetic moments. Measuring a single electron spin (abbreviated as single-spin) would open the way towards a macroscopic spin-cantilever superposition and three-dimensional images of molecular complexes, e.g. protein structure, with angstrom precision.
Although single-spin detection has already been accomplished at 1.6 K, we aim to repeat this feat at millikelvin temperatures to achieve an improved force sensitivity and reduced thermal noise. In this thesis we report on the requirements a setup has to satisfy to enable the detection of an individual spin at millikelvin temperatures. These conditions are drastically more stringent compared to the prerequisites of single-spin detection at a temperature of several kelvin. Moreover, it turned out that our setup does not meet the criteria so we studied several technical enhancements that bring single-spin detection within reach, such as a sample with a lower spin density, nanometer-scale probe magnets and nanometer-sized cantilevers. Provided that these improvements are implemented successfully, detection of an individual spin at millikelvin temperatures appears to be feasible.
Furthermore, we present several test experiments with a novel piezoelectric based vibration isolation device. This damping apparatus was designed to actively reduce the level of environmental vibrations near the sample stage, which is required to be ultra-low to achieve a sufficiently large superposition to measure a visible interference.

Contents

Chapter 1

Magnetic Resonance Force Microscopy

Prologue to the Chapter

Most measurement techniques are exposed to an unfulfilled drive to improve the sensitivity and reduce the noise. The history of the development of MRFM[1–7] followed a similar path that eventually led to the first recorded single electron spin detection,[8] performed at 1.6 K. The ability to observe a single spin signal opens up the way towards exciting and long awaited applications, such as unravelling the structure of molecules and sub-surface imaging with angstrom precision. The feasibility of this breakthrough prompted us to try to repeat this feat at millikelvin temperatures to obtain a better sensitivity and to lower the noise levels. This has proven to be significantly more challenging, since it requires several drastic changes to our apparatus that have far-reaching consequences. A more detailed discussion about the crucial differences between our setup and the standard detection scheme wield in all other MRFM apparatuses is presented in Sec. 1.3.
Despite considerable effort and progression made by multiple people over the course of several years it is still unknown whether a single electron spin measurement is feasible at millikelvin temperatures and what the requisite conditions are. For this reason, this thesis is devoted to set up the requirements for single-spin detection at millikelvin temperatures and to explore whether this feat is achievable. We shed light on a broad range of topics and also examine a few setup improvements that, if implemented successfully, are a significant step towards the main goal.

Before we dive into a feasibility study of single-spin detection, an introduction to the used technique, MRFM, is presented. As such, the purpose of this chapter is to review the essential principles of MRFM, discuss its capabilities with respect to competing methods and cover some of the basic concepts required as foundation for the following chapters. Specific emphasises is placed on the quantum mechanics of a single-spin measurement, because this cannot be omitted in any serious analysis involving single electrons.

The different topics are presented in the following order:

1) *Motivation*
2) *Principles of MRFM*
3) *Setup essentials*
4) *Comparison among high-resolution techniques*

5) *Quantum mechanism of MRFM*

6) *Thesis outline*

An explanation in richer detail of our detection scheme, isolation vibration design and sample preparation is presented in dissertations of various predecessors.[9–13] Here we only discuss the necessary elements for the purpose of understanding the storyline of this thesis.

1.1 Motivation

MRFM was proposed by Sidles in 1991[1] to fulfill the biological need of an imaging technique with nanometer-scale precision. The realization of MRFM happened the following year[14] with the detection of electron spin magnetic resonance and soon after nuclear signal was measured.[15] The rapid progress in the first decade after Sidles's proposal eventually led to the momentous first single-spin detection by Rugar and coworkers.[8] This was shortly followed by another astounding milestone, namely, the image of proton spins inside an individual tobacco mosaic virus with a spatial resolution below ten nanometer.[16]
Recent advancements have slowed down as it took another ten years to improve the resolution to sub-nanometer length-scales.[17] Even though the initial goal, a microscope to image molecular structures, has not yet been achieved, the development of MRFM has led to various new research directions. A selection includes several studied spin phenomena, such as relaxation times,[18–20] spin noise,[21] spin diffusion[22–24] and manipulation of spins in the Boltzmann or statistical regime.[25–28] Other investigations were focused on ferromagnetic resonance[29–32] or paramagnetic resonance.[33,34]
Research in the Oosterkamp group has shifted from medical-driven experiments towards condensed matter applications. A long standing goal within our group is achieving a mechanical spin-resonator superposition (see the prologue to chapter 4 for more details). To this end, it is necessary to be able to unambiguously collect and isolate the signal from a single electron spin. Due to its roughly 660 times smaller gyromagnetic ratio than electrons, directly measuring single ^1H spins or other nuclei spins is significantly more difficult.

1.2 Principles of magnetic resonance force microscopy

Sidles devised MRFM as a combination of nuclear magnetic resonance (NMR)[35,36] and atomic force microscopy (AFM).[37,38] The resolution of AFM and the measurement technique of NMR result in a magnetic resonance based force microscope, which in theory is capable of imaging with atomic-scale precision. The present day spatial resolution records stand at 0.9 nm in one dimension[17] and 4 nm in three dimensions,[16] respectively. In case electrons are studied it is called electron spin resonance (ESR), which is based on the same principles as NMR.
In this section we review the basic principles of MRFM without assuming prior knowledge. The theory of MRFM is built up starting from NMR and thereafter we review the two methods to obtain a signal, i.e. a force or a force-gradient approach.

1.2.1 From nuclear magnetic resonance...

For convenience, let us consider a sample in thermal equilibrium consisting of spin-$\frac{1}{2}$ particles. The spin states corresponding to m = $\frac{1}{2}$ and m = -$\frac{1}{2}$ are degenerate, hence both states are

populated by an equal number of spins. In conventional NMR (or ESR) a large static magnetic field is applied that generates a Zeeman splitting of the spin states. An additional distinct feature of spin behaviour in an external magnetic field is the precession at the Larmor frequency of the spin magnetization in a cone around the magnetic field. Due to the energy difference one state is energetically favorable, which results in the spins being on average aligned along the magnetic field polarization. Subsequently, a perpendicular, weakly oscillating radio frequency (rf) magnetic field perturbs the spin ensemble at a certain frequency. If this frequency is sufficiently close to the Larmor frequency (corresponding to the Zeeman splitting) transitions between the spin states occur. The fluctuating magnetization of the spin ensemble produces a signal that can be observed with a pickup coil, since it induces a current. Consequently, by amplifying the current and using deconvolution techniques, 3D images can be created as is done in magnetic resonance imaging (MRI). The signal strength scales with the amount of spins in the ensemble and their polarization (Sec. 1.2.3). A spatial dependence is included by varying the strength of the static magnetic field across the sample. After the oscillating field is turned off, the spin's magnetization exponentially decays towards equilibrium according to the spin-lattice relaxation time (T_1). For a more detailed discussion of relaxation mechanisms see Sec. 2.1.2.

1.2.2 ...To magnetic resonance force microscopy

The magnetic moments of electrons and nuclei are exceedingly small, hence the magnetic fields they generate are very weak. For this reason on the order of 10^{12} spins are required in NMR to produce a sufficiently large signal.
Bringing down the sensitivity to single spin levels demands a different detection method. In his MRFM proposal, Sidles[1] suggested mechanical detection of magnetic resonance, i.e. force detected NMR, instead of inductive detection as is done in conventional NMR (Fig. 1.1). Both MRFM and NMR are based on the magnetic coupling between a spin and a resonator. The resonator is a mechanical force transducer[1] in MRFM, whereas it is an electrical pickup coil (LC circuit) in NMR. The two cases are mathematically identical[39] and are fully captured by only the resonance frequency (ω_0), quality-factor (Q-factor) and magnetic spring constant (k_m), which is a measure of the potential energy within a system.[2] The signal-to-noise ratio (SNR) is then (see Sec. 3.4.1 for a more detailed discussion on cantilevers)

$$SNR \propto \sqrt{\frac{\omega_0 Q}{k_m}}. \tag{1.1}$$

k_m greatly depends on the dimensions of the cantilever and the generated tip field. Modern fabrication techniques enable the production of cantilevers with incredibly high aspect ratios and Q-factors that exceed 10^4. Even though ω_0 of inductive coils in general exceeds 100 MHz compared to kHz for cantilevers, due to the much higher Q-factor and orders of magnitude lower k_m of cantilevers, the SNR of mechanical detection still greatly surpasses inductive detection schemes.
Intuitively this can be understood by considering the filling factor of coils.[6] Inductive coils require a sufficiently large sample volume to produce a current. This is only realized if the perturbation of the coil's magnetic field by the spins is ample, i.e. if the spin magnetic fields fill up a considerable part of the coil. For increasingly smaller spin ensembles it becomes more difficult to create small enough coils to establish a significant filling factor. The current

[1] In practice the resonator is a high compliance cantilever, i.e. a soft spring, in MRFM.

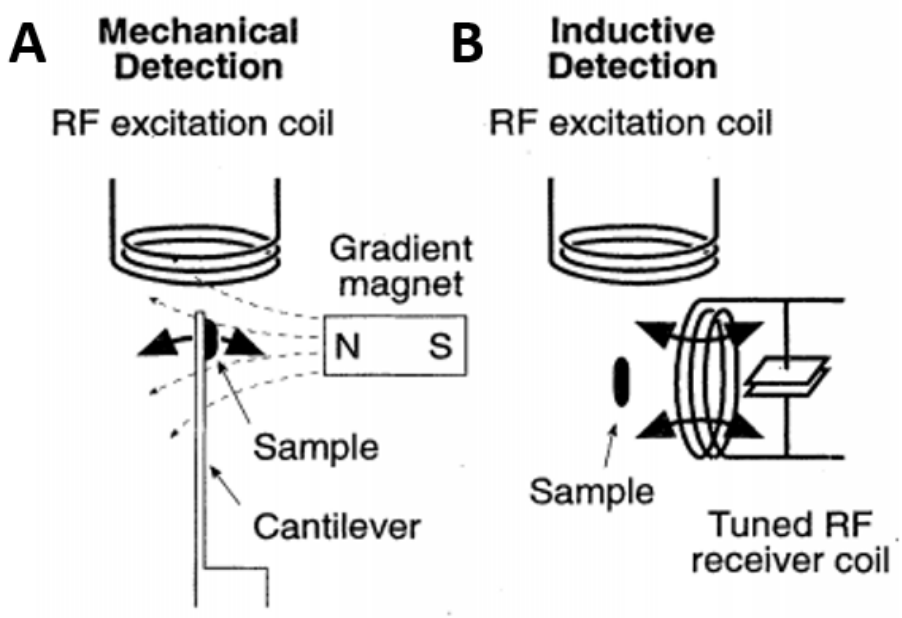

Figure 1.1: *Scheme of mechanical (a) and inductive (b) detection of magnetic resonance as described in the text. In the early days of MRFM a sample-on-tip was the standard, but people soon found that a magnet-on-tip approach is more beneficial due the ability to measure different samples with the same cantilever. Additionally, micro-striplines have replaced the micrometer-sized coils as rf source in present day setups. Since striplines create only local rf fields, the dissipated heat stays far below the cooling power of refrigerators. The price of having highly confined fields is that the rf source has to be in close proximity to the sample, or (as in our case) it has to be mounted directly on the sample. See Fig. 1.2 for modern laser based and SQUID based setups. Figure reprinted from Sidles et al..*[2]

day resolution of inductive NMR is limited at ~3 μm,[40] while medical MRI only reaches ~0.1 mm.
Another effect that explains the extreme SNR of cantilevers is the energy exchange during a period of the oscillating magnetic field.[2] In a coil, the magnetic field is switched on and off twice every cycle, which costs energy. Cantilevers, however, re-locate the field due to vibrations,[2] thereby avoiding the energy conversion of creating and annihilating the field. As a result of technological advancements, state-of-the art cantilevers have sub-micron dimensions (Sec. 3.4.1) that entail much smaller energy conversions than inductive coils.

We continue this section by introducing some concepts that differentiate MRFM from NMR. To do so, we start with a mathematical description of the magnetic interaction in a mechanical fashion, which is derived from the interaction energy[10]

$$E_{int} = -\boldsymbol{\mu} \cdot \mathbf{B}(\mathbf{r}). \tag{1.2}$$

The magnetic moment μ is made bold to indicate that it is a vector. Moreover, since this thesis is focused on electrons: μ = -g$\mu_B \frac{S}{\hbar}$ = 9.28·10^{-24} J/T, where g is the electron spin g-factor, $\mu_B = \frac{e\hbar}{2m_e}$ the Bohr magneton with m_e the electron mass and $\boldsymbol{S}$ is the electron spin angular momentum. For brevity we omit any further specifications throughout this thesis and simply name it μ_s, the electron magnetic moment, or equivalently μ_B.

[2]To ensure energy conservation there is a constant transfer between potential and kinetic energy. The minimal required energy to produce a fluctuating field at the spin location is given by $E_{pot} = \frac{1}{2}k_m B^2$. For comparison, at a field strength of 100 mT, $E_{pot} \simeq 10^{-20}$ J for cantilevers with high-gradient tip magnets and $E_{pot} \simeq 10^{-5}$ J for small coils.[2,3]

The magnetic field B is the sum of a weak, oscillating field (B_1) and a B_0 field, which is typically composed of an external static field and the tip magnetic field. The force is then

$$\mathbf{F} = -\nabla \cdot E_{int} = \mu \nabla \cdot \mathbf{B}. \tag{1.3}$$

Since B_1 is negligibly small and the external field is static, $\nabla \cdot B$ contains only the gradient field of the tip magnet. In practice only the force along the deflection direction is of interest. In this thesis we take x as the cantilever's direction of movement and μ is directed along the z-axis in accordance with literature. The force is then: F = -$\mu \frac{\partial B}{\partial x}$.
Instead of measuring the deflection of the cantilever beam due to incident forces, one could also measure the frequency shift of the natural resonance frequency (force-gradient detection). A position dependence of the force alters the spring constant, which in return changes the resonance frequency. This effect can be described in a simple model by introducing a stiffness k_s that resembles the interaction between a spin and the cantilever. Since k_s is related to F through Hooke's law: $k_s = \mu \frac{\partial^2 B(r)}{\partial x^2}$. Let m and k_0 be the mass and intrinsic spring constant of the cantilever. The resonance frequency f_0 reads then

$$f_0 = \frac{1}{2\pi} \sqrt{\frac{k_0}{m}}. \tag{1.4}$$

Squaring f_0 and taking the derivative with respect to k_0 of f_0^2 results in

$$2 f_0 \Delta f = \frac{1}{4\pi^2} \frac{1}{m} \Delta k. \tag{1.5}$$

By recognizing $\Delta k = k_s$ and dividing Eq. 1.5 by the square of Eq. 1.4 one obtains after doing some algebra

$$\Delta f = \frac{1}{2} \frac{k_s}{k_0} f_0. \tag{1.6}$$

Many effects, e.g. dissipation, spin-spin interactions and cantilever relaxation, are not included in this simplified model. Nonetheless, it is sufficiently close to results from more sophisticated theories in many cases (Sec. 2.2.3.2). Previous mentioned effects will be elaborated in coming sections throughout this thesis. Furthermore, due to its simplicity, the model intuitively shows the important differences between force and force-gradient based measurements. Namely, forces scale with the first gradient of B, while frequency shifts are proportional to the second gradient of B.
In order to detect forces, the sample and magnet have to be in close proximity, i.e. within a μm in our setup. Equivalently to the situation in NMR, an oscillating rf field is switched on that periodically inverts the spins. The spin-flip process results in a fluctuating magnetic force that interacts with the cantilever's magnet. To maximize the force transduction and signal output, the spins are flipped at the cantilever's resonance frequency. The resonance condition is fulfilled in the volume where the following condition holds:

$$\omega_{rf} = \gamma B_0. \tag{1.7}$$

Here, ω_{rf} is the frequency of the B_1 field and γ is the gyromagnetic ratio. Due to the shape of the magnet's field this region takes the form of a thin, open half-sphere (Fig. 2.7) named

the resonant slice. The signal is proportional to the number of spins undergoing periodic inversions. Furthermore, the signal also scales with the cantilever amplitude, hence by far the largest component of the cantilever deflection or frequency shift emanates from spins in the resonant slice. A 3D image can be created by moving the resonant slice through the sample. Spatial dependence is included through a field strength that is a function of the position and, if it concerns nuclei, different types of nuclei can be distinguished by their distinct value of the gyromagnetic ratio. A measurement of the beam deflection or frequency shift is possible with laser interferometers, beam deflection detectors or superconducting quantum interference devices (SQUIDs, see Sec. 1.3).
At last, it is worth to mention that instead of using a rf wire to produce a B_1 field, spin inversions can also be generated by excitation of higher modes of the cantilever. Driven higher modes cause a rotation of the tip magnet, which results in a fluctuating B_{magnet} at the spin location that can be composed in a static component and an oscillating part taking the role of a B_1 field.[8,9,12,41]

1.2.3 Polarization

The polarization of a population of non-zero spin particles can be considered as the fraction of spins pointed along the magnetic field. A high degree of polarization is a prerequisite to manipulate spin ensembles and to reduce diffusion of magnetization out of the detection volume, i.e. the resonant slice. In the most general form the polarization P_m in the thermodynamic limit, with m = -I, -I+1, ..., I, is given by

$$P_{thermal} = e^{\frac{m\hbar\gamma B_0}{k_B T}} \frac{sinh\left(\frac{\hbar\gamma B_0}{2k_B T}\right)}{sinh\left[(I+\frac{1}{2})\frac{\hbar\gamma B_0}{k_B T}\right]}. \tag{1.8}$$

The limit N $\longrightarrow \infty$ with N the number of particles implicates that Eq. 1.8 is only valid in the thermal regime (also named Boltzmann polarization, see Sec. 2.1.2). Statistical polarization (Sec. 2.1.3), on the other hand, is on average zero, therefore the standard deviation is commonly used as measure of this type of polarization. The treatment of nuclei with $I = \frac{1}{2}$ is similar to electrons, hence the polarization of an ensemble electron spins is

$$P_{thermal} = tanh\left(\frac{\hbar\gamma B_0}{2k_B T}\right). \tag{1.9}$$

This formula will be used throughout this thesis when discussing the level of polarization in the thermal regime. An expression for the statistical polarization is[3]

$$P_{statistical} = \frac{\sigma_{M_z}}{M_{100\%}} = \sqrt{\frac{I+1}{3I}\frac{1}{N}}, \tag{1.10}$$

where $M_{100\%} = N\hbar\gamma I$, the polarization of a fully polarized ensemble and σ_{M_z} is the standard deviation of the longitudinal component of the magnetization. The number of particles in a detection volume is

$$N = \frac{3}{I(I+1)}\left(\frac{k_B T}{\hbar\gamma B_0}\right)^2\left(\frac{M_z}{\sigma_{M_z}}\right). \tag{1.11}$$

$M_z = \sigma_{M_z}$ or equivalently $N = N_c$ indicates the borderline between the two regimes.

1.3 SQUID based read-out of cantilever motion

In most setups, measurements of the mechanical oscillations of the cantilever are done with a laser based read-out scheme (Fig. 1.2a). In conventional laser interferometer based apparatuses the cantilever motion is deduced from the interference intensity of the reflected laser beam. Despite significant improvements in the last two decades, the dissipated heat of the absorbed laser power in these type of systems prevents the cantilever from reaching lower temperatures than several hundred millikelvin. To circumvent this problem our setup is operated with a SQUID detection scheme (Fig. 1.2b), however this introduces several new challenges. To name the most notable:

- The inability to use an external static field throughout the cryostat due to magnetic noise that interferes with the SQUID.
- The demand for a detection scheme that shields the SQUID input coil from magnetic pulses originating from the B_1 field and static flux noise.
- The requirement for a careful positioning of the cantilever in the vicinity of the pickup loop.

Especially the lack of an external field complicates measurements, since it dictates the level of magnetic noise suppression, polarization, remnant magnetization of most magnet types and opens up the use of new measurement protocols (Sec. 2.2.2.2).
The theory and design of our specific SQUID scheme was extensively discussed in the dissertation of Wijts.[13] For a broader overview, the book "The SQUID Handbook" by Clarke and Braginski[42] constitutes the epitome of SQUID literature and includes both extensive theory as well as a broad range of applications. Here, we briefly recap the basics of SQUID theory and mention the essential elements necessary to understand how cantilever motion is transferred into a signal. A schematic overview of our entire detection setup is presented in Fig. 2.4.

SQUIDs are extremely sensitive magnetometers capable of measuring single magnetic flux quanta ($\Phi_0 = 2{\cdot}10^{-15}$ Wb). The devices are composed of two Josephson junctions, which consist of two weakly linked superconducting electrodes, in a superconducting loop to transduce a measured flux to a voltage.
Let us consider a SQUID with an input current. If an external magnetic field (the cantilever's tip magnet in our case) induces a flux change inside the loop, a screening current appears to

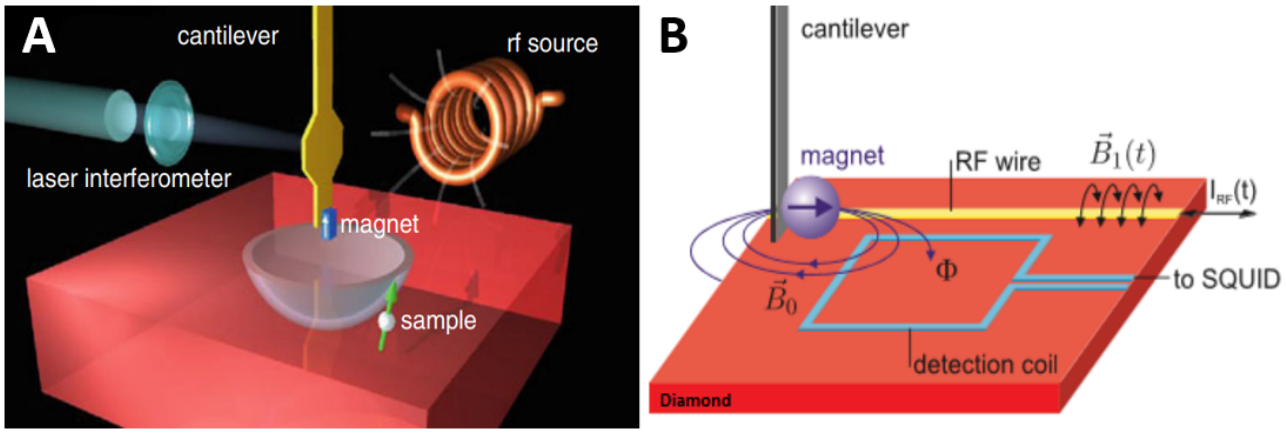

Figure 1.2: *The main two detection types: laser based (a) and SQUID based (b). Figures adapted from Rugar et al.[8] (a) and Wijts and coworkers[13] (b).*

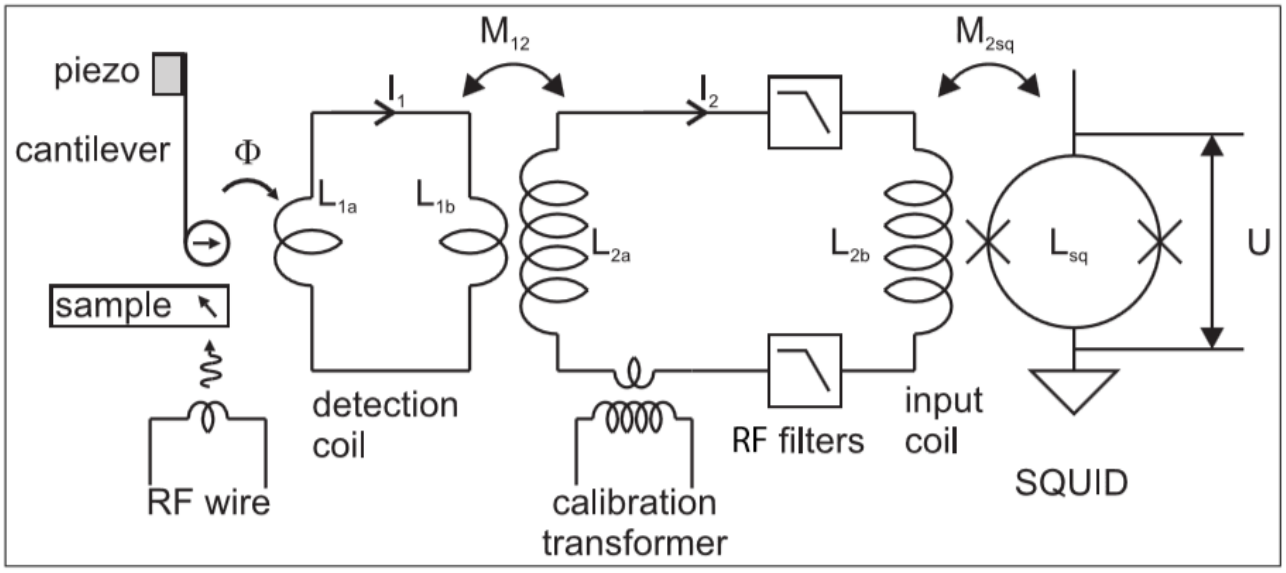

Figure 1.3: *The moving tip magnet attached to the cantilever apex induces a flux in the detection coil (referred to as the pickup loop). To arrive at the input coil, the current goes through a transformer, a calibration transformer and superconducting rf filters to protect the SQUID from pulses. Figure reprinted from Wijts and coworkers.*[13]

cancel the external field (Meissner effect). Once the sum of screening current and the input current exceeds the critical current in one of the junctions, a voltage is created across that junction, which can be measured by a lock-in amplifier.

In order to match the inductance of the pickup loop to the input inductance of the SQUID, the cantilever motion is detected through an intermediate circuit, displayed in Fig. 1.3, that is composed of a transformer. The flux resulting from the tip movement is initially detected by the pickup loop, which in return creates a magnetic field that expels the magnet's field from the inside of the coil. This force causes a shift of the cantilever's spring constant, associated with the stored energy in the coil and with the coupling strength between the cantilever tip and the coil's field. The calibration transformer allows calibration of the cantilever movement and thereby provides a way to express the motion in a voltage. Additionally, the degree of coupling can be experimentally determined by the thermal noise method as described by Wijts.[13]

1.4 Comparison among high resolution MRI techniques

MRFM is special among nanoscale resolution scanning probe microscopes for its ability to non-invasively construct an image of a material's interior. Other high resolution techniques, such as AFM and scanning tunneling microscope (STM)[43] are confined to acquisition of surface images. Furthermore, inherent to magnetic resonance methods, MRFM provides chemical contrast as well.
Although single electron spins have been detected with other techniques,[44–46] they rely on an indirect read-out of other properties, e.g. electronic current, spin current and optical transitions. Only techniques that depend on magnetic principles are capable of directly measuring the magnetic moment of a spin, however, none but MRFM and nitrogen-vacancy (NV) center[47–49] based magnetometry combined with NMR have shown the potential to be used as nanoMRI. NanoMRI includes all magnetic resonance based techniques that are capable of 3D image acquisition with nanometer resolution.

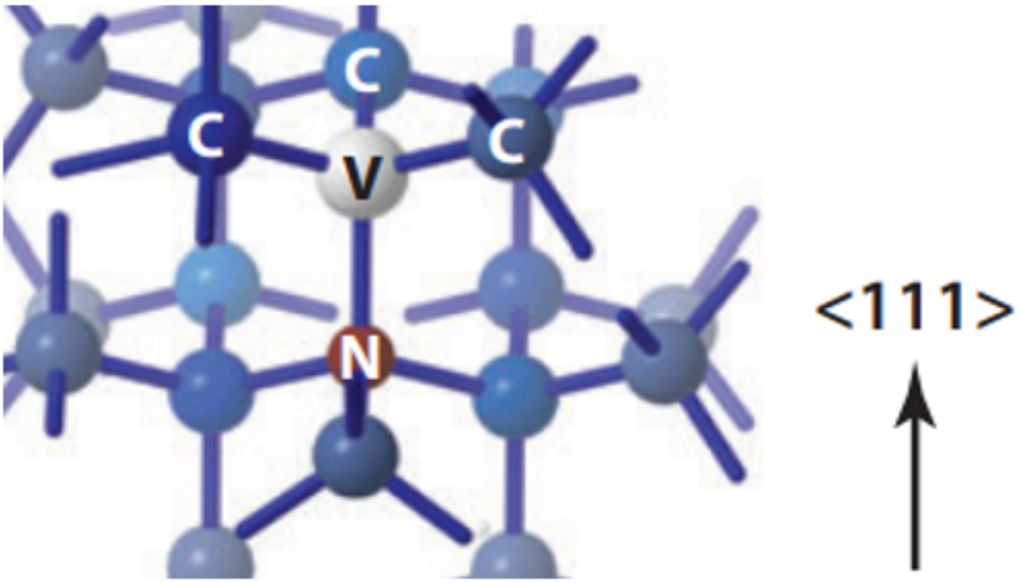

Figure 1.4: *Atomic structure of a NV center in the diamond lattice. Figure reprinted from Schirhagl et al..*[47]

NV centers are color defects embedded in the diamond lattice that consist of a substitutional nitrogen (N) atom and an adjacent lattice vacancy (V), shown in Fig. 1.4. NV centers are one of the many types of defects present in diamond (see Sec. 2.1 for a general introduction to diamond defects and Sec. 2.1.1 for an overview of the abundant P1 center).
Of the two different NV states that exist, NV^0 and NV^-, only the charged defect is of relevance for magnetometry applications. In this defect, the vacancy is occupied by an electron that, in combination with the nitrogen atom, operates as a single spin-1 conglomerate. Particularly interesting features of NV centers are their i) long coherence time, ii) high sensitivity to magnetic field changes, iii) a spin linked to luminescence properties, which allows optical detection and iv) a spin state amenable to manipulation and initialization. Furthermore, as opposed to MRFM, the requirements of a ultra-high vacuum and low operating temperature to preserve a high sensitivity are lifted. Due to these very appealing characteristics, NV centers are considered as one of the most promising candidates to achieve nanoMRI. Furthermore, they can be used in quantum computing processes[50,51] and due to their long coherence time they are presumed to be suited for a detectable spin-cantilever superposition experiment.[10]

Despite these propitious properties, it is rather difficult to measure nuclear spins and only shallow (<5 nm below the surface[3]) NV centers appear to be suited for imaging. To preserve a long coherence time and high sensitivity, NV centers have to be situated in the interior of a material. This, however, conflicts with the requirement to maximize the probe coupling (assuming MRFM is used), namely, a minimal spin-probe distance. Moreover, in order to detect nuclear magnetic moments, the interspin distance has to be small to maintain a sufficiently large dipole coupling. As a result, only near-surface defects are eligible for nanoMRI, thereby downgrading it to an effective 2D imaging method.

The inability to sense bulk material of tens up to 100 nanometer thickness with a nanometer resolution is known as the imaging gap.[3,52] So far no technique is capable of producing high resolution 3D images at this length-scale, leaving an unseen area for physicist and biologists. The structures falling in this regime are essential for the understanding of cell biology, e.g. primary, secondary and tertiary structure of protein complexes and subcellular organelles.

Various emergent techniques, such as nanoMRI and cryo-electron microscopy, are currently under development and show great potential of resolving the gap. Since MRFM is not fundamentally limited in its sensing depth it remains the only viable method for reaching a 3D, atomic resolution microscope. In practice, the size of the probe magnet restrains how deep one may see, however, even the smallest probe magnets perceive magnetic moments at several tens of nanometers.

1.5 Quantum mechanics of single-spin detection

The previous sections were devoted to several important concepts in MRFM and establish MRFM as an imaging method capable of reaching sub-nanometer resolution. In this section we treat the necessary quantum mechanics to understand a single-spin experiment.

Although electrons and nuclei belong to the class of quantum objects, a quasi-classical description of their spin dynamics is satisfactory to describe the basics of magnetic resonance.[53] The main difference between the two descriptions pertains to the spin, which is considered as simply a vector in the semi-classical limit. According to quantum mechanics a spin-$\frac{1}{2}$ particle has two spin-states called spin-up and spin-down. The direction of a spin generally constitutes of a component parallel and perpendicular to the magnetic field and includes some intrinsic uncertainty by virtue of its quantum mechanical origin. If the magnetization of an ensemble of spins is measured this uncertainty vanishes, since it is on average pointed along the magnetic field. Measuring the magnetization of an individual spin, as is done in MRFM, results in a collapse of the initial state[3] (before measuring) into an eigenstate (after measuring), i.e. spin-up or spin-down. Thus, as opposed to techniques that measure the magnetization of a large population of spins, such as MRI, finding an antiparallel orientation with respect to the magnetic field is possible in a single-spin experiment.

It was shown by Feynman *et al.*[54] that the Schrödinger equation describing the spin dynamics of a two level system reduces to a classical equation of motion. The following equation governs the time-evolution of both a single magnetic moment and an ensemble spins:[4]

$$\frac{\partial \langle \boldsymbol{\mu} \rangle}{\partial t} = \gamma \langle \boldsymbol{\mu} \rangle \times \mathbf{B}. \tag{1.12}$$

In the case of a single-spin measurement this equation describes the expected mean magnetization. Moreover, the solution of Eq. 1.12 mathematically illustrates the Larmor precession in a cone around the magnetic field (Sec. 1.2.1).
The previous part of this analysis focused on the spin's magnetization behaviour in solely a large external magnetic field (B_0). Switching on a perpendicular B_1 field perturbs the spin magnetization, which thereafter exponentially relaxes towards equilibrium (Sec. 2.1.2). To describe the spin-evolution as a result of relaxation processes it is convenient to use the Bloch equations.[25,55]

Specific to MRFM among magnetic resonance techniques is the creation of a Schrödinger cat state when the cantilever's magnet interacts with a spin. Although this effect is not measurable in our present setup it could be of interest in a future superposition experiment (see prologue to chapter 4 for a bit more detail).
If the coupling between a quasi-classical object (magnet) and a quantum object (electron

[3] The initial state is in general a superposition of spin-up and spin-down states.

spin) results in a superposition, it is called a Schrödinger cat state. There are two ways in which a Schrödinger cat state can arise: i) spin superposition as a result of spin-cantilever interaction or ii) spin superposition caused by spin-spin interactions. During the existence of this state, the cantilever trajectories are in superposition as well. Nonetheless, the state's lifetime in both cases is too short to be measurable under currently obtainable operating conditions.
The interactions between the tip magnet and a target spin generate a superpositional spin state. However, due to its strong linkage with the environment (e.g. cantilever) the wave function quickly collapses, after which the spin and the cantilever obtain one of the two possible states. Even under favorable ambient conditions, e.g. sub-mK temperatures, the decoherence time of the Schrödinger cat state is still ~10^9 times shorter than the period of a thermal fluctuation of the cantilever tip.[4]
Additionally, the manifestation of a target-spin-cantilever superposition induced by surrounding spins is likewise annihilated by the cantilever environment. The occurrence of this Schrödinger cat state originates from spin-spin interactions[4] that lead to a shift of the spin's orientation relative to the effective magnetic field. In short, the effective magnetic field is the vector sum of the B_0 and B_1 field (Sec. 2.2.2.1). Since the deviation can be inwards, reducing the angle between the spin's direction and the effective field, or outwards by increasing the angle, this gives rise to the formation of two cantilever trajectories. Similar as in the previous situation, these cat states are destroyed by disruptive environmental interactions. In general, the spin collapses to the more probable state pointed along the effective magnetic field. Every now and then the spin orientation swaps direction, i.e. a quantum jump takes place.[56] In contrast to a Schrödinger cat state, is a quantum jump detectable, since it will produce a sharp peak in the frequency shift.

1.6 Thesis outline

This thesis is organized as follows:

- *Chapter 2* is devoted to the requirements for a single electron experiment. Additionally, we test the feasibility of single-spin detection in our apparatus on the basis of these conditions. Furthermore, we study several measurement protocols and propose the best suited ones, depending on the operating situation.
- *Chapter 3* contains several setup improvements that could bring single-spin detection within reach and/or facilitate performing the measurement. Special attention is paid to the double-magnet cantilever design introduced in Ref. 9. We expand it by investigating the system with a nanometer-sized tip magnet in the presence and absence of an external magnetic field.
- *Chapter 4* features several test experiments of a piezoelectric based (abbreviated as piezo) vibration isolation design. Besides the first test experiment, further research directions and improvements are discussed.
- *Chapter 5* summarizes the conclusions of this thesis and sheds light on future steps towards single-spin detection.

[4] Spin-spin interactions form together with higher cantilever modes the main source of magnetic noise.

Chapter 2

Requirements for Measuring a Single Electron Spin

Prologue to the Chapter

The ability to retrieve the coordinates of specific spins in a numerically simulated protocol[57] is an important step in the development of a broadly applicable three-dimensional imaging technique that enables observing the structure of individual macromolecules with atomic or sub-atomic resolution. However, in order to distinguish spins, the first step is to measure an individual spin signal. In this chapter we discuss the feasibility of successfully detecting a single electron spin at millikelvin temperatures and set up the corresponding experimental requirements.
The exceedingly small magnetic moment from an electron spin fundamentally limits the sensitivity required to measure a single electron spin. This translates to conditions for stability of the apparatus and allowed cantilever noise due to thermal fluctuations. The latter is solely contingent on the cantilever stiffness and the operating temperature. For the resonant slice we set the following prerequisite: the resonant volume should, with great certainty, contain at most one electron. The resulting specification for the resonant slice thickness depends mainly on the spin density of the sample. Furthermore, to design the optimal experiment, we compare the SNR of a force based to a force-gradient based approach and use the outcome to analyze several measurement protocols best suited for single-spin detection at millikelvin temperatures. Closely related, we also discuss limitations on the spin lattice (T_1) and spin-spin (T_2) relaxation times in these protocols. At last, not specific to a single-spin measurement, the applied radio frequency magnetic field should be of sufficient strength to flip a spin, while the dissipation should not lead to extensive heating. This is, especially at millikelvin temperatures, a rather intricate and distinct challenge for MRFM experiments.

The structure of the chapter is according to the order of parameters listed below. To support the discussion about the conditions a single-electron experiment has to satisfy, we first scrutinize the dynamics of impurities in diamond, housing the perceptible spin. As a summary, these are the relevant parameters that determine whether single-spin sensitivity is within reach.

1) *Dynamics of defects in diamond: relaxation times*
2) *Signal-to-noise ratio of different MRFM protocols*
3) *Strength of the radio frequency magnetic field*
4) *Cantilever noise and operational temperature*

5) *Resonant slice thickness and spin density*

6) *Apparatus stability*

In this chapter, we will not focus much on the operating temperature, since we use the innovative SQUID-based read-out (Sec. 1.3) of the cantilever motion for a measurement at millikelvin temperature. Previous conducted experiments where single-spin sensitivity has been achieved used an optical interferometer or beam deflection detector and were carried out at a temperature that exceeds the millekelvin range by one to two orders of magnitude.[8,16,17,58]
Throughout this chapter we base the magnetic field strength and its gradient on the currently employed magnet made of neodymium (NdFeB), having a diameter of 3.5 μm and a remnant magnetization (RMT) of 1.3 T (Tab. 2.1).

2.1 Dynamics of defects in diamond

For over a century diamond has been the subject of extensive research unraveling its physical and chemical structure.[59,60] After the rediscovery of diamond nanocrystals,[61] the realization of synthetically fabricated diamond[62–64] and the ability to tailor its features,[65,66] the research in diamond exploded and nowadays covers a baffling range of applications in physics,[67] chemistry,[68] biology[69] and industry. At the foundation of the present ubiquity lie its poor electrical and high thermal conduction, environmentally non-virulence, exceptional hardness and incompressibility, biocompatibility, chemical stability and fluorescence. A particular interesting property of diamond is its high susceptibility to low concentrations of impurities, making diamond an attractive specimen for many resonance studies.
Both synthetic and natural diamond contain defects leading to distortions of the lattice structure. The definition of a defect is as follows: all atoms other than ^{12}C,[1] including the isotope ^{13}C, are referred to as a defect. Examples of defects include impurities, lattice vacancies, interstitial atoms and dislocations of atoms.[70–72] Nitrogen impurities are the prevalent impurity and defect in both synthetically grown diamond and natural diamond.
Diamonds are classified in two groups according to their abundance of nitrogen impurities.[73] In type I, the presence of nitrogen is sufficient to obtain a measurable absorption signal, whereas, in type II it is not. A further subdivision can be made based on the arrangement of nitrogen atoms. Although contamination by other types of impurities, such as phosphor, boron, oxygen and hydrogen were observed,[74–77] the scarcity of these justifies only treating nitrogen induced defects. The reason for their absence is a much higher formation energy compared to nitrogen.[75,78]

Given the physical analogy between different nitrogen impurities, we only briefly review the most frequently occurring magnetically active nitrogen impurity, the P1 center. Particular attention is paid to its magnetic behavior, leaving out a discussion concerning its vibrational, optical, electronic and other types of properties.[75,79–81] We refer to the overview written by Loubser and van Wyk[60] about ESR in diamond for a full treatment of diamond impurities including all different substitutional nitrogen induced centers. Next, a synopsis about electron spin dynamics at low temperature is provided. At first, the relaxation mechanisms are discussed in general and thereafter the discussion shifts to more MRFM related topics. We end the section with an overview of all relevant measured and calculated variables.

[1] The natural abundance and the total angular momentum I, i.e. the nuclear spin, of ^{12}C and ^{13}C are 98.9% and 1.1%, and 0 and 1/2, respectively.

2.1.1 The P1 center

The properties and structure of lattices sites containing substitutional nitrogen atoms were extensively documented using ESR[82–84] and electron-nuclear double resonance[85,86] (ENDOR). The extra unpaired electron neutral nitrogen has over carbon nuclei can be localized on any of the bonds shared with adjacent atoms, which gives rise to many types of impurities. Observed by Smith *et al.*[83] using ESR, P1 centers were one of the first types of nitrogen donors[2] found. Depicted in Fig. 2.1a, they encompass the hyperfine interactions of a paramagnetic electron with a single C atom and an isolated ^{14}N[3] nucleus.

Let us first recall the fundamentals of molecular orbital (MO) theory[88–90] to ease the discussion about the structure of P1 centers. MO theory was developed to explain the molecular electronic structure taking quantum mechanics as starting point and to compute the orbital wave functions of polyatomic molecules. In MO theory, electrons are assumed to be delocalized and to interact with multiple atoms. Molecular bonds are calculated as a linear combination of atomic orbitals (LCAO), which is a widely used technique in computational quantum chemistry.
The concept of atomic orbitals (AO) is convenient to mathematically describe the spatial probability density of a single electron. An AO is uniquely characterized by the set of quantum numbers n (principle quantum number), l (azimuthal quantum number), m_l (magnetic quantum number) and s (spin quantum number), representing the electron energy, electron angular momentum, azimuthal component of the orbital orientation, and orbital energy and form, respectively. The combination of n and l relates to the familiar $(n)s^A$, $(n)p^A$, $(n)d^A$ and $(n)f^A$ orbitals corresponding to l = 0,1,2,3, and where n represents the energy of the

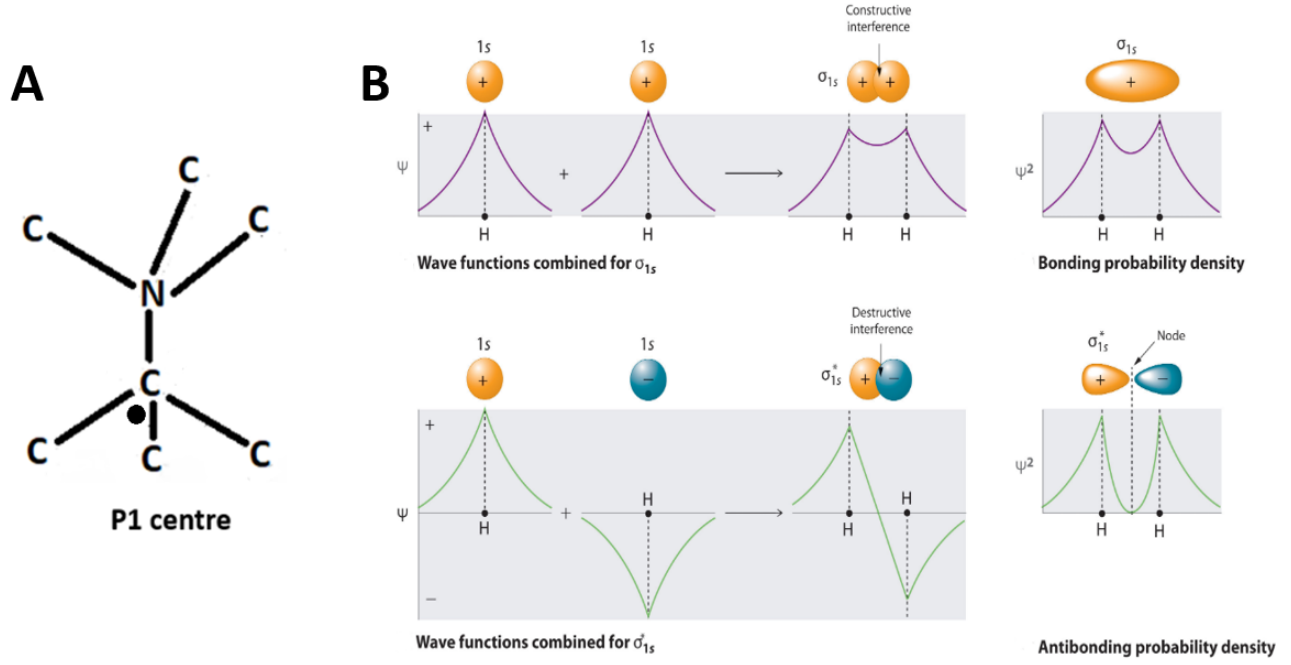

Figure 2.1: *(a) A scheme of the chemical structure of a P1 center within the diamond lattice. The dot represents the position of the unpaired paramagnetic electron. Figure inspired by Loubser and coworkers.[60] (b) A sketch of bonding and antibonding σ_{1s} and σ^*_{1s} MOs respectively as explained in the text. In the plots Ψ represents the orbital wave function. The shape of a ns AO is spherical and contains nodes if n > 1. Figure adapted from Ref. 91.*

[2] Actually Smith *et al.*[83] found four equally probable types of donors corresponding to the four C-N bonds.
[3] The abundance of ^{14}N in nature is 99.64%. Spectra of ^{15}N were measured, see for example.[87]

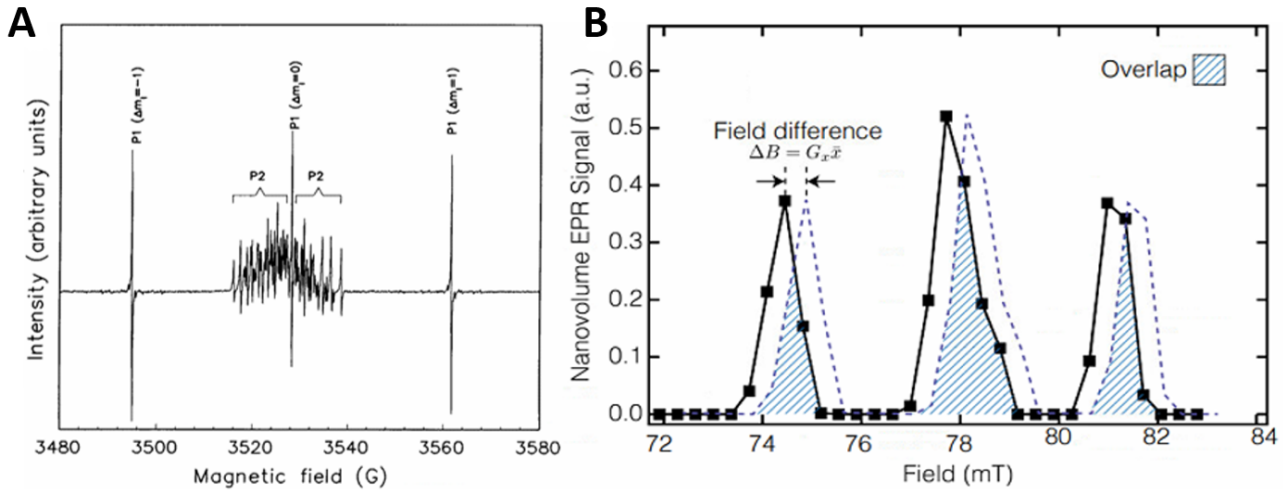

Figure 2.2: *(a) A conventional ESR spectrum of P1 and P2 centers. P2 centers consist of a single carbon atom connected with three nitrogen atoms placed in nearest neighbor positions relative to each other. Even though the bonding structure is more complicate than for P1 centers it leads to an identical situation with a single unpaired paramagnetic electron primarily located near the carbon atom. The P1 center has 3 hyperfine splittings, whereas, the P2 center has 54 due to its coupling with three nitrogen atoms. Figure reprinted from Wyk and coworkers.[84] (b) The overlap spectrum of two adjacent P1 centers characterized by the field difference ΔB. This particular spectrum is used for the calculations of the suppression factor, subject of discussion in Sec. 2.1.3. The three peaks belong to the m_I = -1,0,1 states. Figure reprinted from Cardellino and coworkers.[23]*

orbital and A the number of electrons in the orbital. AOs are filled with electrons according to the Pauli exclusion principle.
When two atoms approach each other to an extent that their AOs overlap, this results in the formation of a MO that can be classified as: (i) bonding, (ii) antibonding or (iii) nonbonding. Bonding and antibonding orbitals can qualitatively be understood by considering electron wave functions that constructively or destructively interfere (Fig. 2.1b), whereas nonbonding MOs contain no interactions. Bonding orbitals have a lower energy than the individual AOs they are composed of, while antibonding orbitals have a higher energy and involve distinctive nodal planes, i.e. regions between the atoms where the electron wave function is zero. Further sorting of MOs is based on the participating AOs that produce nodal planes and symmetries with respect to the internuclear axis. The different MO types are labeled σ, π, δ and ϕ and include an asterisk to indicate an antibonding orbital. In general they correspond to interactions of two s, p, d and f AOs respectively.[4] Filling of MOs is established according to Hund's rule and the Pauli principle.
The electron density of bonding orbitals is particularly high between the nuclei, as such, the attractive interaction of the negative electron and the positive nuclei stabilizes the orbital. On the other hand, in antibonding orbitals the electron is mainly located on the opposite side of a nucleus relative to the in-between nuclei side. Furthermore, interactions in antibonding orbitals are repulsive and destabilize the orbital.

In richer detail, a P1 center consists of an unpaired paramagnetic electron predominantly situated on the carbon atom,[82] accommodated in a C-N antibonding orbital. This leads to an increase of the bond length due to spontaneous symmetry breaking. The phenomenon was previously thought to be a linear Jahn-Teller effect,[60] which states that a non-linear molecule

[4]Higher order AOs are rare, but do exist. Omitting j, labeling continues alphabetically from g on. Two overlapping g AOs are presumed to create a γ MO, however ϕ MOs are the highest order orbitals observed to date.

with a spatially degenerate orbital experiences a geometrical distortion to eliminate the degeneracy.[92] However, ab initio molecular orbital calculations of Bachelet and coworkers[93] revealed that the singly occupied state in the diamond band gap caused by nitrogen is in fact non-degenerate. They attributed the lattice distortion to severe non-linear modifications of the chemical bonding structure. More recent research confirmed their conclusion,[75,86] ascribing the distortion to an antibonding interaction between a single-electron-containing dangling bond from the carbon atom and the unpaired electron from nitrogen. The repulsive nature of this interplay emanating from the Pauli exclusion principle emerges in the asymmetrical displacements of the carbon and nitrogen atom. As a result, the distorted orbital has a lower energy than the other C-N bonds. The total magnetic moment of the unpaired electron in this non-degenerate orbital is nearly equivalent to the spin magnetic moment, since the transfer of magnetic energy to the orbital magnetic moment is suppressed.[60] Therefore, we can treat it as a simple spin-$\frac{1}{2}$ free electron with a g-factor that is only weakly anisotropic, i.e., it closely resembles the free-spin value.

The shape of ESR spectra elucidates the precise hyperfine splitting structure and thus contains the definite answer in regard to the different centers present in the probed diamond (see for example the ESR spectrum of the P1 and P2 center in Fig. 2.2a). Additionally, the overlap of ESR spectra provides the basis for flip-flop suppression calculations (more on this in Sec. 2.1.3).

2.1.2 Relaxation times in diamond

Relaxation times play a prominent role in the detection process of all resonance based measurement techniques. In this section we elucidate the physical mechanisms that underlie the relaxation times in diamond, with specific emphasises on the low temperature regime.

The relaxation times of different impurity centers depend on the temperature, applied magnetic field strength, impurity density and the specific diamond structure. Nevertheless, for sufficiently low temperatures and high polarization the spin-spin relaxation time (T_2) converges to a value of approximately 250 μs.[94] Using ESR, a sudden rise of T_2 was reported by Takahashi *et al.*[94] to happen when the thermal energy becomes smaller than the Zeeman splitting energy ($k_b T < \mu_B B_0$). By reaching a polarization of 99.4%, spin bath thermal fluctuations, causing spin decoherence, were almost entirely erased. This type of polarization is known under the name Boltzmann polarization.[21,25,55]
Thermal fluctuations express themselves through flip-flops, which is a spin transport mechanism originating from the dipole coupling between spins. This process allows opposite aligned spin-pairs to mediate their polarization and magnetization. A spin generates a resonant magnetic field at the site of an adjacent spin, causing two-way transitions if the Larmor frequency of the spins coincides. The accompanying offset from thermal equilibrium results in an oscillating spin-ensemble temperature towards equilibrium, giving rise to thermal fluctuations. The rate at which these flip-flops take place dominates the lifetime of electron-spin coherence.

Conventional ESR experiments are essentially conducted in on isolated spin ensemble, because the detection volume exceeds the sample volume. Spin magnetization is thereby conserved so spin diffusion, inherent to spin transport, can be disregarded. Moreover, a high polarization quenches the energy-conserving flip-flop processes taking place. The quenching of flip-flops can be understood as follows: the flip-flop rate scales with the amount of neighboring spin pairs of opposite allignment, which drastically reduces as the polarization

increases.[95]
The limiting mechanism for reaching longer T_2 times are the nuclear spin bath fluctuations of ^{13}C that have a decoherence time of 250 μs.[94,96]

Altogether, the spin-spin relaxation time can be modeled by

$$\frac{1}{T_2} = \Gamma_{ff} + \Gamma_{res}. \tag{2.1}$$

In this expression Γ_{ff} is the flip-flop rate and Γ_{res} is the residual relaxation rate present from ^{13}C nuclei. A more sophisticated equation is needed to include the dependence on temperature and interrelated Zeeman energy.[94]

On the other hand, the longitudinal relaxation (T_1) is in general heavily dependent on the temperature, magnetic field and impurity concentration. An exception is the low temperature regime where it is, in contrast to higher temperatures, only slightly amenable to temperature changes,[19] but more to a specific impurity density at higher spin concentrations. Wyk and coworkers[84] demonstrated that there is no correlation between the linewidth and the impurity concentration for spin densities <10 ppm, implying no relation among relaxation times and spin density either in that range.
The T_1 process is comprised of three temperature ranges each possessing its own regulation mechanisms.[97] At low temperatures, T_1 is mainly controlled by cross relaxations and spin-orbit tunneling induced by phonons.[98,99] Cross-relaxation is a flip-flop process,[100,101] occurring when the transition energy of spin species, e.g. different types of centers, with unequal orientations matches. Although, the effectiveness of the cross-relaxation rate depends on the interacting defect types present in a conglomerate.
In the paper by Reynhardt *et al.*[99] about relaxation times of nitrogen impurities, spin-orbit tunneling in P1 centers is attributed to the Jahn-Teller effect, however, it was shown[75,86,93] that the Jahn-Teller effect cannot describe the distortions observed in P1 centers. Therefore, it is likely that spin-orbit tunneling has a different origin. Another mechanism that might play a role are electron interactions with highly energetic lattice phonons, also known as the two-phonon Raman process.[97] The impact on T_1 is rapidly overruled for small T as it is proposed to scale as $(1/T_1)_{Raman} \propto T^5$ below T_{Debye} (~2000 K for diamonds[102]).
Furthermore, it is interesting to note that the temperature independent behavior of cross relaxations is also anticipated from the dipole coupling, having no dependence on temperature in this regime. Secondly, an alluring experimental property of T_1 at low temperature is its strong correlation with the magnetic field strength. This allows a tuning of T_1 that could be of use in MRFM to, for example, optimize certain measurement protocols.[97]

2.1.3 Flip-flop suppression and quenching of spin diffusion

A characteristic distinction between MRFM and macro-scale techniques, such as ESR, is the ensemble size, already briefly mentioned in the previous subsection. For increasingly smaller spin ensembles, statistical fluctuations[26–28,103–105] in the polarization, an intrinsic property of a system of magnetic moments, will eventually overrule thermal fluctuations. Statistical fluctuations, i.e. spin noise, are usually not present in ensembles containing more than a few dozen spins.[25,103] For, in our case, typical values, e.g. spin density is 0.4 ppm (Tab. 2.1), T = 20 mK and a Larmor frequency of 3.5 GHz, the transition happens around a detection volume of $(11nm)^3$. Likewise as for Boltzmann polarization, the exchange of magnetization and polarization happens by means of flip-flops. The peculiar difference lies

in the average polarization, being zero in the statistical regime, while the Boltzmann polarization is on average aligned along the applied magnetic field.
Furthermore, the flip-flop process is slightly altered in MRFM compared to regular resonance experiments. Active stimulation is effectuated by an applied rf field oscillating at a certain Larmor frequency. Only spins whose resonance frequency matches the rf frequency are affected, resulting in the formation of a resonant slice. This is the core of MRFM as explained in Sec. 1.2.2.

In contrast to the conventional procedure of applying a strong magnetic field to attain extraordinarily high polarization,[94] that role is allocated to the gradient in MRFM. The quintessentially high magnetic field gradients have profound consequences for flip-flop suppression and spin diffusion.
In a nonuniform magnetic field the transition energy is no longer equal at different spin locations outside the resonant slice, prohibiting flip-flops from occurring, because energy conservation is violated. Nonetheless, the enduring observed presence of spin diffusion[19,23] suggests the existence of a compensation mechanism. The probability to balance out the energy difference experienced by two spins is given by the overlap of their lineshapes,[22,106] which manifests itself as an inhomogeneous broadening of their spectra. According to Budakian *et al.*[22] flip-flop suppression, and accordingly quenching of spin diffusion, kicks off when the discrepancy in magnetic field strength at adjacent lattice sites surpasses the size of spin-spin dipole interactions. The critical gradient for this to happen is

$$G_{crit} = \frac{\Delta B_{dd}}{\bar{a}}, \tag{2.2}$$

with ΔB_{dd} the homogeneous linewidth and $\bar{a}$ the average interspin spacing. For surface spins in our specimen G_{crit} = 73 mT/μm,[19] whereas, for bulk spins, taking $\bar{a}$ = 12 nm (Tab. 2.1) and assuming the same linewidth of 0.14 mT we expect G_{crit} = 12 mT/μm. These gradients are considerably lower than the maximal obtainable gradient in our setup of approximately 0.5 MT/m in the radial direction at a tip-sample separation of circa 200 nm, implying the possibility of strong flip-flop suppression.

Spin diffusion could start playing a non-negligible role[23] in MRFM, since the measurement volume is so small compared to most other techniques. If the diffusion length is larger than this volume, flip-flops lead to transport of magnetization out of the detection volume into the bordering spin reservoir, effectively reducing the lifetime of spin-spin and spin-lattice relaxation.[22] The diffusion length can be determined from

$$L_D = \sqrt{DT_1}, \tag{2.3}$$

where $D = \bar{r}^2/T_{ff}$ with $\bar{r} = 2\bar{a}$ the average separation between spins and T_{ff} the flip-flop time.

2.1.3.1 Estimate of T_{ff}

In the next paragraph we closely follow the discussion in Sec. 3 and 4 of the supplementary material published by Cardellino *et al.*[107] regarding the flip-flop time of P1 centers to find an estimate of T_{ff}.
The flip-flop time is the inverse of the transition rate W of an electron going from state a to state b. Taking Fermi's Golden rule as onset to calculate W, furthermore, assuming a diluted

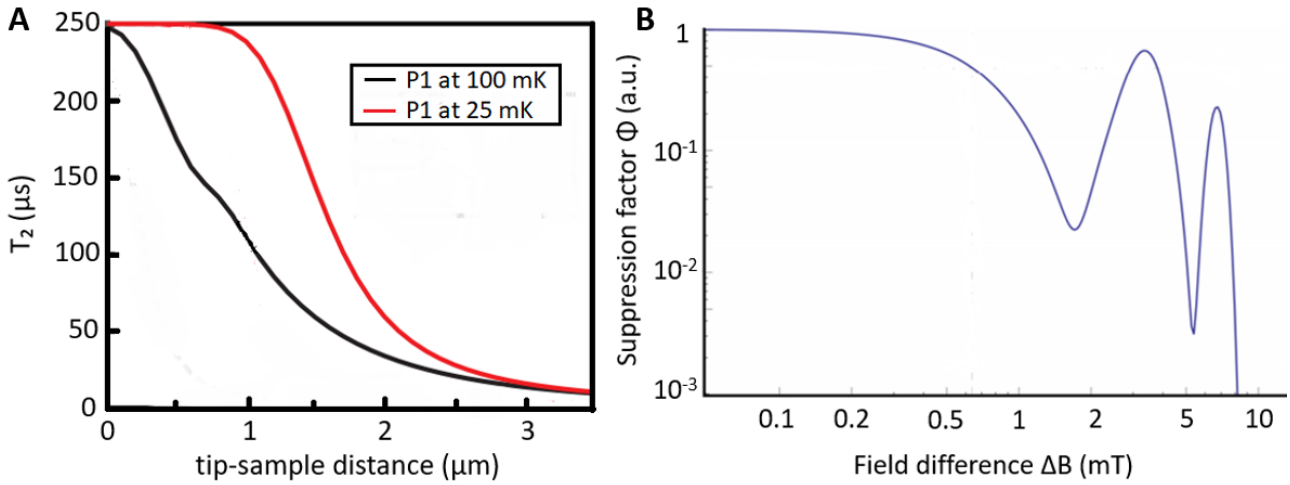

Figure 2.3: *(a) Prediction of the T_2 time of P1 centers for different temperatures. Calculations were completed for a NdFeB magnet with a diameter of 3 µm and a remnant magnetization of 1.15 T. Flipflop suppression was computed from the overlap of lineshapes of spin pairs participating in the flipflop process. In this calculation, a 0.4 ppm impurity spin density and uniform randomly distributed spins, see Sec. 2.5.1, were assumed. Figure adapted from de Voogd.[10] (b) Quantitative analysis of the influence of a field gradient on the suppression factor. The suppression factor was calculated from the normalized overlap function, partially depending on the ESR overlap spectrum for T = 4.2 K shown in Fig. 2.2b. Figure adapted from Cardellino and coworkers.[23]*

spin concentration ($< 10\%$), the spin spectrum to be a Lorentzian with a cutoff at a value much larger than full width at half maximum (FWHM), equal Zeeman splittings and a cubic diamond lattice one can devise a calculable, analytical expression for W. Here, however, we use that the non-suppressed flip-flop time is commensurate with the spin concentration and scales with the sixth power of $\bar{r}$. This scaling behaviour was deduced from the analysis of Cardellino and coworkers. It reads

$$T_{ff,hom} \propto cr^6, \tag{2.4}$$

where c is the concentration. By using $T_{ff,hom} = 0.13$ ms for a concentration of 6 ppm and $\bar{r} \approx 9.8$ nm (measured by Cardellino and coworkers) we can simply determine the flip-flop time from Eq. 2.4 once the spin density is known. M. de Wit and G. Welker *et al.*[19] reported a bulk spin density of 0.4 ppm in our sample, from which we extract $T_{ff,hom} = 0.55$ ms in a homogeneous magnetic field.

In the presence of flip-flop suppression, $T_{ff,sup} = T_{ff,hom}/\Phi$ with Φ the suppression factor as function of the average energy difference ΔB between abutting spins. Φ is proportional to the probability that neighboring spins exchange magnetic energy. Assuming a gradient of 0.5 mT/nm and defining ΔB as the product of $\bar{a}$ and G_L, the local gradient, yields $\Delta B =$ 6 mT corresponding to $\Phi \approx 0.01$ (Fig. 2.3b). In conjunction with the unsuppressed value, $T_{ff,hom}$, we estimate $T_{ff,sup} \approx 55$ ms. From now on we will refer to $T_{ff,sup}$ as T_{ff}.

It is appropriate to remark that the calculation of Φ partly depends on the ESR spectra shown in Fig. 2.2b of two adjacent spins having a resonance frequency of 2.2 GHz and experiencing a gradient of 0.13 MT/m at 4.2 K. These conditions are in striking contrast with both the environment our sample is exposed to and the gradient it endures. To compensate, we conjecture spins in our specimen have a longer flip-flop time.

The parameters $\bar{r}$ and the formerly listed $\bar{a}$ denote the average spin-spin distance and separation, respectively. Meanwhile the maximum nearest neighbor distance was used in calculations in imitation of the literature standard. Since the flip-flop time adheres to scaling

Table 2.1: *Overview of the relevant dynamical values of our diamond sample and operational parameters*

Sample parameters			
Variable	**Value**	**Variable**	**Value**
T_1 [1]	1 ms	ρ [1]	0.4 ppm
T_2 [2]	250 μs	σ [1]	0.072 spins/nm^2
T_{ff} [2]	55 ms	$r_{interspin}$ [2]	24 nm
L_D [2]	3 nm	$G_{crit,surface}$ [1]	73 mT/μm
$T_{1\rho}$ [3]	$\gtrsim$ 100 ms	$G_{crit,bulk}$ [2]	12 mT/μm
τ_m [3]	~1 s	ΔB_{dd} [1]	0.14 mT
Operational parameters			
Variable	**Value**	**Variable**	**Value**
k_0 [1]	50 μN/m	f_0 [1]	3 kHz
Q-factor [1]	~3500	RMT [1]	1.3 T
r_{tip} [1]	1.75 μm	T [1]	20 mK

[1] Measured
[2] Calculated
[3] Expected value

Most variables are prone to small changes in temperature and magnetic field thus they should be viewed rather as a careful estimation than a precise determination. In all the situations involving calculations a gradient of 0.5 MT/m and an on operating temperature of 25 mK were assumed, except for the diffusion length and flip-flop time, which were computed as described in the text. The Q factor of 3500 belongs to a tip-sample separation of 200 nm, which we take as standard distance in our calculations unless stated otherwise. The rotating frame spin-lattice relaxation time ($T_{1\rho}$) and spin lifetime (τ_m) are elucidated in Sec. 2.2.1. We use the maximal $r_{interspin}$ in this thesis in accordance with literature.

laws the result remains unchanged, howbeit, the bulk critical gradient is actually somewhat larger than predicted. A more elaborated analysis on the characteristics of spin distances is presented in Sec. 2.5.1, including an estimate of the average spacing between spins.

The precise T_1 time of our specimen relies strongly on the tip-sample spacing and the magnetic field gradient, however, it has been measured to be on the order of a millisecond.[19] The used measuring method, magnetic force microscopy (MFM), is only susceptible to spins with a longitudinal relaxation time comparable to the cantilever period (about 0.3 ms), while we expect a distribution of T_1 times. The spreading could result from the field gradient giving rise to anomalies in the coupling strength and from differences between spin species, i.e. some relax faster than others. The presence of spins having a relaxation time a couple orders of magnitude larger than mentioned here is therefore not inconceivable.[94] The inadequacy of MFM affects the measurement of the spin density correspondingly, 0.4 ppm is merely a lower limit. A more meticulous method, receptive to a broader range of T_1 times is required to give a decisive result. An upper limit, however, is already set since the manufacturer specifications indicate a maximal concentration of 1 ppm.

From the above examination we conclude that the diffusion length is roughly 3 nm and, from Eq. 2.1, $T_2 \approx 249\ \mu s$.
The calculated value of T_2 is in excellent agreement with the outcome from simulations conducted by de Voogd,[10] presented in Fig. 2.3a. The results demonstrate $T_2 = 250\ \mu s$ for P1 centers at 25 mK as long as the tip-sample distance is less than 1 μm. The major dissimilarity between the two cases: the influence of resonance peaks in the suppression factor on the modeled T_2 time is absent in Fig. 2.3a while visible in Fig. 2.3b. The lack of fluctuating behavior in Fig 2.3a is due to the assumed Gaussian lineshapes of P1 centers and the spatially invariant field gradient experienced by spins.
In addition, the situations describe divergent temperature regimes. Since we perform experiments at a temperature two orders of magnitude lower than Cardellino *et al.*[23] the calculated diffusion length and flip-flop time should be considered an upper bound and a lower bound, respectively. Therefore, and for convenience, we take $T_2 = 250\ \mu s$ from now on.

We end this section with an overview of all calculated and measured intrinsic parameters of our sample and cantilever, displayed in Tab. 2.1. To facilitate coming discussions we use the results presented here in the remaining sections.

2.2 Measurement protocol selection

The first feasibility test for the unambiguous detection of a single spin is the determination of the smallest detectable magnetic moment in a given setup. This lower limit for the sensitivity is defined as $\mu_{min} = F_{min}/G$, where G is the magnetic field gradient stemming from the micromagnet attached to the cantilever tip and F_{min} the minimum detectable force on the cantilever given by $F_{min} = \sqrt{S_F b}$. In the latter equation, b is the detection bandwidth and S_F the thermal force noise: $\sqrt{S_F} = \sqrt{4k_B T \Gamma_t}$, with k_B the Boltzmann constant, T the temperature and Γ_t the total damping experienced by the cantilever. Γ_t is composed of the damping inherent to a specific cantilever geometry and material and non-contact interactions, e.g. surface friction.

Mechanical damping

The mechanical or intrinsic damping, named Γ_m here, is in the most general form given by $\Gamma_m = \frac{\sqrt{km}}{Q}$,[39] which in the case of a rectangular cantilever of mass m can be written as[11]

$$\Gamma_m = \frac{\sqrt{E\rho}wt^2}{2QL}. \tag{2.5}$$

Here ρ is the material density, Q the quality factor[5] and for the spring constant k we substituted $\frac{Ewt^3}{4L^3}$, where E is the material's Young modulus and w, t and L the width, thickness and length of the cantilever, respectively. The non-contact spin bath-cantilever coupling induces a shift of the cantilever's natural frequency and a change of its Q-factor as derived by de Voogd and coworkers.[108] As discussed in more detail below, the dissipation is purely imaginary and it originates from paramagnetic spin-cantilever interactions.
An additional lowering of the quality factor should be taken into account due to clamping losses.[109] The cantilevers used in our group are chosen for their low damping, which has been measured to be approximately 10^{-13} kg/s.[9]

[5]The quality factor Q is defined as 2π times the ratio of the stored energy to the lost energy per cycle.

Magnetic damping

By lowering the spring constant and increasing the quality factor, the force sensors in MRFM were optimized to a degree that non-contact friction is the dominant noise source in measurements. The contribution of spins to cantilever dissipation is related to the imaginary part of the magnetic susceptibility of the spin bath-cantilever system,[108] therefore no detailed knowledge of the spin system, such as the concentration or present spin species is required to measure this type of damping. The magnetic interaction of the cantilever tip with paramagnetic spins is manifested as a transfer of angular momentum through flip-flops.[110] In the most general form, the paramagnetic damping, labeled Γ_m, is given by[110]

$$\Gamma_m = \frac{\omega_0 \chi^{''}(\omega_0)}{2\gamma^2 I}, \tag{2.6}$$

with ω_0 the cantilever's resonance frequency, γ the gyromagnetic ratio, I the moment of inertia of the cantilever and χ'' the imaginary part of the paramagnetic susceptibility related to χ as $\chi(\omega) = \chi^{'}(\omega_0) + i\chi^{''}(\omega_0)$ with $\omega = \omega_0 - i\Gamma_m$.

Electric damping

Although the mechanisms behind force fluctuations are not yet fully understood, it was observed that surface dissipation scales quadratically with the tip-sample voltage difference, implying that dielectric fluctuations also play a role.[111,112] Using fluctuation-dissipation theorem (FDT) the electrical cantilever dissipation emanating from non-contact friction, termed Γ_e here, can be expressed as[112]

$$\Gamma_e = \frac{q^2 S_E(\omega_0)}{4k_B T}, \tag{2.7}$$

where q is the present charge on the cantilever tip and $S_E(\omega_0)$ the power spectrum of the electric field fluctuations evaluated at the resonance frequency of the cantilever, ω_0.
Nevertheless, it was found that magnetic-based dissipation prevails at very low temperatures.[34] Due to our relatively large magnet this type of damping is even more intensified.

It is worth to note that upfront mechanical amplification of the cantilever motion significantly reduces and potentially avoids surface and detector noise.[113,114] By effectively squeezing noise, parametric amplification is a viable method to enhance cantilever displacements above the detector noise level.

Minimal detectable magnetic moment

Ultimately, the minimal perceptible magnetic moment is[5]

$$\mu_{min} = \frac{1}{G}\sqrt{4k_B T \Gamma_t b}. \tag{2.8}$$

In our setup, $\sqrt{S_F} \simeq 3.9aN/\sqrt{Hz}$ at 20 mK and at 200 nm from the sample surface[19] (that means $Q \simeq 3500$ and $G \simeq 5{\cdot}10^5\ T/m$) so in an 1 Hz detection bandwidth the smallest perceptible magnetic moment is $8{\cdot}10^{-24}$ J/T. This is below $\mu_{electron}$ (Sec. 1.2.2) so a single-spin signal is measurable.

section outline

In the remainder of this section we compare the SNR of a force based to a force-gradient based approach and discuss the influence of noise on the averaging time in a single-spin experiment. At the end, after analyzing the limitations, we propose a measurement protocol best suited for single-spin detection.
Furthermore, we present a fast-approach calculation of the frequency shift for various experiments that we propose to perform as an intermediate step towards single-spin detection.

2.2.1 Signal-to-noise ratio

The comparison of the SNR for the two main measurement techniques in MRFM is comprehensively treated in the theses of predecessors.[11] As such, we will only state the most important results in bullet form. The total noise is comprised of detector noise, thermal noise (Brownian motion) and sample noise (e.g. see Sec. 2.2.3.2). More specific to our experiment:

- *SQUID noise*. Falling in the class of detector noise, SQUIDs have a white noise floor ranging somewhere between 10 to 100 pm/$\sqrt{Hz}$ below 300 mK,[10] translated from flux quanta to cantilever motion through the area of the pick-up loop.
- *Phase-Locked Loop (PLL noise)*. Another form of detector noise; frequency modulation results in sidebands of incoherent white noise causing phase jitter in the PLL device.
- *Thermal noise*. All-present noise originating from random motions of the cantilever tip. More on this subject in Sec. 2.4.1.

Next, the force-amplitude SNR of a force based, a force-gradient based approach and their respective ratio is given.

- *Force*: $SNR_F = \mu \frac{dB_0}{dx} \frac{1}{4k_B T \Gamma_t}$.
- *Force-gradient*: $SNR_{FG} = \mu \frac{d^2B_0}{dx^2} \frac{A}{4k_B T \Gamma_t}$.
- *Force versus force-gradient*: $\frac{SNR_F}{SNR_{FG}} = \frac{\frac{dB_0}{dx}}{\frac{d^2B_0}{dx^2} A} \propto \frac{R}{A}$.

Here, A is the driving amplitude (Sec. 2.4.2) and a cantilever tip magnet having a magnetic dipole[6] with R the tip-spin distance was assumed to arrive at the last step in the force vs force-gradient comparison. It is apparent that a force measurement yields a higher SNR when the tip-sample separation is greater than the driving amplitude. Nonetheless, the only single-spin experiment to date was performed with a force-gradient protocol while the size of the set cantilever amplitude was far below the tip-sample distance.[8]
The reason to choose for a force-gradient approach over a direct force measurement is twofold. Detection of incident forces requires the cantilever tip to be in a steady state during the coherence time of a spin. Unfortunately, as a consequence of the high quality factor, the response time of a cantilever can be orders of magnitude longer than the spin relaxation times, thereby spoiling the sensitivity to spin forces. In order to evade deleterious cantilever responses, feedback schemes were developed[115–118] to reduce the time needed to reach equilibrium. On the other hand, force-gradient protocols allow a more expeditious detection, because frequency shifts can be measured while the cantilever is driven towards a steady state.

[6] Dipole magnetic field B $\propto R^{-3}$ with R the distance from the magnet.

Secondly, many pulse sequences specifically intended for force measurements, for example spin echo,[119,120] use a combination of π and $\pi/2$-pulses, which require a homogeneous B_1 field modulated at exactly the cantilever frequency. Moreover, the homogeneity scales with the amplitude of the B_1 field, therefore a higher current is needed which leads to more dissipation. Although applied in both force and force-gradient approaches, the requirement for adiabatic pulses to coherently drive the cantilever is less stringent, because they only involve adiabatic amplitude or frequency modulation of the rf field depending on the rotating frame spin lifetime compared to the cantilever frequency.[5] Adiabatic pulses only require the fulfillment of the adiabatic condition (Sec. 2.2.2.1), which is generally achieved at a lower B_1 field than other type of pulses. Since the cooling power at 20 mK is so little, adiabatic rapid passage (ARP) based protocols remain the only viable method for single-spin detection (Sec. 2.2.2.1).

Signal averaging

The prevalent noise source in an experiment could be instrument noise, thermal noise or spin fluctuations. If the standard deviation $\sigma_{spin} \gg \sigma_{detector}, \sigma_{thermal}$ then the SNR is in general as presented in Ref. 21 and 5. In the same limit, in Ref. 57 an analytical expression for the SNR in the Boltzmann regime is inferred based on the expectation value of the Curie-law magnetization.
In our case, only a single, extremely small spin signal will be measured, therefore the detector noise is expected to dominate, as such we assume $\sigma_{detector} \gg \sigma_{spin}$. Furthermore, we use the power SNR ($\propto \sigma^2$) instead of the amplitude SNR ($\propto \sigma$) so statistical fluctuations can be described correctly and the SNR is independent of the sign of the initial magnetization.
Here, we discuss the situation as displayed in Fig. 2.4: signal averaging based on our experimental setup. A lock-in amplifier separates the signal so a two-channel PLL can decompose the signal such that the in-phase channel (X) contains the spin signal plus noise, while in the quadrature channel (Y) only noise appears.[5,10,12,21] For simplicity, the detector noise and thermal noise are combined, which jointly have the variance s_{noise} with a standard deviation σ_{noise}. Because detector noise is white and thermal motion is randomly distributed, the total noise can be considered uncorrelated. The variance of the spin signal follows simply from the difference between the two channels: $s^2_{signal} = s^2_x - s^2_y$. The SNR is then[5]

$$SNR \approx \frac{\sigma^2_{spin}}{\sigma_{s^2_{signal}}} = \left(\frac{n-1}{2}\right)^{1/2} \frac{\sigma^2_{spin}}{\sqrt{2}\sigma^2_{noise}}, \tag{2.9}$$

with n the amount of averages. To arrive at this result a Gaussian distributed noise variance and $\sigma_{s^2_x} \approx \sigma_{s^2_y}$, justified since $s_{noise} \gg s_{signal}$, were used.
Shown in Ref. 5, the factor $\sigma^2_{spin}/\sqrt{2}\sigma^2_{noise}$ is proportional to $n^{-1/4}$ so a single-shot SNR scales only as $n^{1/4}$. This makes significant noise reduction by averaging highly inefficient. Improvements of the SNR should therefore primarily be realized by amelioration of the existing setup, by for example employing high compliance cantilevers with a lower mass and spring constant to decrease noise levels, using nanomagnets for larger field gradients that increase the force signal or creating a large external static magnetic field. These improvements are thoroughly discussed in chapter 3.
Eq. 2.8 is appropriate for the description of signal averaging in a single-spin measurement, however, in a small spin ensemble the autocorrelation time τ_m, i.e. the spin lifetime, has to be taken into account.[27] The configuration of an ensemble dominated by statistically fluctuating spins is correlated for a duration τ_m, therefore the time in between averaging cannot

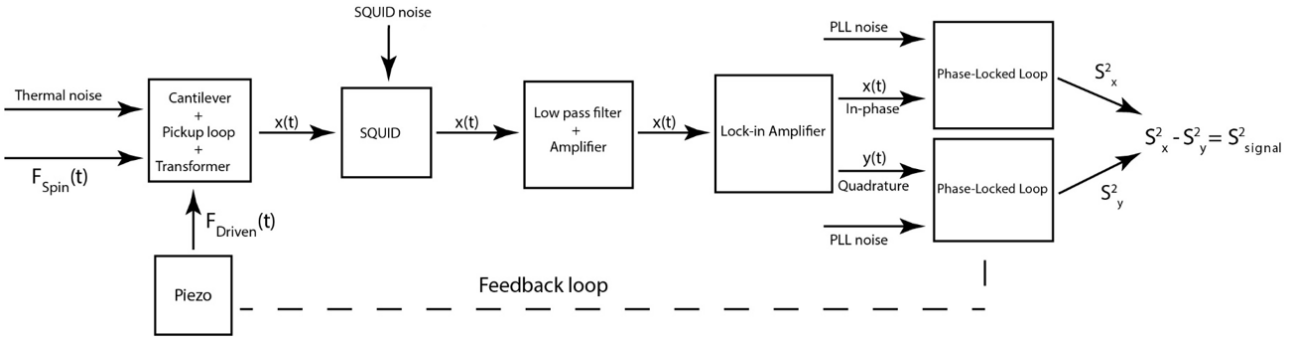

Figure 2.4: *Detection scheme to extract the spin signal. x(t) represents the information hidden in the signal, not the signal itself. For completeness the feedback loop and all intermediate components in the detection scheme are displayed.*

be shorter than τ_m.[7] The precise value of τ_m depends on the magnetic noise, the cantilever amplitude, the sample material and spin species through the rotating frame spin-lattice relaxation time. Nonetheless, to avoid spurious averaging one should at least anticipate a waiting time of on order 1-10 s between consecutive spin signal evaluations.[27]
A rather interesting approach to improve the SNR is to manipulate the statistical correlation time. It was shown that stimulated periodical randomization of spins improves the SNR of a spin ensemble in the statistical polarization regime six times.[21,122]

2.2.2 Measurement protocol comparison

The credo of the last subsection points to the advantages of a measurement protocol that wields adiabatic spin reversals. Further support for the use of ARP-involving protocols is presented in Sec. 2.3 and Sec. 2.5. In short, these sections include the analysis of the required B_1 field and the amount of spins affected by a single shot.
We will start this section with a brief introduction to ARP and thereafter the influence of the pulse shape on the signal and two prominent adiabatic force-gradient protocols, namely oscillating cantilever-driven adiabatic reversal (OSCAR) and cantilever enabled readout of magnetization inversion transients (CERMIT), are reviewed. A comprehensive treatment of ARP can be found in chapter 2 and 6 of Ref. 36 and chapter 2 and 3 of Ref. 35.

2.2.2.1 Adiabatic Rapid Passage

ARP has been broadly used in magnetic resonance experiments to invert the magnetic moment of a spin population. This technique allows one to keep the spin locked along the effective magnetic field B_{eff} for a time of order $T_{1\rho}$[27,119] without decaying due to T_1 processes. Since $T_{1\rho}$ is much longer than T_1 in some materials, the coherence time and interval in which the cantilever experiences a force are equivalently longer, resulting in a larger cantilever amplitude. Additionally, adiabatic pulses preserve the component of the magnetization along B_{eff}, i.e. the tip angle remains constant, regardless of the homogeneity of B_1.
We start with the mathematical formulation of the adiabatic condition and thereafter discuss cyclic adiabatic inversion (CAI) and the effect of an offset frequency on the adiabaticity.

Let us analyze the situation of an alternating magnetic field $B_1(t) = |B_1|cos(\omega_{rf}(t)t)$ along

[7] Decorrelation happens by means of flip-flops, which is mathematically explained by the Wiener-Khinchin theorem.[121]

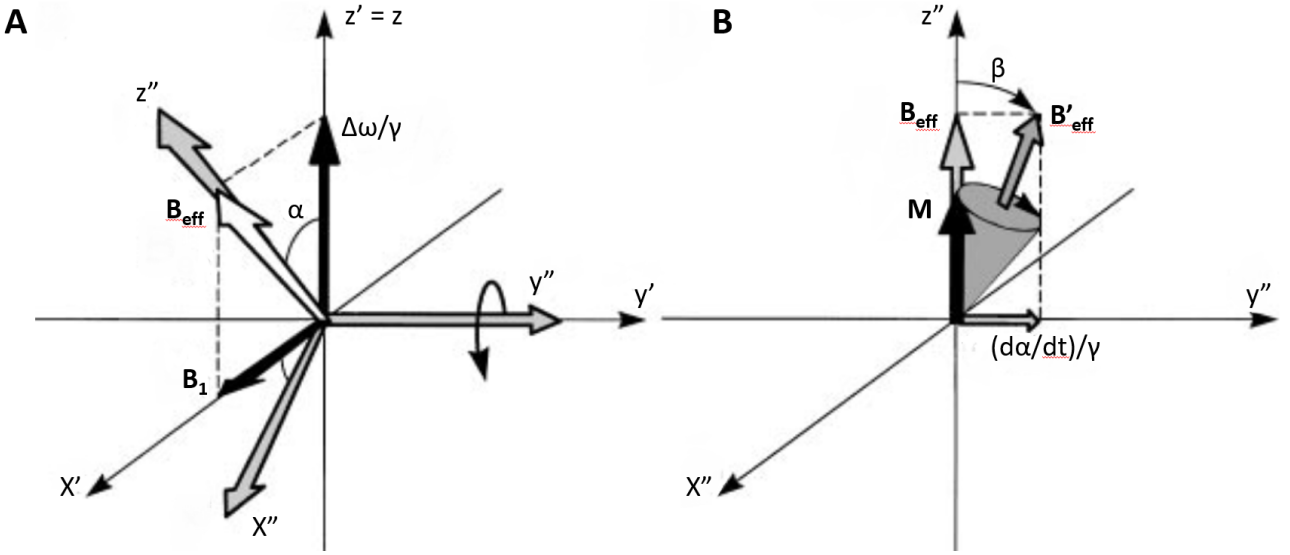

Figure 2.5: *Relation between the two coordinate systems RSC_1 and RSC_2. (a) RSC_1: axes of RSC_1 are labeled as x', y' and z' and axes of RSC_2 are labeled x", y" and z". The precessing magnetic moment and the laboratory system of coordinates are omitted for clarity and brevity, apart from the z-axis, which coincides with the rotating frame z'-axis. The evolution of B_{eff} and B_1 is described in the text. (b) RSC_2: in this frame it can clearly be seen that the component of the magnetization along B_{eff} is conserved during an ARP pulse. Figure adapted from Tannus and coworkers.*[123]

the x-axis in conjunction with a static field B_0 colinear with the z-direction as is the case in every force-sensitive MRFM setup. Here, however, we take the static field B_0 to be only the magnetic field arising from the magnet attached to the cantilever tip, as opposed to the convention of a static field that is composed of the magnet field and a large applied field. The external static field (+$\hat{z}$) in general exceeds the magnet's field (-$\hat{z}$) by at least an order of magnitude at a spin location, therefore the field is directed along the z-axis if B_{ext} is present. To keep this evaluation readily we stick with the literature standard regarding the field directions, nevertheless we note that in reality the direction of our magnet's magnetic field points in the minus z-direction in the currently employed coordinate system.
Ostensibly contradictory, but for simplicity we introduce two rotating systems of coordinates, RSC_1 and RSC_2, shown in Fig. 2.5.

- RSC_1: the axes are labeled x', y' and z'. The rotation axis z' rotates at frequency ω_{rf} and coincides with the z-axis so both B_0 and B_1 are static. Meanwhile, the magnetic moment precesses at the Larmor frequency in a cone around B_{eff}, which is the vector sum of $(B_0 - \omega_{rf}/\gamma)\hat{z}$ and $B_1\hat{x}$. B_{eff} changes its direction according to the time evolution of the angular velocity $\Omega(t) = d\alpha(t)/dt$, where α is the angle between B_{eff} and the z'-axis given by $\alpha(t) = arctan(\gamma B_1(t)/\Delta\omega(t))$, with $\Delta\omega(t) = \omega_0 - \omega_{rf}(t)$.

- RSC_2: the axes are denoted as x", y" and z". This frame is especially convenient to describe the magnetization vector M or equivalently the magnetic moment μ, because B_{eff} is static. RSC_2 rotates within RSC_1 at the rate $\Omega(t)$ with its z"-axis along B_{eff} and y"-axis aligned with y'. The new effective magnetic field, B'_{eff}, is the sum of B_{eff} and the field parallel to y", having the magnitude $\frac{d\alpha(t)}{dt}/\gamma$. The size of β, the angle between B_{eff} and B'_{eff}, is an indication of the magnetization left after a cyclic inversion. $\beta \sim 0$ means practically all magnetization is conserved and the adiabatic condition is fully satisfied.

The tipping angle is defined as the final angle between RSC_1 and RSC_2 after an ARP pulse.

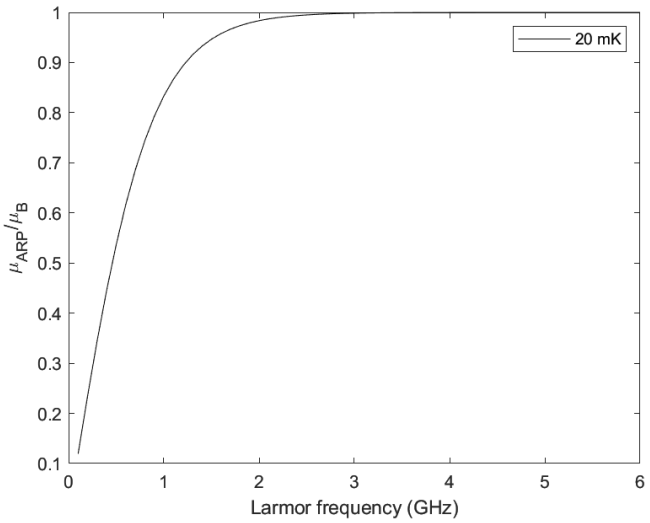

Figure 2.6: *The effective magnetization during an inversion, defined as μ_{ARP}/μ_B and only valid for thermalized spins (Sec. 2.2.3.1), is computed as function of the Larmor frequency at 20 mK.*

Furthermore, it is assumed that the initial orientation of the magnetic moment is along B_{eff}, which is in the B_0 direction, justified since $B_1 \ll B_0$.
The magnetization effected by an ARP pulse throughout the spin inversion process depends on the Larmor frequency of the resonant spins. Depicted in Fig. 2.6, at 20 mK and for Larmor frequencies larger than 2 GHz, the net magnetization effected by an adiabatic reversal is nearly saturated at the Bohr magneton value.

If the change in B_1 is slow enough in time then the spin follows B_{eff}, leading to a spin inversion. More precisely, this is the case when the following holds for all t

$$\frac{d|\alpha(t)|}{dt} \ll |\gamma \mathbf{B_{eff}}(t)|. \tag{2.10}$$

This is the familiar adiabatic condition. It is desirable to include spin-spin and spin-lattice interactions in the condition to represent experimental circumstances. The duration of a spin reversal $1/\Omega \ll T_2 \leq T_1$ and $B_1 \ll B_0$, so inequality 2.10 reads

$$\frac{1}{T_2} \ll \frac{d}{dt} arctan\left(\frac{\gamma \mathbf{B_1}(t)}{\Delta\omega(t)}\right) \ll |\gamma \mathbf{B_1}(t)|. \tag{2.11}$$

It is now evident that ARP pulses allow a rapid frequency sweep, which make them both applicable in pulse sequences for force based approaches and in force-gradient based protocols. From the definition of α(t) follows that adiabatic pulses can be amplitude modulated (changing $|B_1|$) and frequency modulated (varying $\Delta\omega$ through ω_{rf}).
Further elaboration of inequality 2.11 depends on the magnitude of B_1. Namely, for solids, the magnetization no longer obeys the Bloch equations[55] if $|B_1|$ is far above the saturation level.[124]

Cyclic adiabatic inversion

In essence, CAI[119,125,126] is a train of repeated ARP pulses that cause periodic inversion of the longitudinal magnetization. The z-component of the electron magnetization is locked parallel (if $B_0 - \omega_{rf}/\gamma > 0$) or antiparallel (if $B_0 - \omega_{rf}/\gamma < 0$) to B_{eff} (Fig. 2.5).

Let $\Delta\omega$ be the frequency modulation of the rf field that consists of a frequency dependent wave form with an amplitude Ω. The wave form significantly influences the spin inversion profile and transfer of magnetization. This is the topic of Sec. 2.2.2.2, where we also discuss the wave form best suited for single-spin detection. Without specifying the wave form, M_z can be written as[119]

$$M_z = \widetilde{M}(t)\frac{\Delta\omega(t)}{\sqrt{(\Delta\omega(t))^2 + (\gamma B_1)^2}}, \tag{2.12}$$

where $\widetilde{M}$ is the amplitude of the magnetization. A time dependency was included to indicate that the magnetization magnitude is a function of time, however, in general, the time-dependent change is very small compared to the frequency modulation.
CAI is only viable if $T_{1\rho}$ is long enough to enable the creation of a cantilever amplitude large enough to be detectable. Other mechanisms that lead to magnetization decay are spin-spin relaxation, rotating frame cross relaxations and poor adiabaticity.[125]

A remark on offset resonance

If a resonance offset is present due to variations in the B_1 field the adiabatic condition alters slightly.[11] Let C be the adiabatic accuracy parameter and $\Lambda = \gamma\Delta B$ an offset frequency, then, at the most critical moment, namely resonance (t_{res}), the adiabatic condition translates to the following inequality

$$C(t_{res}) = \frac{\gamma \mathbf{B_1}(t_{res})}{\dot{\Lambda}(t_{res})} \gg 1 \tag{2.13}$$

The offset is typically very small, because resonant slices in MRFM are extremely thin. In other techniques, such as MRI and NMR, offset independent adiabatic pulses play a vast role.[123]

2.2.2.2 Pulse shapes and protocols

Pulse shapes occur in many different forms, e.g. B_1 insensitive rotation,[11,123] π compatible,[127,128] Gaussian,[129] phase modulated[130] and sin/cos pulses. The shape has a far-reaching influence on the spin inversion fidelity and the carry-over of magnetization during an ARP pulse. It is of importance to optimize both to provide a large spin signal, however, this is contingent on the specimen's relaxation times and the exact experimental settings, such as the tip-sample spacing, magnet and cantilever properties.

The on-resonance transfer of magnetization can be modeled by[131,132]

$$M_{before} = M_{after} e^{-\frac{K}{T_2}}, \tag{2.14}$$

where M_{after} is the magnetization left after an ARP pulse and K is an unphysical pulse-shape dependent parameter roughly comparable to the single pulse duration. The product of the bandwidth and K is a measure of the pulse sensitivity to short T_2 times.
The factor $exp(-K/T_2)$ is the chance to invert a single spin. In order to create sufficient

signal, the spin inversion success rate during a sequence of ARP pulses[8] should be approximately 99.99%,[10] which directly leads to a limitation on K, namely $K < 10^{-4}T_2$.
In the previous force experiment in our group[10] K did not satisfy the aforementioned condition. This has profound consequences for the feasibility of a force-based experiment, since the average longitudinal magnetization rapidly reduces towards an undetectable level for $K > 10^{-4}T_2$. The left-over longitudinal magnetization, labeled M_{ARP} at time t after a number of spin flips scales as follows

$$< M_{ARP}(0)M_{ARP}(t) > \propto e^{-t/\tau_m}, \tag{2.15}$$

where a pulse length $t_{pulse} \ll T_2$ was assumed so cross relaxation can be ignored.[133] $\tau_m = \frac{\pi T_2}{\omega_s K}$, with $2\omega_s/2\pi$ the spin reversal frequency and ω_s the frequency of a spin undergoing 2 ARP pulses, i.e. the frequency of 2*180° = 360° rotations. The autocorrelation time establishes the borderline between the statistical and thermal polarization regime. More specifically, for the duration $T_{experiment}$ of an experiment, statistical polarization dominates if $\tau_m \ll T_{experiment}$, whereas thermal polarization prevails if $\tau_m \gg T_{experiment}$.

Secant pulses

To enable force-based measurements, we propose to use the hyperbolic-secant (HSn) pulse, which is known for its exquisite spin inversion profile in a small bandwidth, robust insensitivity to dephasing as a result of spin-spin dipole interactions and negligible response to deviations in the strength of B_1.[17,131,134–136] Due to the spatial focus of the pulse all spins within the inverted region have a nearly equal Larmor frequency offset, thereby increasing the total force output on the cantilever. For unambiguous single-spin detection, however, the short on-resonance time, i.e. the inversion moment, relative to the total sweep time is of greater relevance. This ensures a minimal loss of magnetization due to the component in the transverse plane.[11,124]
HSn pulses require both frequency modulation by $tanh(\beta t^n)$ and amplitude modulation by $sech(\beta t^n)$ of the rf-field, where β and n are control parameters that regulate the truncation and slope of the modulation.

OSCAR

OSCAR was invented by Stipe *et al.*[18] and is the protocol that was used to detect a single spin[8] among numerous other ESR and NMR experiments.[23,27,104] The requirement for this protocol is $T_{1\rho} \gg T$, with T is the cantilever period. A rule of thumb is $T_{1\rho} \gtrsim 100$ ms in order for OSCAR to be viable.[5] In short, the protocol works as follows

- The piezo elements drive the cantilever in an abiding self-oscillation according to the feedback scheme depicted in Fig. 2.4.
- The rf source is at first turned off so more spins can align along the field of the magnet (assuming no external field as in our setup), thereby increasing the polarization.
- Subsequently, a continuous rf field is switched on synchronized with the cantilever's peak position, as such, maximizing the displacement.

[8] A typical pulse sequence consists of hundreds to thousands pulses and has a total length on the order of $\frac{Q}{f_c}$. Much longer or shorter sequences are not advantageous as described in chapter 4 of de Voogd's thesis.[10]

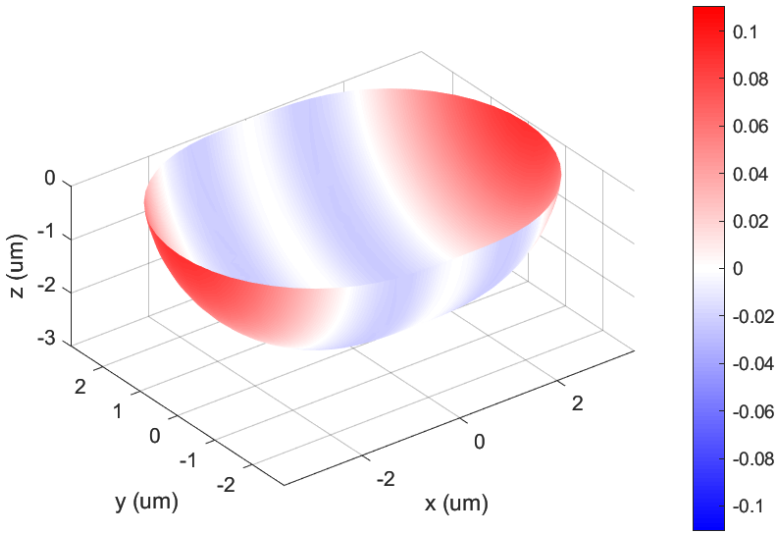

Figure 2.7: *Resonant slice corresponding to ω_{Larmor} = 2.5 GHz. The movement of the cantilever is in the x-direction. The colors represent the contribution of spins to the total frequency shift of the cantilever.*

- Due to the cantilever movement, the resonant slice oscillates through the sample. As a consequence, this induces synchronous cyclic adiabatic spin inversions (Sec. 2.2.2.1) of the spins located in the volume subject to cantilever motion.
- The spins produce a back-reaction force that alters the response force from feedback. This effectively results in a shift of the spring constant, which manifests itself as a change of the cantilever frequency.

The contribution of spins to the total frequency shift depends on their position relative to the cantilever (Fig. 2.7).[137] Spins directly under the cantilever do not interact, whereas spins on the side of the resonant slice in the cantilever displacement direction provide the largest oscillating force. Consequently, the OSCAR protocol requires an asymmetric amount of spins on either side of the cantilever, which could be a cumbersome requirement in the statistical regime.
Assuming a cantilever amplitude far below the tip-sample distance, the single-spin frequency shift is[137,138]

$$\Delta f_{OSCAR} = \mp \frac{2 f_0 M_{eq}}{\pi k A_{pk}} |\mathbf{B}'_{||\hat{\mathbf{B}}_0}(r)|, \tag{2.16}$$

where the - corresponds to spin-lock and the + to spin-antilock, k is the spring constant, A the peak cantilever amplitude and M_{eq} the average magnetization during an adiabatic spin inversion.

Later on, more sophisticated forms of OSCAR were developed. In iOSCAR,[8] or interrupted OSCAR, the rf field is turned off every half a period, switching the relative phase of the spins by reversing the locked and the antilocked spins. As a result, the signal will be composed of a symmetric periodic alternating frequency shift that imitates a square wave function and some inhomogeneity due to quantum jumps (Sec. 1.5).[56]
On the other hand, partially interrupted OSCAR,[23] abbreviated as piOSCAR, truncates the interruption to a duration less than half the cantilever period. Hereby a higher sensitivity is reached at the price of a reduced detection volume.

CERMIT

Since it is presumed that the nuclear $T_{1\rho}$ is longer than T_1 in many materials, Kuehn *et al.*[5] devised a new approach, called CERMIT, that only demands $T_1 \geq T$, with T the cantilever period and does not enforce a rotating frame spin-lock to detect a signal. In a nutshell, the protocol is operated as follows

- The core principle of the protocol: a magnet attached to the cantilever tip is coupled to the longitudinal component of the magnetization (Curie-law or statistical) of the spin bath. A high polarization is essential to generate a clear discrepancy between inverted spins and the spin bath. For this, an external static magnetic field perpendicular to the cantilever motion should be applied. Due to the high polarization flip-flops are suppressed, therefore the force-gradient can be considered constant and only differs between the inverted slice and the spin bath.
- In order to evade the problem of canceling force-gradients due to a roughly symmetric spin distribution around the cantilever tip (Fig 2.7) a single frequency modulated ARP pulse is emitted so a small slice of spins is inverted.
- The reversed spins are antilocked compared to locked spins in the spin bath or vice versa and have a uniform sign if a suitable slice is chosen.
- The force-gradient difference between the initial (before the pulse) and final state (after the pulse) changes the spring constant. The resulting shifted cantilever frequency exponentially decays to its natural frequency with a ringdown time equal to the characteristic T_1 time in which the longitudinal magnetization returns to the pre-pulse value.

Under the same approximation as for the frequency shift in OSCAR, namely a small cantilever amplitude relative to the tip-sample distance, the single-spin induced change of the cantilever frequency is[138]

$$\Delta f_{CERMIT} = -\frac{f_0 M_{eq}}{2k} |\mathbf{B}''_{||\hat{\mathbf{B}}_0}(r)|. \tag{2.17}$$

The major difference is the dependency on $\mathbf{B}''$, whereas Δf_{OSCAR} is a function of $\mathbf{B}'$.

A particularly interesting advantage of CERMIT for MRFM at millikelvin temperatures is the low duty-cycle as a result of the single ARP pulse. Given that the rf field is the main source of cantilever heating, any potential reduction is a serious improvement of the SNR. Furthermore, a minimal detection bandwidth similar to $1/T_1$ compared to $1/T_{1\rho}$ for OSCAR also favors CERMIT.
Nonetheless, the high sensitivity to $1/f$ surface noise could possibly nullify all the previous mentioned benefits. Additionally, so far, no experiment reached the full theoretical spin coherence time, suggesting the need for further improvement of the protocol.[139]

Proposed protocols

Although no $T_{1\rho}$ of P1 centers was measured to the authors knowledge we can safely assume it is longer than 100 ms, since several OSCAR experiments were performed on diamond.[10,23]
To conclude this section: we propose to use ARP pulse trains having a HSn wave form for a force based measurement if a micrometer sized magnet is employed and piOSCAR, a force-gradient based protocol, if a nanometer sized magnet is utilized, since these choices yield the highest single-spin SNR.

2.2.3 The first step: frequency shifts as a result of various ARP pulse trains

As explained in Sec. 2.2.1, measuring a force signal is for various reasons more complicated than detecting a force-gradient signal. A logical first step towards a successful force based CAI measurement (sequence 3) is the detection of a frequency shift, induced by an ARP based protocol. In this section we pave the way for the latter mentioned experiment by calculating the expected frequency shift from bulk and surface spins for two ARP pulse trains (sequence 1 and 2) at a tip-sample separation of 500 nm.
For simplicity, we merely use a heuristic model to calculate the frequency shift Δf. A more complete theory was developed by de Voogd *et al.*[108] that includes the influence of the cantilever on the spin dynamics. Nevertheless, as a sanity check, we compare the results from our fast-approach calculation with simulations based on de Voogd's theory.

2.2.3.1 Proposed pulse sequences

In detail, the three proposed sequences are

1) *Sequence 1*: It is presumable that the signal due to a single pulse is smaller than the frequency noise, therefore we propose to send N = 50 ARP pulses modulated at different frequencies and with a total time $NT_{pulse} < T_1$. This sequence results in the generation of 50 resonant slices. The cumulative frequency shift is measured for these N slices.

2) *Sequence 2*: Similar frequency modulation as in sequence 1, but in this case, 50 resonant slices are addressed by 50 pairs of consecutive ARP pulses. The first pulse inverts the spin's magnetic moments and the magnetization returns to its initial value as a result of the second pulse. The time between the two pulses must be shorter than the flip-flop time: $\Delta t < T_{ff}$ ($T_{ff} \simeq 55$ ms, Tab. 2.1). The expected signal strength is smaller than for sequence 1, because of the magnetization loss (Sec. 2.2.2.2). If the observed signal is indeed smaller, one may conclude that the cantilever frequency shift of sequence 1 is not due to heating.

3) *Sequence 3*: If the heating is negligible then one may send 1000 consecutive ARP pulses in 500 cantilever cycles, i.e. 2 ARP pulses per cycle, that all address the same slice. The force is measured at the cantilever's natural frequency during the pulse train. Likewise as for sequence 2, the exigency of long flip-flop times might be too stringent to successfully perform this sequence.

Sequence 2 serves as a control experiment for sequence 1 to examine whether potentially observed heating effects are spurious or real. In sequences 1 and 2 the frequency is swept through the sample, in contrast to sequence 3. Sequences 1 and 2 form the groundwork for the more advanced sequences 3, which is a typical CAI sequence.

The spin-lattice relaxation time of bulk spins is expected to greatly exceed the cantilever period as explained in Sec. 2.1.3. The duration of T_1 is of importance in all protocols, because the electrons have to fulfill the following condition[108,140] to ensures a well defined spin temperature (only valid for spin-$\frac{1}{2}$ particles)

$$\pi\gamma^2|\mathbf{B_1}(\omega)|T_1 g(\omega) \ll 1. \tag{2.18}$$

Here, $g(\omega)$ is the normalized shape of the absorption line. A further relevant consequence of long T_1 times is the limited influence from spins on the cantilever's Q-factor.
If the relaxation rate turns out to be on the order of the cantilever's resonance frequency,

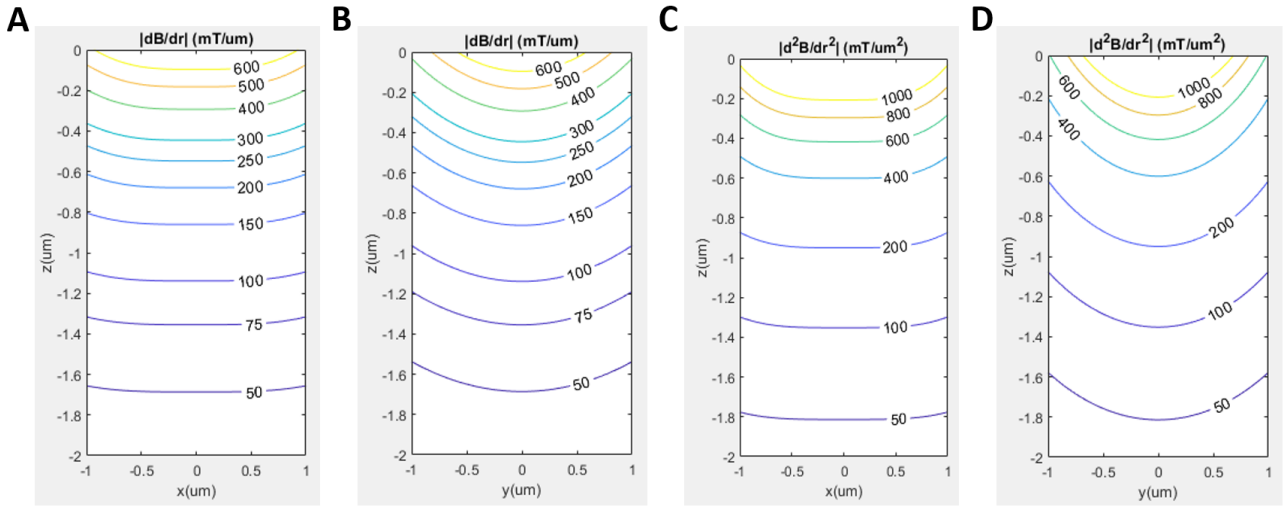

Figure 2.8: *Plots of the first (a and b) and second gradient (c and d) of the tip's magnetic dipole field (Eq. 2.20) with respect to the radial direction from the magnet. In these calculations, z is the tip-sample height, where (0,0) is the surface of the magnet. The magnetic field is plotted in the x-z plane (a and c) and the y-z plane (b and d).*

interrupted CAI (iCAI) could be used to circumvent the problem of detrimental spin relaxation times. An additional issue could be the set duration of T_{pulse}, because the exact T_1 time is unknown and T_{pulse} must be shorter than T_2. The expediency of a certain pulse duration greatly depends on the tip-sample separation as visible in Fig. 2.3, which partly determines the T_2 time.

Sinusoidal wave forms can be employed for simplicity in sequence 1 and 2, but a more sophisticated approach is required for sequence 3. As described in chapter 4 of de Voogd's thesis[10] sinusoidal wave forms are not beneficial for CAI experiments due to the loss of magnetization, therefore we suggest to use HSn or Lorentzian pulses.

2.2.3.2 Frequency shift calculation

In our model the spin-cantilever interaction is characterized by a stiffness k_s. Starting from the potential interaction energy $E = -\mu \mathbf{B}(\mathbf{r})$, the exerted force and stiffness k_s follow from the first and second derivative of B(r) with respect to the cantilever's direction of movement, respectively. The frequency shift caused by a single spin is then (for a derivation see Sec. 1.2.2)

$$\Delta f = \frac{1}{2}\frac{k_s}{k_0} f_0, \tag{2.19}$$

with $k_s = \mu \frac{d^2 B}{dx^2}$ and, k_0 and f_0 the cantilever stiffness and frequency, respectively. Summing over all the spins in a resonant slice yields the total frequency shift.

Since the frequency shift Δf is a function of the magnetic field strength, it indirectly depends on the tip-sample distance. In our analysis we assume sufficient coupling between the spin magnetic moment μ and the magnetic field B(r) of the cantilever's magnet tip for a detectable change in the natural resonance frequency. This is satisfied as long as the tip-sample spacing stays below ~2.5 μm.[19]

Magnetic dipole approximation

The employed magnet is to a high approximation spherical, therefore we consider the magnetic field as to arise from a point source, whose field is by definition a magnetic dipole field. This field is given by

$$\mathbf{B}(\mathbf{r}) = \frac{\mu_0}{4\pi}\frac{1}{r^3}[3\hat{\mathbf{r}}(\mathbf{m}\cdot\mathbf{r}) - \mathbf{m}], \tag{2.20}$$

where r is the radial direction from the magnet and m the magnetic moment. As visible in Fig. 2.8, the gradient fields in the direction parallel to the cantilever's direction of movement (x) differ slightly from the perpendicular direction (y).
At a tip-sample separation of roughly 500 nm: $\frac{d^2B}{dx^2} \simeq 5 \cdot 10^{11}$ T/m^2 (Fig. 2.8c). Using the values from Tab. 2.1, we find that the single-spin induced frequency shift is ~0.1 mHz.

Bulk and surface resonant slices

In anticipation of the discussion about the shape of the resonant slice in Sec. 2.5.2, we use the results presented there to analytically calculate the thickness of surface resonant slices from which we derive the total amount of spins inhabiting a slice. On the other hand, the amount of spins located in a bulk resonant slice is computed numerically. For both situations typical pulse settings are used to imitate the experimental situation.

As we will see in Sec. 2.3, the minimal required B_1 field strength to send ARP pulses is ~3 μT. For simplicity we take B_1 = 10 μT in our calculation, which is still small enough to not cause significant heating.
From Fig. 2.9c we deduce $\omega_L = \gamma B_0 \simeq 5.6$ GHz at a tip-simple distance of 500 nm. A pulse would thus be send at the Larmor frequency and be frequency modulated with $\omega_{rf} = \gamma B_1 \simeq$ 250 kHz. Numerically calculating the spins in a resonant slice created by this pulse results in Fig. 2.10a. Multiplying the number of spins in a resonant slice at ω_L = 5.6 GHz with the frequency shift per spins yields the bulk frequency shift. In conclusion, the bulk frequency shift as a result of 1 ARP pulse (sequence 1) or 2 ARP pulses (sequence 2) is ~0.5 mHz.

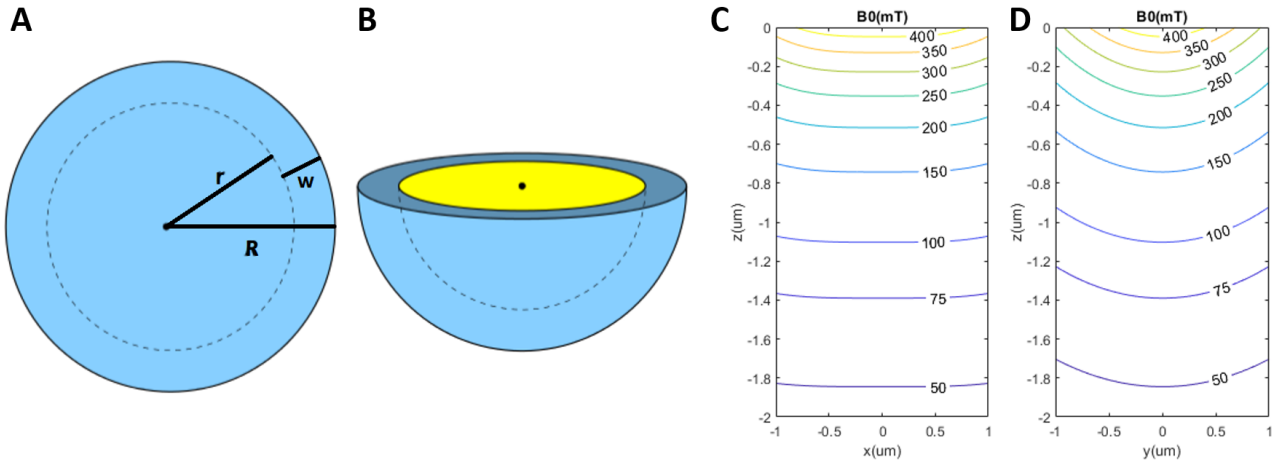

Figure 2.9: *Schematic overview of the surface (a) and bulk (b) resonant slice. Both slices have a thickness w given by Eq. 2.21. Plots (c) and (d) show contour lines of the B_0 field in the x-z and the y-z plane, respectively. In these calculations, z is the tip-sample height, where (0,0) is the surface of the magnet.*

A circle shell of thickness w closely resembles the shape of surface resonant slices (Fig. 2.9a). The thickness w is given by[22]

$$w \simeq \left(\frac{d\mathbf{B}}{dx}\right)^{-1} \frac{\Omega}{\gamma}, \tag{2.21}$$

where Ω is the peak-peak frequency amplitude of the modulated B_1 field. Using Fig. 2.8a, $\frac{dB}{dx} \simeq 0.25\,\mathrm{MT/m}$ at a tip-sample spacing of 500 nm. The contribution of the diffusion length L_D (Tab. 2.1) to w, omitted in Eq. 2.21, leads to a broadening of 3 nm in all directions. Equal frequency modulation as for bulk slices and taking the diffusion length into account results in a slice thickness of roughly 6 nm.

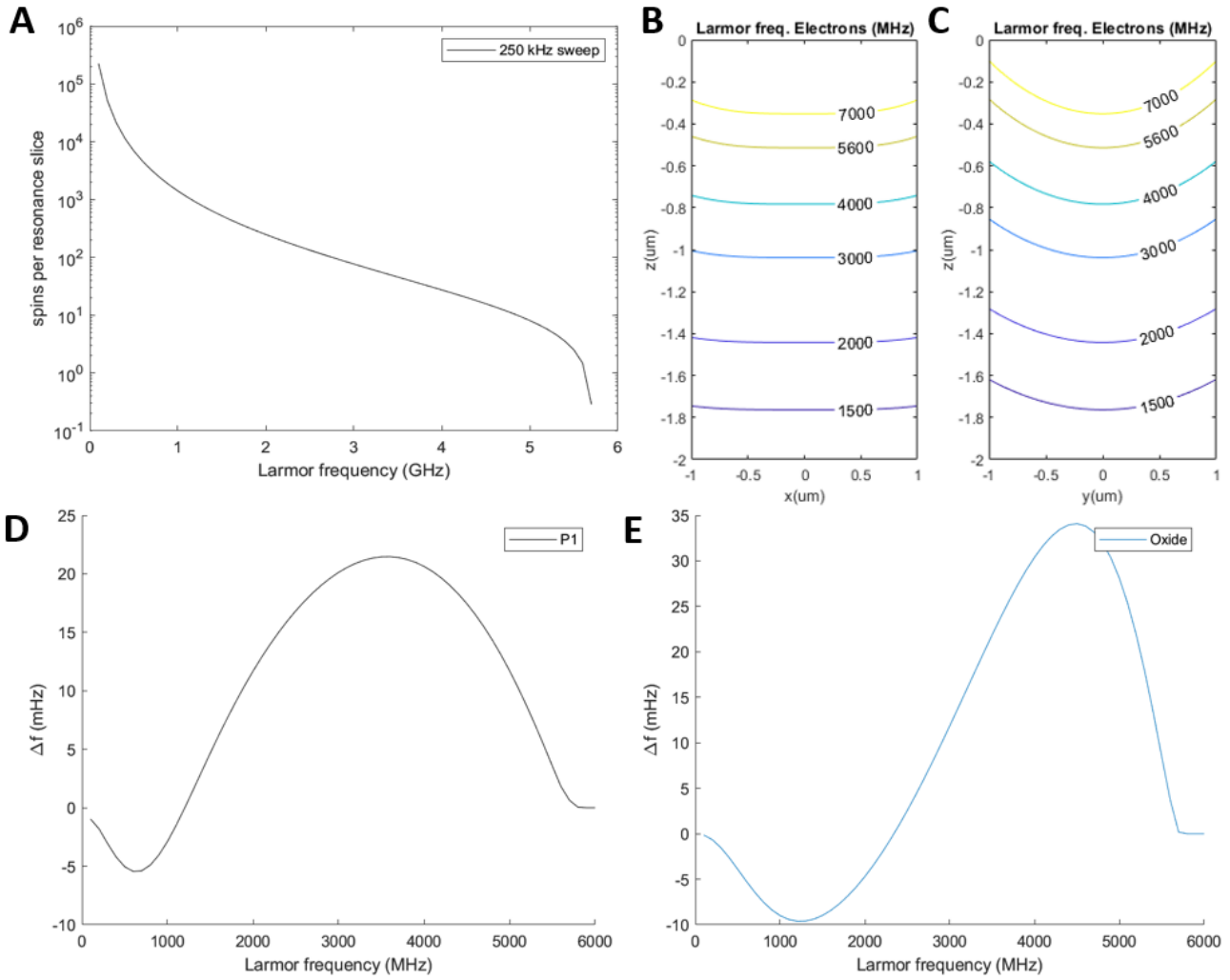

Figure 2.10: *a) Plot showing the dependency on the Larmor frequency of the amount of spins in a resonant slice created by a 250 kHz frequency modulated pulse. The rapid reduction of resonant spins with a Larmor frequency close to 6 GHz is a consequence of these spins being too close to the cantilever. b,c) The Larmor frequency as function of the electron position relative to the tip magnet in the x-z plane (b) and the y-z plane (c). In this simulation, z is the tip-sample height, where (0,0) is the surface of the magnet. d,e) Calculations of the bulk frequency shift of P1 centers (d) and surface frequency shift of free electrons emanating from oxide dangling bonds (e) as function of the Larmor frequency for a resonant slice of 6 nm thickness at 20 mK and a tip-sample separation of 500 nm. An equal thickness of the bulk and surface slice was chosen to enable quantitative comparison. The spin-cantilever interaction k_s was computed based on formulas 10-12 in Ref 108. The T_1 time was taken to be infinite for P1 centers and $1/\omega_0$ for oxide dangling bonds.*

The area $A_{surface}$ of a surface slice is (Fig. 2.9a)

$$A_{surface} = \pi \left[R^2 - r^2\right] = \pi \left[R^2 - (R-w)^2\right] \simeq 2\pi R w. \tag{2.22}$$

To arrive at the last step $w \ll r < R$ was assumed. An estimate of R can be extracted from Fig. 2.10b, i.e. the distance in the x and y direction for which the Larmor frequency is 5.6 GHz at a tip-sample separation of 500 nm. Since we base our analysis on a circular shaped resonant slice, the smallest length was used in the calculation. The length along the y-axis imparts $R \simeq 0.5\ \mu$m.
Together with w = 6 nm this yields $A_{surface} \simeq 7.85 \cdot 10^{-14}\ m^2$. For a surface spin density of $7.2 \cdot 10^{16}$ spins$/m^2$ (Tab. 2.1) the surface frequency shift is ~0.1 Hz.

The sample was cleaned exhaustively by predecessors[19] before use in previous experiments, therefore we assume that the contribution of diamond impurities to the surface frequency shift is negligible. The exposure to air, however, leaves a layer of oxide on top of the sample that disturbs the signal from diamond impurities. The actual culprits are the abundance of valence electrons of oxygen atoms and the lack of neighboring atoms to create covalent bonds. The unpaired electrons are referred to as dangling bonds, or more specifically in the case of our oxide layer, free immobilized radicals.
The frequency shift of a surface slice is substantially larger than that of a single bulk slice, especially at high Larmor frequencies. The suggested amount of emitted ARP pulses, or equivalently, the amount of created resonant slices, is only an indication. By increasing the amount of generated slices the bulk frequency shift will dominate due to the sheer amount of bulk slices. Alternatively, although harder to accomplish, one could choose to avoid disturbing surface signal by only generating bulk slices.

Frequency noise floor

To enable a successful measurement the signal has to transcend the frequency noise floor. Similar as for force noise (Sec. 2.2.1), the total power spectral density $P_{\delta f}(f)$ of the frequency noise can be found by adding the thermal noise, 1/f noise and all different detector noise[25]

$$P_{\delta f}(f) = P_{\delta f}^{thermal} + P_{\delta f}^{det} f^2 + P_{\delta f}^{sample} f^{-1}. \tag{2.23}$$

The $1/f$ noise is conjectured to originate from sample dielectric fluctuations that are especially disruptive at low frequencies.[20,141,142] As described in Sec. 2.4.1 and Sec. 2.2.1, most detector noise stems from voltage fluctuations that scale as f^2 and dominate the high frequency noise range.[142,143]
The total frequency noise in a 1 Hz detection bandwidth for a Q-factor of about 5000 is roughly 2 mHz.[25] From this we conclude that a pulse train, creating dozens of bulk resonant slices, generates sufficient signal to enable the suggested frequency measurements.

Comparison with de Voogd's theory

Both the calculated bulk and surface frequency shift deviate no more than one order of magnitude from the results (Fig. 2.10d,e) that were derived based on the complete analysis of the spin-cantilever environment.[108] For other values of the Larmor frequency the difference may be somewhat larger, however abberations for bulk and surface slices stay within an order of magnitude from de Voogd's theory as long as the Larmor frequency is larger than

~2 GHz for bulk and ~2.5 GHz for surface, respectively. Using Fig. 2.10b, this translates to a critical tip-sample distance of 1.2-1.4 μm. All together, the degree of accordance is sufficient to conclude that the fast-approach method demonstrated here can be wielded without significant loss of accuracy in most practical situations.
There is one important feature that our calculations does not highlight. Namely, the calculated frequency shift based on our simplified model does not differentiate between a positive or a negative change of the cantilever's natural frequency. In general the shift is positive due to the dominant influence of spins that increase the cantilever's frequency (Fig. 2.7).

2.3 Amplitude of B_1 field

In this section we discuss the required B_1 field strength to adiabatically flip a spin. To prevent signal degradation the adiabaticity should be above a certain threshold,[125] which can be accomplished by a strong B_1 field in combination with appropriate frequency modulation of the pulse.
We base our estimate of B_1 on previously conducted experiments in our group and on data from the paper by Poggio and coworkers.[122]
As a reference, the cooling power of our cryostat is ~1.2 mW at 100 mK and our minimal detection bandwidth is 2 Hz.

Data from our group

As onset we take the ARP measurements conducted by de Voogd[10] on the diamond sample we currently use. The relevant experimental settings were: an operational temperature of 100 mK, a magnet diameter of 3 μm, a tip-sample distance of 500 nm and a separation between the spins and the rf-wire of 27 μm. The findings were: 0.63 mA generates around $B_1 \simeq 2.4$ μT, which was sufficient to fulfill the adiabatic condition for each resonant slice. Furthermore, it was deduced that the dissipated power of a pulse is 0.9μW/mA, so 0.63 mA is well-below the maximal cooling power.

Data from Poggio and coworkers

The experimental data of Poggio *et al.* of the rotating frame spin lifetime as function of B_1 is displayed in Fig. 2.11. A minimal detection bandwidth of 2 Hz corresponds to τ_m of 0.5 s.

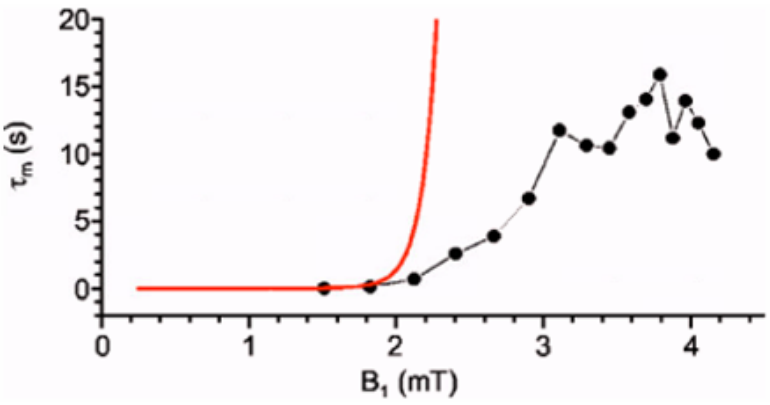

Figure 2.11: *Plot comparing the theoretical limit (red line) of τ_m and a subsequent measurement of τ_m as function of B_1 at 4.2 K for ^{19}F in CaF_2. The calculation was performed by numerically integrating the Bloch equations. Figure reprinted from Ref. 122.*

To compensate for the 700 times smaller gyromagnetic ratio of a ^{19}F nucleus[9] compared to an electron we divide $\tau_m(0.5)$ by 700 to get $B_1 = 2\ \mathrm{mT}/700 \simeq 2.86\ \mu\mathrm{T}$.

Comparison of calculated B_1 values

The two experiments discussed here give comparable results for B_1. This, in combination with our almost identical situation as in Ref. 10 boosts our confidence that the required B_1 strength of roughly 3 μT is not the limiting factor in a single electron experiment.
It should be noted that the cooling power at 20 mK is significantly lower than at 113μW and the sample is only weakly thermally connected to the environment. However, even a hundredfold reduction of the cooling power would still not interfere with the power released during a pulse.

2.4 Cantilever dynamics

In the nanometer realm thermal fluctuations could disturb a measurement in such a way that no distinction between cantilever noise and spin signal can be made, i.e. no image can be created.[117] Moreover, the root-mean-square (RMS) amplitude of thermal cantilever fluctuations, x_{RMS}, has to be well-below the cantilever displacement induced by spins or by feedback control and it is desirable that the RMS amplitude is also substantially smaller than the pulse-caused movement of the resonance slice. Another reason to minimize thermal cantilever movement is the generation of fluctuations in the polarization field of spins.[144] As such, the goal of this section is to calculate and compare the RMS thermal amplitude, driven cantilever displacement and the resonant slice movement to see if a single-spin experiment is possible under current circumstances.

2.4.1 Thermal cantilever vibrations

We start with a brief elucidation concerning FDT,[145–147] the inception point to calculate x_{RMS}, and, furthermore, we explain that the often encountered omnipresent Johnson-Nyquist noise[148,149] elegantly showcases the power of FDT.
First derived by Callen and Welton from first principles,[150] for a system in equilibrium the FDT establishes a relation between thermal fluctuations and an irreversible process. This irreversibility, i.e. an external perturbation, is represented by a response function or generalized impedance. One of the oldest examples of an applied FDT regards the situation of voltage fluctuations, widely referred to as Johnson-Nyquist noise. Present in every electrical system, the agitations are related to the electric charge carriers in conductors. This effect is of great importance, since it could drown out small signals.

From FDT, a general expression for x_{RMS} is[4]

$$x_{RMS} = \sqrt{2\hbar\Delta f coth(\frac{\hbar\omega_0}{2K_bT})|Im(\chi)|}. \tag{2.24}$$

In this equation ω_0 is the cantilever's natural resonance frequency, χ the resonant susceptibility of the cantilever tip and $\Delta f = \frac{\omega_b}{2\pi}$ with ω_b the bandwidth. By using $\chi = i\frac{Q}{k_0}$ with k_0

[9] The gyromagnetic ratio of ^{19}F is approximately 40.05 MHz/T.

the cantilever spring constant and Q the cantilever's quality factor, $\Delta f = \frac{\omega_0}{4Q}$ and assuming $\hbar\omega_0 \ll k_B T$ we can rewrite Eq. 2.24 as

$$x_{RMS} = \sqrt{\frac{k_B T}{k_0}}. \tag{2.25}$$

An identical equation can be derived from the equipartition theorem, which relates the temperature to the average energies of the degrees of freedom present in a system.[151] This approach should be treated with great care at very low temperatures, because its validation breaks down when the energy spacing in a degree of freedom exceeds the thermal energy.

2.4.2 Driven cantilever displacement

Both π-pulses, i.e. a driven displacement by Rabi oscillations, and adiabatic pulses induce spin reversals[10] that exert a force on the cantilever. Provided that a spin experiences adiabatic reversals, the forces it exerts on the cantilever as a result of rf modulation are equivalently described by a series of continuous rf π-pulses with a duration of $\frac{\pi}{\omega_{Rabi}}$ as by a sequence of adiabatic pulses. The asymmetry of the rf source with respect to the geometry of a typical MRFM setup makes π-pulses incompatible with the demand for a homogeneous B_1 field, which is required for driving the Rabi oscillations.
The approach we present here is inspired by the derivation of the driven cantilever displacement in chapter 7 of the book about MRFM written by Berman *et al.*,[4] as such, some results will only be stated. The procedure to find an expression for the driven cantilever displacement is based on π-pulses with a trifling pulse duration[11] compared to the time interval between periodic pulses.

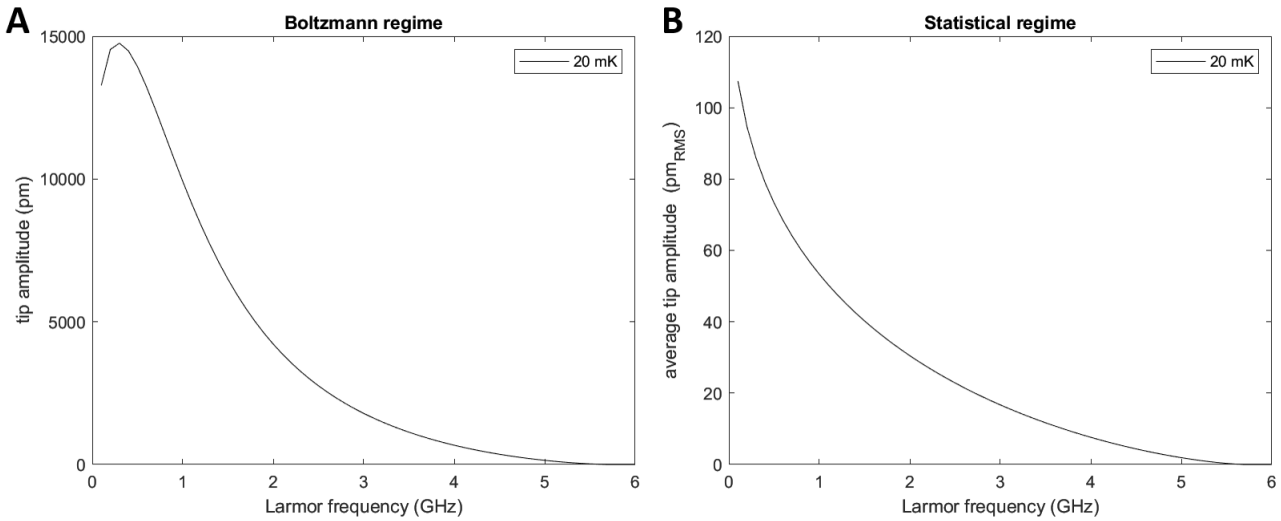

Figure 2.12: *Plots showcasing the theoretical tip amplitude as a result of a single spin inversion as function of the Larmor frequency in the thermalized polarization regime (a) and the statistically polarized regime (b). The borderline between the regimes is as described in Sec. 2.2.2.2. The average tip amplitude in the statistical regime is practically zero as expected, therefore it is customary to measure the standard deviation of the signal (Sec. 2.2.1). Notably, the tip amplitude discussed here should not be confused with x_{RMS}.*

[10] When a static magnetic field B_0 is present, spin reversals could also be generated by modulation of the magnetic field B_0.

[11] The pulse duration is $\frac{\pi}{\omega_{Rabi}}$, so for $\omega_{rabi} \gg \omega_0$ the condition is satisfied.

The formula for the tip amplitude derived here is valid in both the Boltzmann and statistical regime, however the tip amplitude profile, depicted in Fig. 2.12, in both regimes is very different due to statistical fluctuations.

The equation of motion of the cantilever tip is simply that of a driven damped harmonic oscillator. For typical cantilever geometries, displacements perpendicular to the sample are negligible during a lateral deflection, therefore we only treat displacements parallel to the sample. Let x_c be the displacement of the cantilever tip, m its mass, Q its quality factor, ω_0 its natural frequency and F_ω the Fourier component of the magnetic force exerted by a spin acting as an external force, then:

$$x_c(\omega) = \frac{F_\omega / m}{\omega_0^2 - \omega^2 + i\omega^2/Q} e^{i\omega t}. \tag{2.26}$$

Our main focus is the determination of the real part of the amplitude A of $x_c(\omega)$. Given the short pulse duration, the magnetic spin force can be approximated by a periodic rectangular magnetic force F(t) with an amplitude $F_s = |\mu| \frac{dB_0}{dx}$. Subsequently, the Fourier component F_ω can be calculated as an integral of $F(t)cos(\omega_0 t)$ over a single period of F(t), yielding $F_\omega = \frac{4}{\pi}F$. We are solely interested in the resonant case, because at that moment the amplitude is maximal. Setting $\omega_0 = \omega$ results in

$$A = \frac{4FQ}{\pi k_0}, \tag{2.27}$$

where k_0 is the cantilever spring constant. The dependency on the Larmor frequency is included through any variable that is a function of the tip-sample distance.

A remark on the feedback-driven cantilever amplitude

Some protocols require a constant cantilever amplitude. This is generally achieved by mechanical feedback mechanisms that accurately drive the tip amplitude towards a pre-set steady state (Sec. 2.2.2.2 and 2.2.1). Depending on the setup properties and protocol, a typical feedback-driven amplitude ranges somewhere between 1-100 nm.
The optimal cantilever amplitude for a nanomagnet and a force-gradient protocol is discussed in more detail in Sec. 3.3.5.

2.4.3 Shift of the resonant slice

The activation of B_1 results in an offset from equilibrium of the resonant slice, because the resonance condition is altered. Considering that electrons have a Larmor frequency in the GHz range, the resonant slice shift can be seen as a permanent offset during an ARP pulse and for pulse sequences with a rf frequency far above the system's relevant frequencies, i.e. the spin relaxation times and the cantilever modes. The amplitude of the displacement roughly reads

$$\Delta x_{rs} \approx \frac{\mathbf{B_1}}{\frac{d\mathbf{B_0}}{dx}}, \tag{2.28}$$

with Δx_{rs} the resonant slice shift in comparison with B_1 turned off.

2.4.4 Numerical comparison

The values displayed in Tab. 2.1 and Tab. 2.2 are used in the determination of the various displacements at a tip-sample separation of 200 nm and an operating temperature of 20 mK. The size of thermal fluctuations is representative for any tip-sample distance, because its only variables, k_0 and T, remain effectively constant throughout an experiment.
The results are:

- $x_{RMS} = 2 \cdot 10^{-11}$ m
- $A = 4.5 \cdot 10^{-10}$ m
- $\Delta x_{rs} \approx 2 \cdot 10^{-11}$ m

Although A and Δx_{rs} do change a little at a different tip-sample spacing, the illation does not change.
In conclusion, the displacement of the cantilever caused by a single spin greatly exceeds the size of thermal fluctuations, thereby enabling single-spin detection. The shift of the resonant slice, although comparable in size to x_{RMS}, can be neglected in most situations.

2.5 Thickness of the resonant slice

The number of spins inhabiting a volume depends on the spin concentration and their local spreading. A precise determination of the spin distribution is impossible and even including disordering turns out to be often too complicated, consequently we made an assumption for the spin distribution and discuss its validity. Thereafter, we treat the imposition of the slice thickness condition that we partly derive from the spin distribution.
The resonant slice thickness is an important experimental variable, since it confines the achievable resolution. Subsequently, it is an indication for the expected number of spins in the resonant volume, which determines the strength of the magnetic resonance signal.

2.5.1 Spin distribution

The location of crystal atoms is restrained to their lattice site, however impurity spins can be deemed free spins (Sec. 2.1.1) being therefore only partially restricted in their movement. This substantiates the choice for a random spin distribution. Nonetheless, random sampling allows infinitely small separations that are in reality prohibited by repulsive electron-electron interactions[152,153] due to Pauli exclusion principle, enforcing a minimal interspin

Table 2.2: *Overview of parameters used to calculate Δx_{rs} and A*

Parameter	Variable	Value
Radio frequency magnetic field	B_1	10 μT
Magnetic field gradient of the magnet	$\frac{dB_0}{dx}$	0.5 MT/m
Single-spin force	F_s	5 aN

The quality factor and magnetic field gradient belong to a tip-sample spacing of roughly 200 nm. The spin force equals the maximal exerted force during a spin reversal. For simplicity $B_1 = 10\,\mu$T was used.

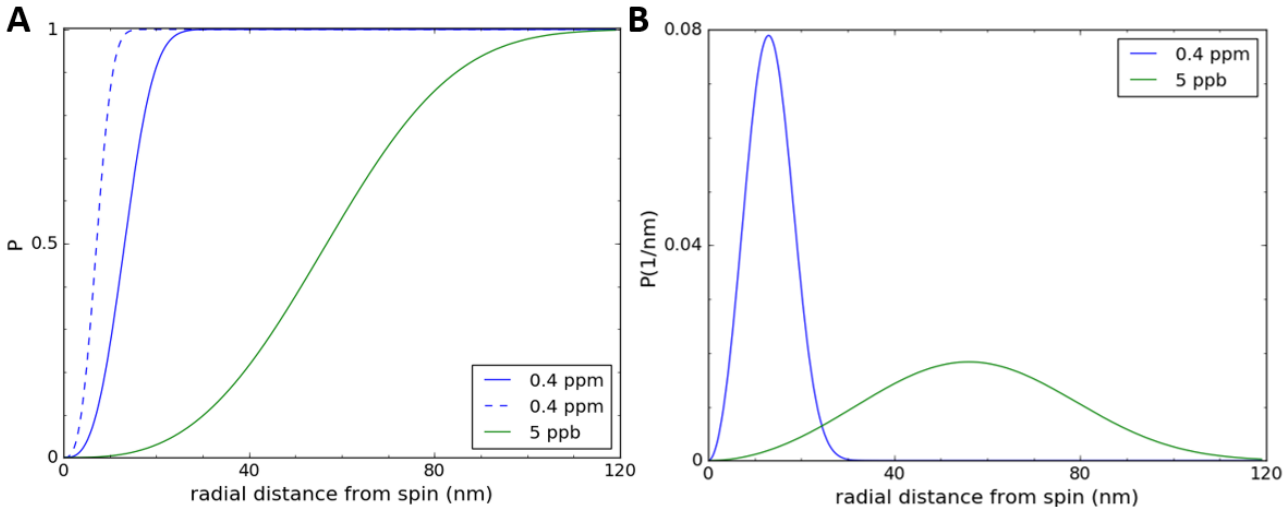

Figure 2.13: *Plots showing the probability (a) to find a nearest neighbor impurity spin within a distance r for uniform randomly distributed spins and the probability density (b) of the same distributions. The concentration of nitrogen impurities corresponds to our current sample (0.4 ppm) and a commercially available diamond sample from Qnami (5 ppb). The dashed line represents the probability distribution of spins having an average interspin distance opposed to a maximal.*

distance. Hereby, the validity of a random distribution is reduced to a cutoff proportional to the repulsion strength. A pertinent indication for typical minimal spin-spin distances is the length of a C-C bond or the C-N bond, which is of comparable length. High accuracy X-ray measurements impart a C-C bond length of 0.154 Å,[154] which is also a fundamental resolution limit for any electron imaging technique.
Only samples with a spin density having a non-zero probability to find a nearest neighbor within a single bond-length for random uniform distributed spins are excluded. Even taking into account the disparity between lone pairs and bonding electron pairs and that C-N bonds housing the unpaired paramagnetic electron are extended by roughly 10%,[82] the critical impurity concentration still lies above 80%.

In practice every monster also includes local inhomogeneities,[155] e.g. clustering because of a preferred geometry of a conglomerate impurities and differences in interaction strength between and within centers.[156] Since the length scales at which these effects play a role are small we can safely neglect their impact on the analysis of the spin distribution of a millimeter sized specimen.

The tenet from the above reasoning, that an uniform random spin distribution can be assumed without noteworthy loss of generality, was applied here. The probability for such a distribution to find a nearest neighbor within a distance r is given by

$$\mathbb{P} = 1 - e^{-\frac{4}{3}\pi\rho r^3}, \tag{2.29}$$

where ρ is the spin density. The nearest neighbor probability distribution and its derivative, termed the probability density, are depicted in Fig. 2.13 for both our sample and a commercial diamond sample from Qnami[157] whose properties will be further examined in Sec. 3.2. Due to the random spreading, the average interspin distance is not equal to the maximum interstice, which is only possible for an equidistant distribution. The r for which the probability density is maximal corresponds to the average spin-spin distance yielding $\backsim$13 nm for our sample and $\backsim$57 nm for Qnami diamond.

2.5.2 Thickness condition

The resonant slice thickness condition appropriate for a single-spin measurement is semi arbitrary, because its only limitation is the ill-defined prerequisite that the resonant volume should, with high probability, contain at most an individual electron.

Here we choose the following: the thickness should be such that a slice is populated at most by a single spin with 90% certainty.

Provided by the intersection of P = 0.1 with the straight 0.4 ppm line in Fig. 2.13a, this would translate to a thickness d = 7 nm under mitigated circumstances, i.e. the sphere-like volume of the resonance slice and spin diffusion were ignored. The up till now neglected transfer of magnetization subverts a single-spin measurement considerably as it leads to an enlargement of the resonant slice by 3 nm in all directions.
Further, Fig. 2.14a suggests the resonant volume cannot be omitted, therefore we present a more elaborated analysis of the resonant volume to establish a meaningful answer regarding the set requirement. Starting off with the geometry: the B_0 gradient is not constant throughout the resonant slice, however it was shown[158] that the spreading is only 1.5% for a homogeneously magnetized spherical magnet. Additionally, the rf field strength contains also a spatial dependency, although, at already a few μm from the rf line $\frac{dB_1}{dx} \ll \frac{dB_0}{dx}$ and the gradient rapidly reduces to an insignificant value on the scale of a constant B_0 slice (Sec. 2.2.3.2) so it can be considered constant. The figure of merit is that the resonant volume can be represented by a parabola-shaped half-sphere (Fig. 2.7).

An analogous prerequisite to the aforementioned one, massaged to be directly applicable to Fig. 2.14, is that the thickness should be such that the expected number of spins accommoda-

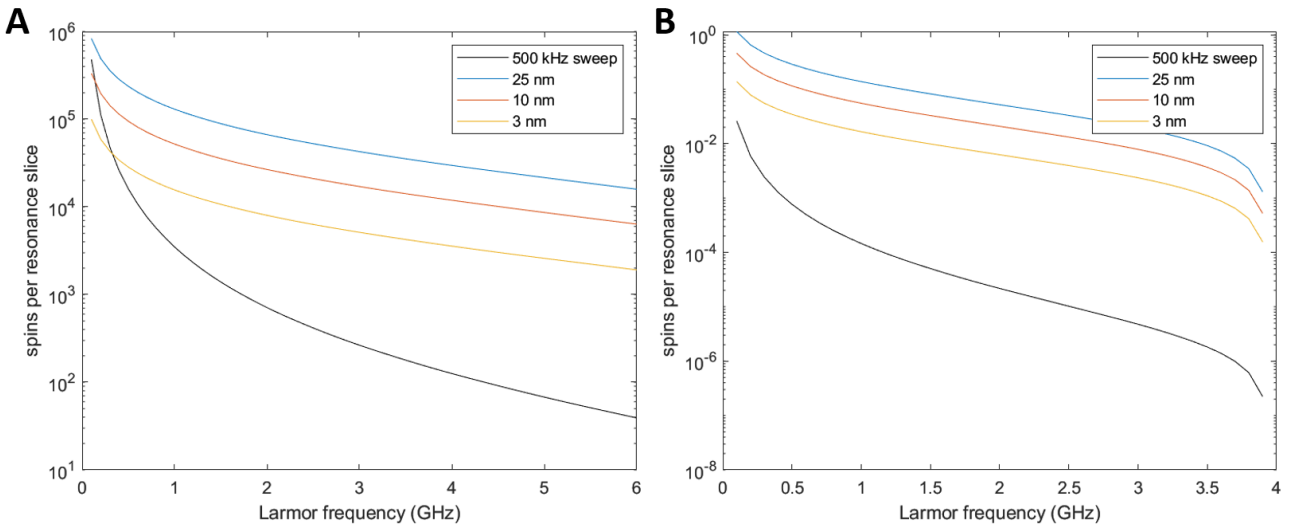

Figure 2.14: *Calculation of the dependency on the Larmor frequency of the expected number of spins within a resonant slice of constant thickness and an ARP pulse with a 500 kHz frequency sweep range. (a) The parameters correspond with our typical experimental values, i.e. tip-sample separation = 25 nm, Q = 2500[19] and for the others see Tab. 2.1. (b) Parameters from the single-spin experiment were used:[8] ω_0 = 5500 Hz, k_0 = 110 μN/m, R_0 = 75 nm, RMT = 1 T, tip-sample distance = 25 nm, Q = 2500, ρ = 0.4 ppb. Rugar and cowokers performed their measurement at h = 125 nm so the number of spins per slice is slightly higher than in the actual experiment. Furthermore, their quality factor is unknown so we assumed one of similar value and we approximated their rectangular SmCo tip as spherical.*

ted in a slice is 0.1. From Fig. 2.14a it is clear that higher Larmor frequencies yield a lower amount of spins per slice, ARP pulses are preferred over a slice of constant thickness and the spin concentration in our sample is several orders of magnitude too dense to enable single-spin measurements.
Considering a previously achieved resolution of 4 nm in our group,[25] single-spin detection is well within reach if the following improvements are implemented: switching to nanometer-sized tip magnet and probing a specimen with a spin density at least hundred times lower than 0.4 ppm. These two substitutes of the current micrometer-sized magnet and the 0.4 ppm sample would enable single-spin detection with a high degree of certitude under reservation that the requirements discussed in the other sections of this chapter are met. The improvements will be in detail discussed in chapter 3, including nanocantilevers and an external field.

In this thesis, no attempt to verify the proposed condition is presented, however, previous published literature contains multiple indications for the correctness of our proposition. To bring the detection of a single and isolated spin within reach, the requirement of an on average sub-one spin population in the resonant slice was earlier suggested by Mamin and coworkers in 2003.[27]
More important is the experimental confirmation in the following year. The reported 25 nm spatial resolution by Rugar *et al.*[8] at ω_{Larmor} = 2.96 GHz for a thousandfold more diluted sample was achieved with iOSCAR. Visible in Fig. 2.14b, at 3 GHz the expected number of spins in a slice of 25 nm thickness is ~0.03. This translates to a 97% single-spin certitude within the resonant slice, thereby supporting the legitimacy and feasibility of our chosen requirement.

2.6 Apparatus stability

Many scanning probe techniques such as scanning tunneling microscopy (STM),[159–161] atomic force microscopy (AFM)[162,163] and MRFM are highly sensitive to environmental vibrations. For our setup it has been demonstrated that the vibration isolation yields excellent thermal conduction and greatly attenuates vibrations nearby the system's resonance frequency.[164] Nonetheless, we discuss the necessary requirements for a single-spin measurement, because even more so than usual, single-spin sensitivity requires a high mechanical stability to minimize internal drift and exceptional isolation from external vibrations to maintain fluctuations in the tip-sample distance well below the resonant slice thickness. At the same time, the size of fluctuations in the tip-sample spacing is a measure for the system's maximal spatial sensitivity.

A cantilever with a low spring constant and a high quality factor is desired to detect extremely small forces. However, this simultaneously introduces a high sensitivity to environmental vibrations and therefore conflicts with requirements for minimal tip-sample fluctuations. Mechanical stability and attenuation of environmental vibrations is generally achieved by isolation of the cryostat on a heavy stage and segregation of cooling pumps from the cryostat. In our case, the main cooling equipment, the pulsetube, is clamped to the cryostat and emits vibrations of 1.4 Hz and its harmonics into the setup. This requires the implementation of isolation within the cryostat, which is for various reasons significantly more complicated[161,164,165] than for liquid helium-cooled cryostats.
The universal vibration isolation dilemma can be formulated as follows: for a given source and receiver, design an isolation with a transmissibility that diminishes environmental vi-

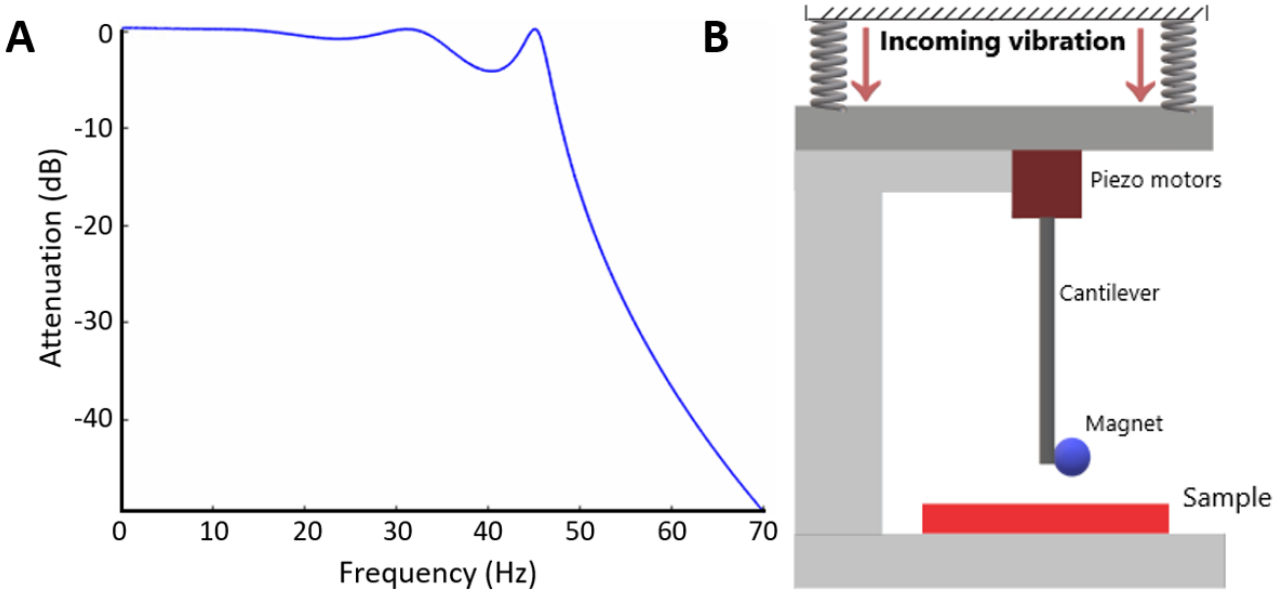

Figure 2.15: *(a) The high attenuation of the four-stage mass-spring system containing the specimen at the bottom shields the experiment from external vibrations interfering with cantilever eigenfrequencies. The mass-spring system acts as a low-pass filter having a tipping frequency of 45 Hz. The main source of continuous external excitations, however, can still pass unobstructed, causing permanent oscillations of the resonant slice. (b) An overview of all relevant elements in the tip-sample complex located on the bottom of the four-stage mass-spring system.*

brations to a tolerable level. As aforementioned, an acceptable vibrational peak-peak amplitude is negligible compared to the slice thickness. The efficiency of an isolator, loosely termed the transmissibility or transfer function, can be defined as the reciprocal of the ratio of force or velocity amplitudes at the outgoing to the ingoing side.[166]

Here, we restrict the discussion to vertical vibrations leaving out rotational and horizontal motions, because the tip-sample distance is most sensitive to vertical displacements, which we assume to originate from harmonic vibrations. Nevertheless, the existing vibration isolation affects horizontal movements identically.
The exact properties of each element in the cryostat are unknown, as such we based our calculation of the transfer function of the total system on just the four-stage mass-spring structure and note that this is an upper bound. Furthermore, we neglected the cantilever mass, because it is negligible compared to the structure's mass it is mounted to. The piezo motors are considered incompressible and therefore the cantilever is effectively only influenced by displacements of the springs connecting the sample-cantilever stage to the upper stage, condoning the treatment of solely the tip-sample system as depicted in Fig. 2.15b.
For an external sinusoidally driven and strongly damped system, as in our case, the transient state, associated with free movement at the natural frequency, quickly extinguishes. The equation of motion of the sample relative to the cantilever is therefore solely described by the steady-state, which reads

$$x_{s-t}(t) = \frac{F_0}{m\sqrt{(\omega_0^2 - \omega^2)^2 + 4\gamma^2\omega^2}} cos(\omega t - \phi), \tag{2.30}$$

with F_0 an external force, m the mass of the sample stage, ω_0 the system's natural frequency, ω the driven frequency, ϕ a measure of the system response defined as the phase difference

Table 2.3: *Overview of parameters used to calculate tip-sample vibrations*

Parameter	Variable	Value
Spring constant stage	k_{stage}	$5{\cdot}10^4$ N/m
Spring constant piezo	k_{piezo}	~10^8 N/m
Wave impedance	c	314 kg/s
Frequency of incoming waves	ω	n·1.4 Hz
Mass sample holder	m	~2 kg

k_{stage} belongs to the springs that connect the sample holder with the stage above it. To emphasize the equally disturbing influence of higher harmonic modes a factor n was added to 1.4 Hz, with n a natural number larger than 1. The cantilever parameters used to calculate x_{s-t} (Eq. 2.30) are as stated in Tab. 2.1.

between the driven force and the deviation from equilibrium and $\gamma = \frac{c}{2m}$ with c the wave impedance. From Eq. 2.30 it is clear that a high natural resonance frequency is beneficial for curtailing the amplitude of $x_{s-t}(t)$. In our case the difference between ω_0 and ω results in almost a factor 10^7 attenuation.
In equilibrium practically no corrugations in the cantilever occur, whereas, during either spin or feedback induced agitation the cantilever is highly receptive to external vibrations. This means that deviations with respect to a complete perpendicular suspension of the cantilever on the piezo motors have to be minimized.

The pulse tube resonates at multiples of 1.4 Hz, i.e. at the ground frequency and at higher harmonic modes, with a speed of $\frac{10^{-5}m/s}{\sqrt{Hz}}$. Using the values in Tab. 2.3 to calculate x_{s-t} and multiplying the amplitude with the transfer function showcased in Fig. 2.15a yields a maximal amplitude of roughly 1 pm in the frequency range of the pulse tube. Hence, we conclude that the vibration isolation is of sufficient quality to enable single-spin detection.

A remark on internal drifts

Internal stability and thus a low drift speed is of importance for the sake of averaging, since the typical SNR for single-spin measurements lies far below unity[8]. The easiest and fastest way to get a grasp of internal drift speeds is to measure the duration in which the signal strength of a single spin, electron or nucleus, decays to a level indistinguishable from noise. Although no experiments with long averaging times were undertaken in our group, it was measured that the cantilever experiences a drift of 1 Å/hour when the piezo knobs are thermalized. Furthermore, it is plausible that other drift speeds are also very low considering the absence of levitating components, the high stiffness of materials and negligible external and internal vibrations.

CHAPTER 3

SETUP IMPROVEMENTS

Prologue to the Chapter

As described in chapter 2, to enable unambiguous single electron spin detection several technical improvements of our current setup are required. Of particular importance is a diamond sample with a low density of spin impurities and with geometrical properties suitable for our sample holder and the employment of a nanometer-scale magnetic tip for improved sensitivity.
To broaden the applicability of this chapter we include the discussion about the influence of high-compliance nanometer-scale cantilevers and an external static magnetic field on the feasibility of a single-spin experiment. Furthermore, these four setup enhancements are also of relevance to achieve spin-cantilever superposition and in the improvement of quantum information processes using NV centers (Sec. 1.4).

In this chapter we in particular expound on nanomagnets. The discussion of the improvements is presented in the following order:

1) *External magnetic field*
2) *Sample with a low density of diamond impurities*
3) *Nanomagnets*
4) *Nanometer-scale cantilevers*
5) *Proposed improvements*

Measurements with a nanocantilever have already been done in our group. The specific type as well as other sort cantilevers will be discussed in Sec. 3.4.
Furthermore, the creation of an external field up to 500 mT is currently under development in our group. The technical details and the assembly process of the materials used to generate a static external B_0 field has been the subject of previous theses and publications[167–169] and will be further discussed in future theses.

3.1 A static external magnetic field

The ability to switch on an external field allows a greater selection of measurement protocols (for example CERMIT, Sec. 2.2.2.2), increases the polarization and, we believe, reduces the magnetic dissipation.[108,164]

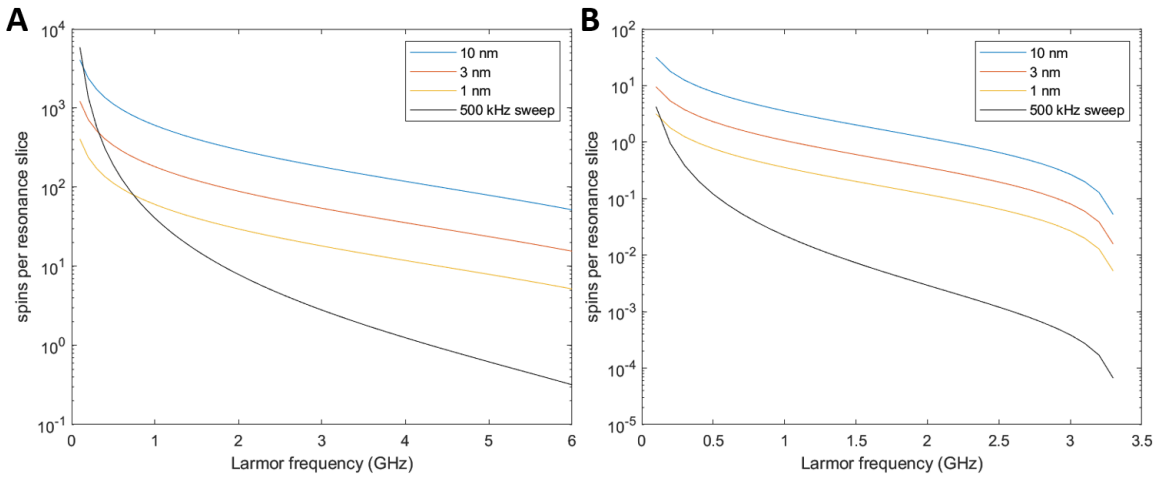

Figure 3.1: *Numerical simulation of the amount of spins per resonant slice of constant thickness and one created by a 500 kHz sweep as function of the Larmor frequency. a) Parameters: NdFeB magnet with radius = 1.75 µm and tip-sample separation = 200 nm. b) Parameters: cobalt magnet (Tab. 3.1) with radius = 200 nm and tip-sample separation = 50 nm.*

SQUID-based detection enables MRFM measurements at millikelvin temperatures, but the high sensitivity to magnetic flux complicates the use of an external field throughout the cryostat (Sec. 1.3). In order to distinguish the cantilever signal from noise, the external field can only be generated inside the superconducting shielding and its noise levels have to be minimized to non-disturbing values in the proximity of the pickup loop. A recently developed design, consisting of a local persistent current flowing through a loop, which can be short-circuited by Niobium, shows promising results. Up till now, a field of roughly 100 mT was created, however, the field strength could possibly reach ~500 mT,[1] which is a fundamental limit given by the upper critical magnetic field (H_{c2}) of Niobium. Niobium belongs to the class of type-II superconductors that all feature a superconducting regime bounded by the thermodynamic critical field (H_{c1}) and a mixture state that consists of superconducting current vortices with a normal core.
It is unclear at present whether our approach allows creating magnetic fields larger than H_{c1}. In our discussions of nanomagnets (Sec. 3.3) that include an external field we assume the maximal field strength of 500 mT.

In the presence of an external field $B_0 = B_{magnet} + B_{ext}$ as is the situation in every other MRFM setup in the world. Consequently, the spin-cantilever dynamics are now in general as described in Chapter 8 of Ref. 4. Furthermore, the description of the full evolution of the Schrödinger cat state,[171] its decoherence[126] and the thermal diffusion of the cantilever tip[4] likewise changes. It should be noted that, in contrast to our situation, in other apparatuses the following inequality holds for every point in space: $B_{ext} \gg B_{magnet}$. The inability to make this simplification results in the fact that the field direction varies a lot in space and this causes our results to sometimes be different from phenomena examined in the previous mentioned references.

3.2 A low impurity concentration

In this section we calculate the required resonant slice thickness for a single-spin measurement with a high-purity diamond sample with implanted NV centers. This specimen has

[1] The exact value of the critical field depends on the temperature, niobium purity and crystal orientation.[170]

a spin impurity density of 5 ppb and is commercially available from Qnami[157] or can be obtained from the group of van der Sar in Delft. The probability and the probability density functions of the nearest neighbor distance for this sample have already been displayed in Fig. 2.13. Here, we will only describe the feasibility of single-spin detection (defined in Sec. 2.5.2) with this spin density and leave out a discussion regarding the specific impurities that are present in the diamond.
The slice thickness is computed (Fig. 3.1) both for our current magnet and for the nanomagnet in the absence of an external field as described in Sec. 3.3. The corresponding tip-sample distances are 200 nm (in agreement with the experimental situation in chapter 2) and 50 nm, respectively.

With the Qnami sample, a single-spin measurement is still not achievable if a micromagnet is employed. However, single-spin detection comes within reach if a nanomagnet is used, even after accounting for an enlargement of the resonant slice by the diffusion length (Tab. 3.2).
To facilitate single-spin detection with a micrometer-sized magnet, a lower impurity-density sample than Qnami's specimen might be more propitious. It is not inconceivable that a spin density as low (~0.4 ppb) as used for the single-spin detection in Ref. 8 is required. Finding a spin signal would become harder, but the chance to unambiguously detect an individual spin would increase.

3.3 High-gradient nanomagnets

Many applications of MRFM require an exquisite sensitivity and a high spatial resolution. As we have shown in Sec. 2.2.1, the SNR scales with the magnetic field gradient. Nanomagnets allow a smaller spacing between the magnet's center and sample surface, as such the field gradient in the proximity of a nanomagnet is higher than for our currently employed micrometer-sized magnet. To maximize both the resolution and the sensitivity, the magnet's size has to be minimized to improve the resolution, while maintaining a large magnetic moment to preserve a strong signal. Moreover, the structure of the cantilever-tip system[172] and the magnet's purity[173] play an important role in the mitigation of surface noise and the size of the saturation magnetization, respectively. In Ref. 172, Hickman *et al.* found that a tip attached to a NW hanging over the leading edge of a micrometer-sized cantilever reduces surface noise by increasing the distance between the bulk cantilever and the sample, while allowing the magnet to be within several nanometers of the surface.
Of further relevance is the shape and material of the magnet, namely, a homogeneously magnetized and a spherically shaped magnet permits the use of the magnetic dipole field approximation, which eases analytical predictions. A spherical geometry together with a lack of magnetocrystalline anisotropy[174] of certain ferromagnetic materials diminishes the effect of an external field on the cantilever's resonance frequency.[175]
This section is structured as follows: the first part is devoted to the form of magnetism of nanometer-scale magnets. The central tenet from this paragraph is taken into account when discussing the double-magnet cantilever system introduced in Ref. 9. As a feasibility test of this design we numerically simulated the polarization and field deformations in the absence and presence of an external static magnetic field.
Furthermore, the value of the flip-flop time, diffusion length and spin force are calculated in the high-gradient field of a nanomagnet. At last we describe the impact of a nanomagnet on the SNR and calculate the optimal cantilever amplitude with an attached nanomagnet in a force-gradient based protocol.

3.3.1 Superparamagnetic state

Depending on the material, nanoparticles become superparamagnetic[176–178] below a critical size. In general, magnets are composed of an assembly of elementary magnetic moments (electrons) that all have an independent orientation to minimize the system's potential energy such that the total magnetic moment is zero. Ferromagnets, however, are subdivided in domains in which the magnetic moments are aligned. The domains behave as the electrons in regular magnets, nonetheless, the system's left over magnetization is non-zero due to a non vanishing polarization. At sufficiently small length scales it is energetically favorable for a ferromagnetic particle to remove the domain barriers, known as Bloch walls in literature, and evolve into a single domain, i.e., a transition to a superparamagnetic state occurs.[179,180]
As explained in Sec. 2.1.3, random flip-flops of the magnetization are an intrinsic property of electrons. The magnetization M of a nanomagnet exponentially decays toward equilibrium according to the Néel relaxation time, which is roughly the time between two jumps (M to -M).[181] In the absence of an external field the time-averaged magnetization is zero. The statistic behaviour of the magnetization emerges from thermal fluctuations and can be thought of as Brownian-like rotations of the orientation of magnetic moments.
In order to capture the full potential of a superparamagnetic nanomagnet's high-gradient field, an external field strong enough to orient the magnet in a fixed direction is required. Given that our current setup does not involve an external field, the reason laid out above is the main impetus to employ a probe whose dimensions do not fall into the superparamagnetic regime.

3.3.2 Double-magnet cantilever

A magnet-on-tip geometry calls for a fabrication process in which the magnet is directly grown on or adhered to the cantilever apex. In this thesis we will not expatiate on different techniques, but only note that high-gradient magnets suitable for the magnet-on-tip approach have been produced by the following methods: focused electron beam induced deposition (FEBID),[173] electron beam lithography,[172] focused ion beam (FIB) milling[182] and e-beam lithography.[67] Our unique apparatus might dictate specific adjustments to certain fabrication processes, but we will not expand on this here and leave the subject to future projects devoted to the development of nanomagnets.
The difference between our setup and the situation in all other MRFM groups is the absence of a large external static field and the use of a SQUID-based detection scheme instead of a beam deflection readout system. As such, in our case, detection requires a careful positioning of the cantilever in the vicinity of the pickup loop. This is further complicated, because the B_0 field stemming from a nanomagnet is very small and therefore arduous to detect.

To bypass these challenges de Wit *et al.* proposed a double-magnet cantilever with a small magnet attached to the tip for a high field gradient and a large one affixed slightly above for strong coupling with the SQUID (Fig. 3.2). In chapter 8[9] of de Wit's dissertation the situation of two micrometer-sized magnets, having 0.95 μm and 1.82 μm radii, is both numerically and experimentally analyzed.
Here we extend the analysis by considering a nanomagnet as tip-magnet combined with a micromagnet as coupling magnet and numerically compute the polarization and deformations of the magnetic field around the nanomagnet.
An overview of all relevant distances in the geometry of the double-magnet cantilevers and the remnant magnetization of the magnets examined in this section is accumulated in

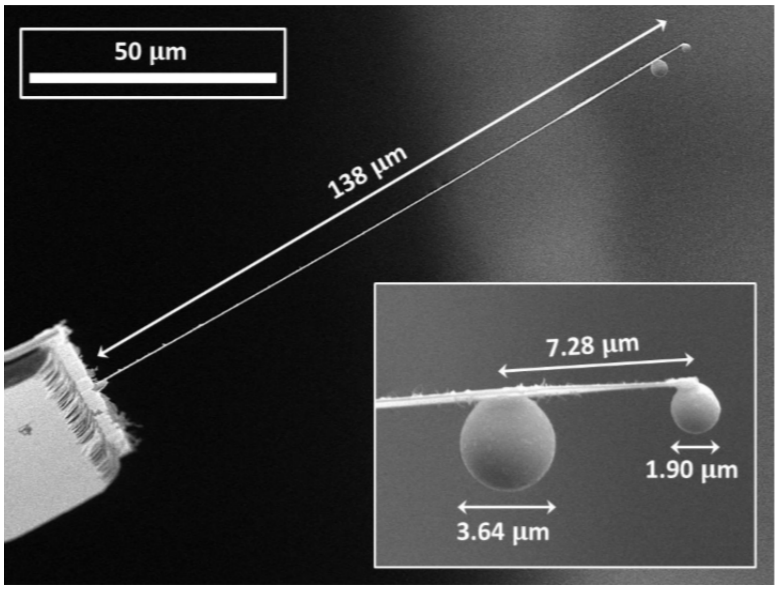

Figure 3.2: *Image made with a scanning electron microscope of the double-magnet (both NdFeB) cantilever system as investigated by de Wit. A similar situation is examined here with the dimensions of the magnets in our calculations as stated in the text. Figure reprinted from de Wit.*[9]

Tab. 3.1. A motivation for the chosen values is presented further on, as well as a derivation of certain values.

Instead of the currently employed NdFeB magnets, our study is based on uniformly magnetized spherical cobalt nanoparticles, which have a single domain diameter D_c of 45 nm.[183] Interestingly, the saturation magnetization M_s of cobalt nanoparticles with diameter D can be divided in three regimes. In magnets with 32 $nm < D < D_c$ a stable vortex is present, however the total magnetization rapidly drops to merely ~$0.6M_s$. In the range 24 $nm < D <$ 32 nm both a vortex and a quasi-uniform state exist and for $D <$ 24 nm only the quasi-

Table 3.1: *Summary of the geometry and magnetization of the investigated double-magnet cantilevers in the presence and absence of a vertical external magnetic field*

Parameter	No external field	with an external field
Magnetization cobalt tip magnet	0.7 T	1 T
Radius cobalt tip magnet	200 nm	100 nm
Magnetization NdFeB coupling magnet	1.3 T	1.3 T
Radius NdFeB coupling magnet	1.75 μm	1.75 μm
h-distance	2 μm	7 μm
tip-sample distance	50 nm	50 nm
intermagnet distance	0.58 μm	5.4 μm
coupling magnet-sample distance	2.57 μm	7.24 μm

The geometry of the double-magnet cantilever system is fully characterised by the the sticking points of the magnets to the cantilever (labeled h-distance) and the tip-sample distance. The separation between the coupling magnet and the sample is defined as the distance between the coupling magnet's center and the sample directly below the nanomagnet. Note that the centers from the magnets are not at the same distance from the cantilever.

uniform state remains. This state retains about $0.95M_s$, therefore $D \simeq 24$ nm can be considered the effective single domain diameter.[180,183]
The dependency of the total magnetization on the cobalt content in a nanoparticle is of greater relevance, because the influence is already significant at length scales $D < 400$ nm. In practice, every fabrication process induces damage to the particle and the exposure to air leaves a magnetically dead oxidation layer behind. In Ref. 173, Sangiao *et al.* found that for cobalt nanomagnets fabricated with FEBID, the optimal ratio for MRFM between the total magnetization and the size is a particle with D = 200 nm. At this size, the magnetization is still roughly 70% of the bulk saturation magnetization, which is ~1.8 T for cobalt.

The result, pertinent to the previous paragraph, is a direct incentive for us to investigate cobalt nanomagnets with a radius of 200 nm in the absence of an external field and with a radius of 100 nm if an external field is present. As coupling magnet we used a NdFeB magnet with a radius of 1.75 μm.
h = 2 μm and h = 7 μm are the intermagnet distances based on the magnet's sticking point to the cantilever that we use for studying the absence and presence of a static external field, respectively. The combination of a permanent and relatively high saturation magnetization of NdFeB together with an incredibly small single domain diameter and extremely high saturation magnetization of cobalt makes these materials befitting for MRFM applications with a double-magnet cantilever.

3.3.3 Field dynamics and polarization

We will examine the double-magnet system first without an external field as is the status of our current setup and thereafter with an external field, which is under development at the time of writing. In our analysis we assumed a homogeneously magnetized nanomagnet. As shown later on, the applicability of a double-magnet cantilever is limited without an external field, even in the idealized situation of a homogeneously magnetized tip magnet. The development of an external field is still in the early stages of testing, therefore we cannot yet determine the position-dependent strength of the field and the gradient-field in a MRFM experiment. Other groups that have a setup with a large external magnetic field experience a fixed magnetization direction of the spins and the magnet. Moreover, the dissipation reduces too, but this topic is left out of our analysis.

3.3.3.1 No external field

In the double-magnet geometry, which we have chosen for this simulation, the intermagnet spacing is ~0.58 μm. At this distance, the induced magnetic field strength stemming from the coupling magnet at the position of the nanomagnet is approximately 180 mT (Fig. 3.3c). Using Fig. 3.3a, this corresponds to a normalized magnetization of $0.4M_s$, which translates to ~0.7 T. Displayed in Fig. 3.3b-f, this value was used in all simulations concerning the field stemming from the cobalt nanomagnet, while a remnant magnetization of 1.3 T is used for the NdFeB coupling magnet.

Magnetic field deformation

Field deformations complicate the data analysis, because the dipole approximation does no longer hold. The field's isolines of the double-magnet cantilever have to resemble the field of a point source at the spin's position to consider it as a dipole field. Although imaging would still be possible by using deconvolution techniques, it would be more complicated and time-consuming.

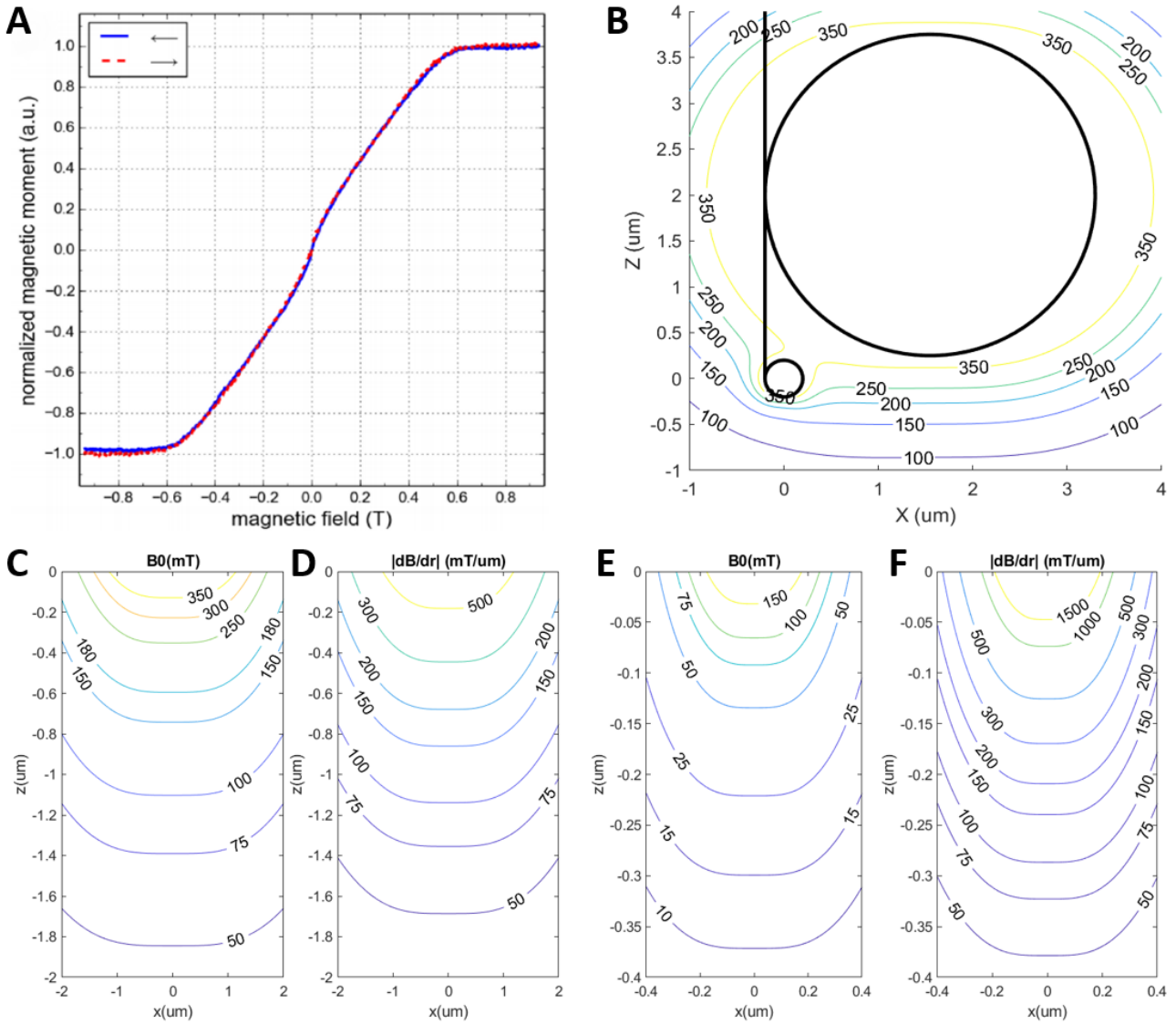

Figure 3.3: *Figure of the magnetic hysteresis of cobalt nanoparticles performed at room temperature, reprinted from Sangiao and coworkers[173] (a) and plots of the numerical simulations of the magnetic field of the double-magnet cantilever in the absence of an external magnetic field (b-f). The magnetization direction of the magnets is in the positive x direction. Geometry of the cantilever system used in the simulations is as described in the text. b) Plot of the combined field of the magnets. Plots of the field and the gradient field in the x-z plane of the coupling magnet (c,d) and the tip magnet (e,f), respectively. Coordinate (0,0) is the magnet's surface in figures (c-f) and the nanomagnet's center in figure (b).*

When the magnetic field or the gradient field of one magnet dominates at a certain tip-sample separation, the total field can be deemed to originate from a point source, i.e. a single magnet. In the vicinity of the nanomagnet, that is, within a tip-sample spacing of roughly 60 nm, the nanomagnet's gradient field exceeds the coupling magnet's gradient field by at least an order of magnitude - determined by comparison of the gradient fields in Fig. 3.3d,f at the respective spin-magnet distances. On the other hand, the B_0 field of the magnets is of comparable strength around the nanomagnet.

Possible solutions to alleviate the problem of proportionate field values are: i) a decreased size of the nanomagnet or ii) an increased distance between the two magnets, however, both come at the cost of a reduced magnetization of the nanomagnet. Further research, either

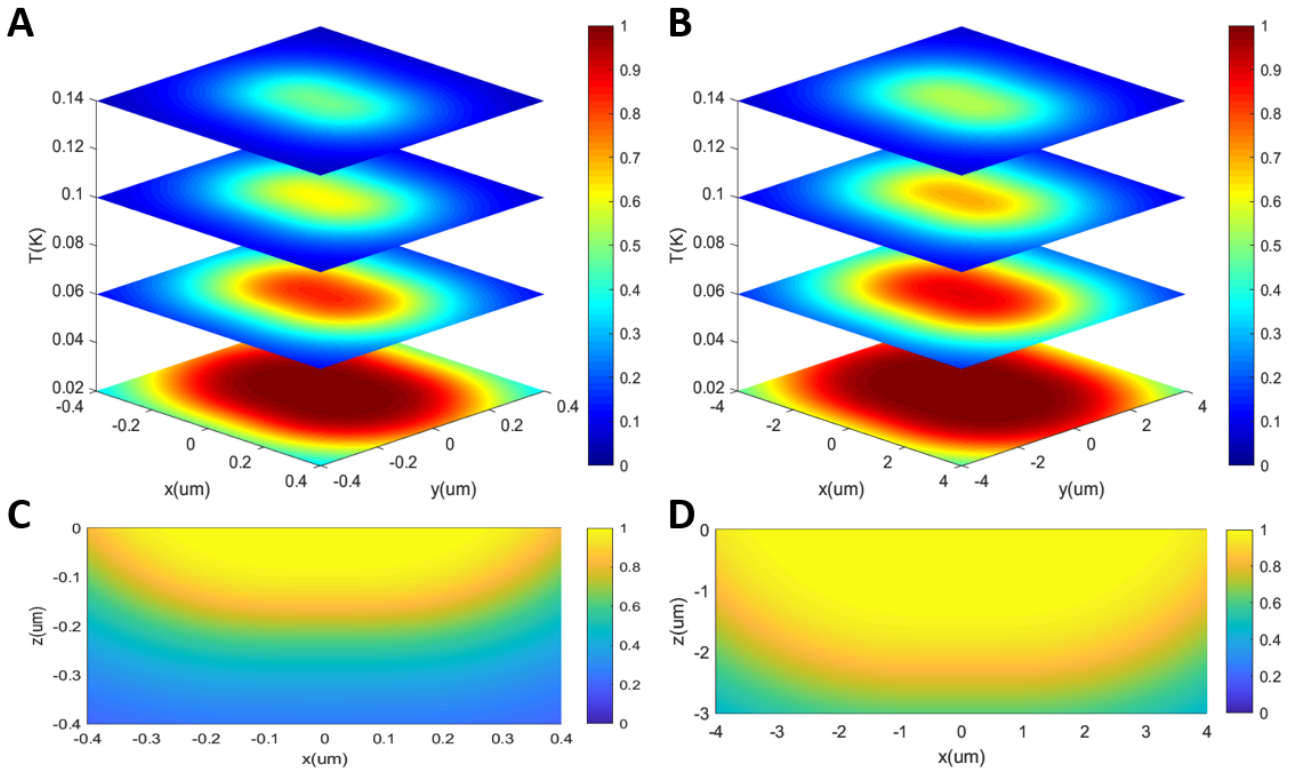

Figure 3.4: *Relative polarization as a result of the nanomagnet's magnetic field computed at a tip-sample distance of 50 nm for different temperatures in the x-y plane (a) and at 20 mK in the x-z plane (c). b,d) Relative sample surface and bulk polarization due to the micrometer-sized coupling magnet calculated at the same temperatures as (a,c). Coordinate (0,0) corresponds to the point directly below the center of the magnet in all figures.*

experimentally, numerically or both, is required to determine the optimal magnet size and h-distance. The optimal situation greatly depends on the realization of an external field.

Polarization

The degree of polarization of spins within 100 nm of the nanomagnet is nearly 0.5 (Eq. 1.9 and Fig. 3.4) as a consequence of both the magnetic field emanating from the tip magnet and the coupling magnet. The polarization is highly susceptible to changes in the magnetization so for any adjustments to the size of the magnets or the intermagnet distance the polarization has to be re-evaluated.

3.3.3.2 With an applied static external field

In our analysis we assume a sufficiently small gradient of the external field such that it is negligible compared to the tip magnet's gradient field. As stated in Sec. 3.1, the expected strength of the external field is roughly 500 mT near the coil. To compensate for the tip-coil distance we presumed a field strength of 400 mT at the location of the tip magnet, which results in a magnetization of 1 T[2] of the nanomagnet. In the h = 7 μm geometry, the inter-magnet distance is roughly 5.4 μm and the separation between the coupling magnet and the sample directly below the nanomagnet is about 7.3 μm.

The magnetic field and the gradient field of both magnets have been numerically calculated

[2]The value of M_s of a cobalt nanoparticle with a radius of 100 nm is only ~1.25 T.[173] Using Fig. 3.3a, a field strength of 400 mT translates to a magnetization of 1 T.

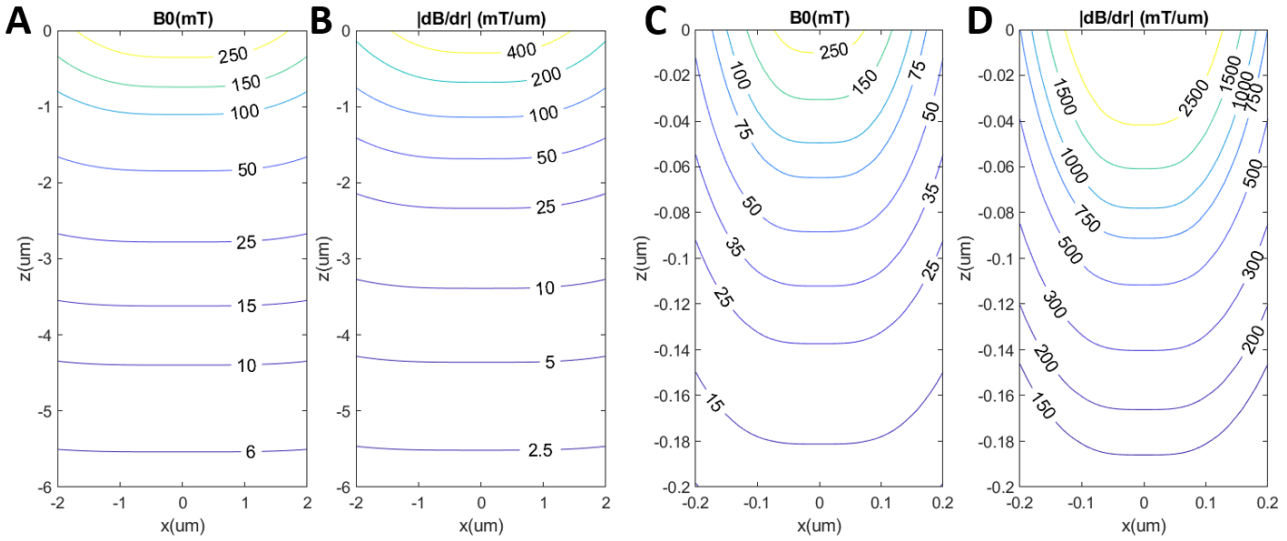

Figure 3.5: *Numerical simulations of the magnetic field and its gradient field of the coupling magnet (a,b) and the tip magnet (c,d). Magnetization and geometry is as described in the text and coordinate (0,0) is the magnet's surface.*

and displayed in Fig. 3.5. In this magnet configuration the field and the gradient field values in the neighborhood of the nanomagnet are both dictated by the tip magnet. Due to a stronger magnetic field at the position of the sample, the degree of polarization is expected to be even higher than in the absence of an external field, however, the lack of experimental data about the external field at the time of writing prevents us from quantitatively elaborating on this.

3.3.4 Dissipation and diffusion in the presence of a nanomagnet

Here we present the calculations regarding the diffusion length, flip-flop time and the single spin force in our current diamond sample and the Qnami sample characterized in Sec. 3.2 for a typical tip-sample spacing of 50 nm. The calculations regarding L_D and T_{ff} were performed analogous to the method described in Sec. 2.1.3 and F_s was computed as stated in Sec. 2.4.2. The gradient is 1.5 MT/m at 50 nm from the nanomagnet in the absence of an external field. We note that this is a lower bound, because in case an external field is applied, the tip magnet's gradient field reaches even larger values at 50 nm.

Table 3.2: *A succinct overview of the influence of a nanomagnet*

Variable	Current sample	Qnami sample
ρ	0.4 ppm	5 ppb
$r_{interspin}$	24 nm	104 nm
L_D	<1 nm	<0.2 nm
T_{ff}	>0.55 s	>220 s
F_s	$1.4{\cdot}10^{-17}$ N	$1.4{\cdot}10^{-17}$ N

The diffusion length, the flip-flop time and the spin force were calculated for a gradient of 1.5 MT/m according to the method described in Sec. 2.1.3 using Eq. 2.3, Eq. 2.4 and Fig. 2.3b and Sec. 2.4.2. For a comparison of the values of the variables computed here with the values in our current setup see Tab. 2.1 and Tab. 2.2.

Furthermore, the T_2 time is not expected to differ much in the vicinity of the sample surface compared to the value inherent to the single micrometer-sized magnet used in chapter 2. It is limited by the ^{13}C nuclear fluctuation time of 250 μs (Sec. 2.1.2).
It should be noted that the diffusion length and the flip-flop time stated here are an upper bound and a lower bound, respectively. The analysis is restricted by the suppression factor (Fig. 2.3b) as function of ΔB, the field difference between adjacent spins, which depends on the field gradient and the dissipation between spins. It only goes up to ΔB = 8 mT, while the field difference is 18 mT in our specimen and 78 mT in the Qnami sample. The suppression factor at ΔB = 8 mT is used in the calculations, however we conjecture that the suppression factor is considerably larger at ΔB = 18 mT and possibly several orders of magnitude larger at ΔB = 78 mT.
The results are accumulated in Tab. 3.2. As anticipated, the suppression of dissipation and diffusion is much stronger than the experienced suppression as a result of the currently employed micrometer-sized magnet. Furthermore, due to the higher gradient field from the nanomagnet, the larger spin force generates a stronger signal and thus increases the SNR.

3.3.5 The effect of a nanomagnet on measurement protocols

In Sec. 2.2.1 we showed that SNR_{FG} is more beneficial if the ratio of the tip-spin distance (R) to the driving amplitude (A) is smaller than 1. In that section we already expounded on the reasons why a force-gradient approach is more auspicious even if $SNR_F > SNR_{FG}$. Here, we calculate the optimal A in a force-gradient based experiment and demonstrate that R/A is smaller than 1 for, in our case, typical values of R and A. This result is the main motivation to use a force-gradient protocol. Since we already expanded on R previously this section, only the main result will be re-stated, namely, a smaller magnet allows a closer approach to the sample surface.

In Ref. 5, an expression for the SNR of the cantilever's frequency shift during one period, induced by a single spin as function of the cantilever amplitude and the tip-sample separation is derived. It was found by numerical integration that the optimal force-gradient zero-to-peak cantilever amplitude is[5,57]

$$A_{0p} \simeq 0.47(r_{tip} + h), \tag{3.1}$$

where h is the height measured from the magnet surface to the spin, or equivalently, the tip-sample spacing and r_{tip} the radius of the tip magnet. At a tip-sample distance of 50 nm, $A_{0p} \simeq 70$ nm for r = 100 nm and $A_{0p} \simeq 120$ nm for r = 200 nm. It is now evident that a force-gradient based method is preferred when operating nanomagnets.

The tipping point between a higher SNR for a force-gradient or a force based protocol is $r_{tip} \simeq 1.12$h, which effectively corresponds to $r_{tip} \simeq 1.12$R. It should be noted that in a specific experimental setup the situation might call for a force based approach, while calculations point to a force-gradient based protocol. The relatively large cantilever amplitudes calculated above could cause local heating and produce a torque on the spins.
In the specific case of spherical magnets (as in our case) the field gradients can be calculated analytically, since it is a dipole field. In other instances, e.g. magnet rods, numerical simulation are required to provide an answer. To keep the calculation simple and short only the scaling behaviour could be considered, but if R/A ~1 no indisputable conclusions can be drawn without knowledge about the pre-factor. Nonetheless, a force-gradient protocol

results in general in higher SNRs when employing nanomagnets. This is supported by the frequent use of a force-gradient based approach in setups that involve a nanomagnet.[8,105,184]

3.4 Nanometer-scale cantilevers

The specific geometry and material of a cantilever play a central role in its ability to transduce forces and in the magnitude of the total dissipation (Sec. 2.2). Using Eq. 2.5 as starting point, a low density material, a reduction of the size and a high aspect ratio are beneficial to minimize the mechanical dissipation. Other advantageous consequences of the tendency to miniaturize cantilevers well into the nanometer regime are an increased sensitivity and abated environmental vibrations. Since the natural resonance frequency increases as the size decreases, the latter mentioned effect follows directly from Eq. 2.30.
The promising range of applications of nanometer-sized cantilevers together with recently developed bottom-up assembly processes that enable atomic-scale precision fabrication and innovative top-down produced designs are the reason for the dominant role of nanometer-scale cantilevers as force sensor in many force microscopy techniques. Cantilevers can be divided into the following groups based on their fabrication process: nanowire (NW) cantilevers or nanocantilevers. The main differences will be explicated below.
An in-depth review of the mechanics and force sensing properties of NW cantilevers is presented by Braakman and coworkers.[185] On the other hand, nanocantilevers are extensively discussed in the book by Schmid *et al.*[186] and in the application-focused review written by Eom and coworkers.[187]
In this section, nanometer-scale cantilevers are briefly reviewed in general, after which the nanocantilever used in our group[3] and the influence of a nanometer-scale cantilever on the feasibility of a single-spin experiment are discussed.

3.4.1 Principles of nanometer-scale cantilevers

Traditionally, MRFM measurements are carried out with top-down produced Si micro- or nanocantilevers.[188–190] These fabrication techniques, such as lithography and chemical etching, are limited in their ability to downsize cantilevers even further than today's size and introduce surface impurities. Nonetheless, the methods are very consistent in mass-producing nearly identical structures at a low cost. Although many researchers have invested significant effort in improving the top-down cantilever designs,[190] the sensitivity has not reached lower values than several hundred zN/$\sqrt{Hz}$.
The optimal achievable sensitivity is related to the experienced dissipation, temperature and bandwidth (Eq. 2.8). Analogous to the case of a rectangular cantilever presented in Sec. 2.2, the mechanical dissipation of a cylindrical cantilever with length $l \gg d$, the diameter, can be derived from the general formula: $\Gamma_m = \frac{\sqrt{km}}{Q}$. From Euler-Bernoulli's beam theory follows $\sqrt{km} \propto d^3/l$[185] and $Q \propto d$[191] so $\Gamma_m \propto d^2/l$. This result is in agreement with the conclusion for rectangular cantilevers, i.e., long and thin cantilevers are best suited for experiments that require very sensitive force transducers.

Bottom-up processes were developed in order to lower the dissipation further, increase the natural resonance frequency and improve the resolution, driven- and self-assembly.[192–194] In these fabrication approaches the NW cantilevers are grown molecule-by-molecule, which results in devices with nearly defect-free surfaces, astonishingly low masses and very small

[3] For clarity, the standard cantilever in our group is the one briefly mentioned in Sec. 2.2, which is a relatively large micrometer-sized cantilever. The double-magnet cantilever in Fig. 3.2 has similar dimensions.

cross-sectional areas. The pinnacles of bottom-up assembled nanomechanical resonators, e.g. nanotubes and NWs, are a record-low recorded sensitivity of 12 zN/$\sqrt{Hz}$ at 1.2 K[195] and a mass resolution of 1.7 yg at cryogenic temperatures.[196] Despite all these successes, top-down fabricated cantilevers have remained the preferred force sensor. It turned out that a magnet integrated on a NW cantilever is rather challenging to implement in a bottom-up fabrication process and the Q-factor lags behind top-down produced cantilevers unless inventive methods are devised to enhance the Q-factor.[197] Another point of concern is the relatively high spring constant compared to regular nanocantilevers.

Although much more research is required in order for bottom-up produced NW cantilevers to become widely applicable, the expected advantageous and the promising results from the first proof-of-concept MRFM measurement[198] with a NW cantilever all indicate that NW cantilevers are likely to become the next generation leading force sensor.
In Ref. 198 the authors reached an unprecedented force noise of roughly 4 aN/$\sqrt{Hz}$ at 4.2 K and a tip-simple spacing of 80 nm. This is of similar value as our best measured force noise measured at a whopping 200 times lower temperature and a 2.5 times larger tip-sample separation, which suggests that they could have reached a force noise of roughly 10 zN/$\sqrt{Hz}$ at 20 mK provided that the NW is thermally limited. Furthermore, with their Si NW they measured a factor 80 less surface dissipation and even a factor 250 less total dissipation at a tip-sample distance of 7 nm compared to Si cantilevers of similar size and Q-factor as ours at a comparable tip-sample spacing.[111] The underlying physical processes are not yet fully understood, however, the observed reduction of surface dissipation was attributed to a small cross-section area that could possibly decrease the tip-sample interaction strength and a resonance frequency in the rf regime (MHz) compared to our audiofrequency (kHz) resonance frequencies. Even though the spring constant (650 μN/m) is roughly 10 times larger than the spring constant of our micrometer-sized Si cantilevers, the resonance frequency still exceeds a million hertz due to the incredibly low mass.
In one of the early articles about MRFM, Sidles and Rugar[39] showed that the SNR of an electrical and a mechanical oscillator, i.e. for inductive detection and force detection, scales as

$$SNR \propto \sqrt{\frac{\omega_0 Q}{k_m}}. \tag{3.2}$$

Here, ω_0 and Q are as previously defined the resonance frequency and Q-factor of the resonator. k_m is the magnetic spring constant, which is related to the mechanical spring constant k_s as:

$$k_m = \frac{k_s}{G^2} \propto G\frac{wt^3}{L^3}, \tag{3.3}$$

where G is the field gradient and w, t and L are the width, thickness and length of the cantilever, respectively. Since a physically smaller oscillator requires less energy to produce a magnetic field this leads to the same conclusion as in the beginning of this section was found, namely, smaller cantilevers are more sensitive.
The quality factor of the NW was measured to be ~$2.5{\cdot}10^4$ at 8 K and a calculation of the field gradient yielded only $1.2{\cdot}10^5$ T/m at a tip-sample spacing of 80 nm. Due to the relatively low Q-factor and field gradient, the SNR of the NW is comparable to our micrometer-sized Si cantilever, however the potential is enormous. First of all, the 10 times larger mechanical

spring constants is more than made up for by a three orders of magnitude higher resonance frequency. Furthermore, the authors stated that in an improved design field gradients over 10^6 T/m could be generated by reducing the rf-wire constrictions to allow current densities in excess of 10^9 A/cm^2. At last, lowering the temperature to millikelvins would result in a Q-factor of similar value as regular Si cantilever counterparts exhibit. In this optimized situation a 100 to 1000 times larger SNR than our present cantilever has could be realized.

To evade the challenging magnet-on-tip approach Nichol *et al.* coated their cantilevers with ^1H-containing material. Spin detection was performed with a home-developed protocol that utilizes a nanometer-scale wire to generate both the B_1 field and a time-varying B_0 magnetic field gradient. Consequently, the resonant condition is fulfilled throughout the sample, which results in a stronger coupling of the cantilever with the spin bath and thus produces more signal. Furthermore, this innovative protocol requires no driven cantilever vibrations or modulation of the electron or nucleus magnetization at the cantilever's natural frequency.

Nanocantilever or NW cantilever?

In conclusion of this subsection, it is apparent that a size-reduction of the cantilever brings about significant improvement of the sensitivity. A nanocantilever appears to be most eligible due to its direct applicability in our current setup. NW cantilevers, however, demand substantial research in unique technical designs and new spin-detection protocols.

3.4.2 The nanocantilever used in the Oosterkamp group

Recently, our group received one of the nanoladder cantilevers designed and fabricated by Héritier and coworkers. The nanocantilever that was tested in our group is the longest of the Si nanoladder cantilever tested and demonstrated in Ref. 190. A schematic picture of this design is displayed in Fig. 3.6. All the properties of this top-down, batch-fabricated cantilever are as stated and described in Ref. 190. The experimental results obtained with MFRM measurements in our group will be presented in future articles and theses. Here, we will briefly touch upon its unique features that form the basis of its exquisite performance.

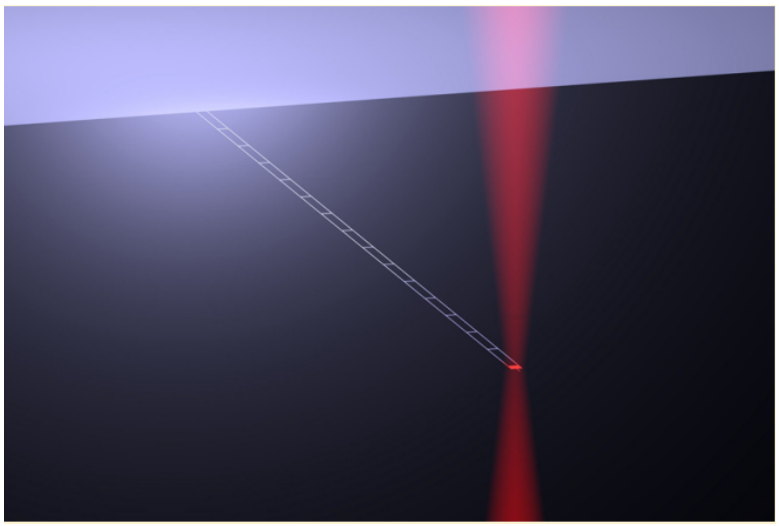

Figure 3.6: *The nanoladder geometry of the cantilever used in our group. Picture reprinted from Héritier et al..*[190]

The characteristic ladder design makes it possible to maintain the rigidity level of a standard rectangular cantilever, while the sensitivity approaches values reported for NW cantilevers. The underlying physical properties that result in this success are an effective mass and spring constant that are one to two orders of magnitude lower than rectangular cantilevers of similar dimensions. The mechanical dissipation was anticipated to likewise decrease about 100 times, however, only a reduction by a factor 15 was measured. An enlarged surface-to-volume ratio and imperfections in the surface of the two parallel wires forming the foundation of the ladder are presumed to be the main culprits. For these reasons the Q-factor is unexpectedly low compared to rectangular cantilevers. Nevertheless, the measured Q_0 is ~45000 at millikelvin temperatures, which does not deviate much from the values our standard Si cantilevers reach[19] (presented in Fig. 1b of the supplementary material).
The major result of the work of Héritier *et al.* is an achieved force sensitivity of 188 zN/$\sqrt{Hz}$ at 110 mK. This is, up till now, the lowest documented sensitivity for top-down fabricated cantilevers. The ability to attach a micro- or nanomagnet to the cantilever tip in combination with the ultra-low sensitivity is an exciting improvement towards applications that require detection of extremely weak magnetic forces.

3.4.3 Impact of a nanocantilever on single-spin detection

Here we discuss a single-spin measurement with the nanoladder cantilever presented in the previous section. In Sec. 2.2 we already demonstrated that the sensitivity of our currently employed cantilever type is sufficient, nonetheless, the superior properties of a nanocantilever ease the unambiguous detection of a single spin. Let us now quantitatively evaluate the impact of the nanoladder cantilever on the SNR of a force-gradient measurement. We will use the formulas from chapter 2.

The nanocantilever exhibits a spring constant of 6.5 μN/m and resonance frequency of ~5500 Hz[190] as opposed to a spring constant of 50 μN/m and resonance frequency of ~3000 Hz of our standard cantilevers (Tab. 2.1). This produces a significantly larger frequency shift regardless of the chosen measurement protocol (Eq. 2.16, 2.17 and 2.19) and, consequently, the spin signal is stronger as well. Another route towards the same outcome is to consider the increased cantilever amplitude (Eq. 2.27).
On the other hand, a lower spring constant also results in larger thermal cantilever fluctuations, however, since the thermal noise only scales as $k^{-1/2}$ and the frequency shift and the cantilever amplitude are both proportionate to k^{-1}, the increase in spin signal will eclipse the enlarged thermal vibrations.
In conclusion, the SNR (Eq. 2.9) scales as $k^{-1}/k^{-1/2} = k^{-1/2}$ for a force-gradient protocol and thus, a nanoladder cantilever increases the SNR.

3.5 Proposed improvements

As a summary of this chapter we present the proposed improvements in bullet form and distinguish between a successful realization of an external magnetic field (0.5 T) and no external field.

- *Low impurity sample*. At least a specimen with a spin density $\lesssim$ 5 ppb is required for feasible single-spin detection.
- *Nanomagnets*. In the double-magnet cantilever geometry: cobalt tip magnets with radius 200 nm in the absence of an external field and radius 100 nm if an external field

is present. As coupling magnet NdFeB with a radius on the order of several micron is preferred.

- *Nanocantilever*. Any nanocantilever, for example the nanoladder design discussed in Sec. 3.4.2 that increases the sensitivity and has a larger force noise, is suitable for the double-magnet design would be an improvement.

These suggestions should be taken as starting point for further research. Besides the previously mentioned directions that require additional attention, it is necessary to investigate what the influence of an external field on the movement of the cantilever and the magnetization direction of the magnet(s) would be.

Chapter 4

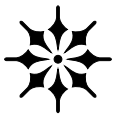

A Piezoelectric Based Design to Reduce External Vibrations

Prologue to the Chapter

In this standalone chapter we introduce a piezo-based design to attenuate environmental vibrations near the sample stage. The incentive to start this project is twofold: both testing the continuous spontaneous collapse (CSL)[199–201] model (more on this below) as achieving a micro-macro superposition (Sec. 1.1) that demands extremely high vibration isolation. The realization of a linear superposition of a macroscopic (e.g. a cantilever) and a microscopic (e.g. a spin) state allows one to investigate the borderline between quantum mechanics and classical mechanics, and the behaviour of macroscopic objects coupled with microscopic objects that unavoidably leads to the 'measurement problem'.[200,202]

Quantum theory accurately describes most physical phenomena and reduces to a classical theory in the macroscopic limit. The correctness of this transition can be traced back to the mass-dependence of wave characteristics, i.e. the wave behaviour of macroscopic objects is insignificant according to quantum mechanics. Despite the widespread success of quantum theory it comes with some difficulties that mainly arise in the crossover regime between the microscopic and the macroscopic world. In short, the complications originate from the linearity of quantum mechanics, which allows a linear superposition of distinct macroscopic states. An example of this type of dilemma constitutes the superposition of cantilever trajectories (Sec. 1.5), making it impossible to establish definite properties of the system. In a broader perspective: the inability to reconcile the indefiniteness and linearity of quantum mechanics with the definiteness and non-linearity of a macroscopic system, e.g. a measurement process, makes it impossible to consistently derive macroscopic physics starting at a microscopic level and to assign an indisputable boundary between the quantum and classical realm.[199]

A modified quantum theory in which dynamical reduction is incorporated has been proposed to overcome the aforementioned puzzle.[202,203] Out of the different models, the CSL model is the most advanced. Research in the past few decades was focused on various aspects of CSL[204–207] and even includes applications in cosmology.[208]

A detailed description of CSL is beyond the scope of this thesis, as such, we only briefly state the relevant features for the purpose of this discussion. The CSL model is based on the interaction of a fluctuating, stochastic field with an ensemble of particles causing collapse of their respective wave functions. The two parameters that characterize the collapse are the collapse rate λ and the characteristic length r_c, associated with the spatial localization of the collapse. The energy loss related to the collapse of the wave function brings about

a measurable change in the system's temperature if the experiment is operated within the boundaries set by the phenomenological parameters λ and r_c. As a result of the wave collapse the particles gain energy and due to the random fluctuations of the field, the particles perform a random walk. These side effects of CSL put restrictions on the parameters λ and r_c, thereby making it possible to test CSL. In practice, the collapse of the wave function can only be measured in an ultra-cold temperature regime.
In the Oosterkamp group we aim to address the 'measurement problem' with two different experiments. One is lowering the bounds on λ and r_c to test the CSL model and the other is achieving a spin-resonator superposition state. However, much work has to be done to bring such experiments within reach, e.g, achieving single-spin detection.

During previous efforts in our group to lower the bounds on the parameters it was found that external vibrations possibly heat up the experiment, obscuring the supposed heating by a wave function collapse. As such, we started a project to design an additional vibration isolation mechanism (see Sec. 2.6 for existing vibration isolation).
As an end of this rather lengthy prologue: the remainder of the chapter is structured as follows

1) *Design*
2) *Methods*
3) *Experimental results of piezo dissipation and control feedback*
4) *Improvements and future steps*

The main goal of this chapter is to provide a firm basis for further research on this project. The feasibility of the design presented here has yet to be confirmed, however the first results encourage to perform follow-up experiments.

4.1 Anti-vibration criteria and design principles

In this section we report on the general criteria an anti-vibration device has to satisfy in order to be applicable, introduce the piezo design and describe the attenuation mechanism, and passive and active control feedback.

4.1.1 Vibration isolation criteria

To keep the analysis succint we state the various criteria in bullet form. Since the aim of the design presented here is to reduce the amplitude of vibrations near the sample stage, it will be located between the bottom plate of the cryostat and the four-stage mass-spring system in which the experiment houses.

- *Length*: Due to the limited space below the cryostat the structure can be at most ~15 cm in length. This includes the suspension points.
- *Mass*: The structure has to be able to hold roughly 10 kg, while its own mass should be considerably lower to not exceed the carrying capacity of the cryostat.
- *Resonance frequency*: The natural resonance frequency of the device itself and the device in combination with the mass-spring system has to be far from the external frequencies. The most intense environmental excitations originate from the pulse tube, which resonates at 1.4 Hz and its higher harmonics.

Table 4.1: *Overview of the relevant piezo properties*

Specification	P-810.10	P-830.10
Resonance frequency (no load)	22 kHz	14 kHz
Response time	$\sim\mu s$	$\sim\mu s$
Mass	4 g	10 g
Length	20 ± 3 mm	22 ± 3 mm
Push force capacity	50 N	1000 N
Pull force capacity	1 N	5 N
Static large-signal stiffness[1]	$14 \pm 20\%$ N/μm	$57 \pm 20\%$ N/μm
Travel range at 0 to 100 V	$15 \pm 20\%$ μm	$15 \pm 20\%$ μm
Electrical capacitance	0.3 μF	1.5 μF

[1] The stiffness is roughly 4 times smaller at cryogenic temperatures.

Several properties of the two piezos types used in the experiments. Other specifications, not relevant in this context, can be found on the Physik Instrumente website.[209]

- *Heat conductance*: A high heat conduction between the device and bottom plate is required in order to accommodate the transport of dissipated heat to the bottom plate of the cryostat. To prevent heating of the experiment, a significant heat flow towards the sample stage should be prevented.
- *Feedback*: The nature of the incoming external vibrations, i.e. a frequency band, requires a method that allows vibration control through feedback, either passive or active, in a frequency range from 1 Hz to rougly 10 Hz.

Piezos are suitable for vibration damping in small spaces due to their low mass, small length-scale, high resonance frequency and extremely fast response time (see Tab. 4.1 for the specifications of piezos used in our experiments). For this reason our vibration isolation device is centered around piezos.
Piezos belong to the class of 'smart' materials,[210] a group of materials whose properties are coupled to multiple physical branches, e.g. mechanical, thermal and electrical. This allows a 'smart' material to modify a variable in one branch through its correlation with another branch. In piezo materials, the mechanical and electrical properties are related, which make them highly attractive for mechanical applications. Moreover, the fact that piezos can serve both as sensor and as actuator is another appealing feature that is frequently exploited in vibration isolation designs.

4.1.2 Design

The anti-vibration device is composed of two vertically stacked tube-shaped piezo transducers that can only expand or contract along their rotational-axis (Fig. 4.1).[1] The top piezo acts as a mechanical force-to-voltage transducer having the role of sensor and the bottom serves as an actuator providing mechanical feedback based on the sensor input.
A home-made base construction provides a stable casing for the piezos and two suspension

[1] In fact, a contraction or expansion in the perpendicular direction does always take place due to the Poisson effect (Sec. 4.1.3).

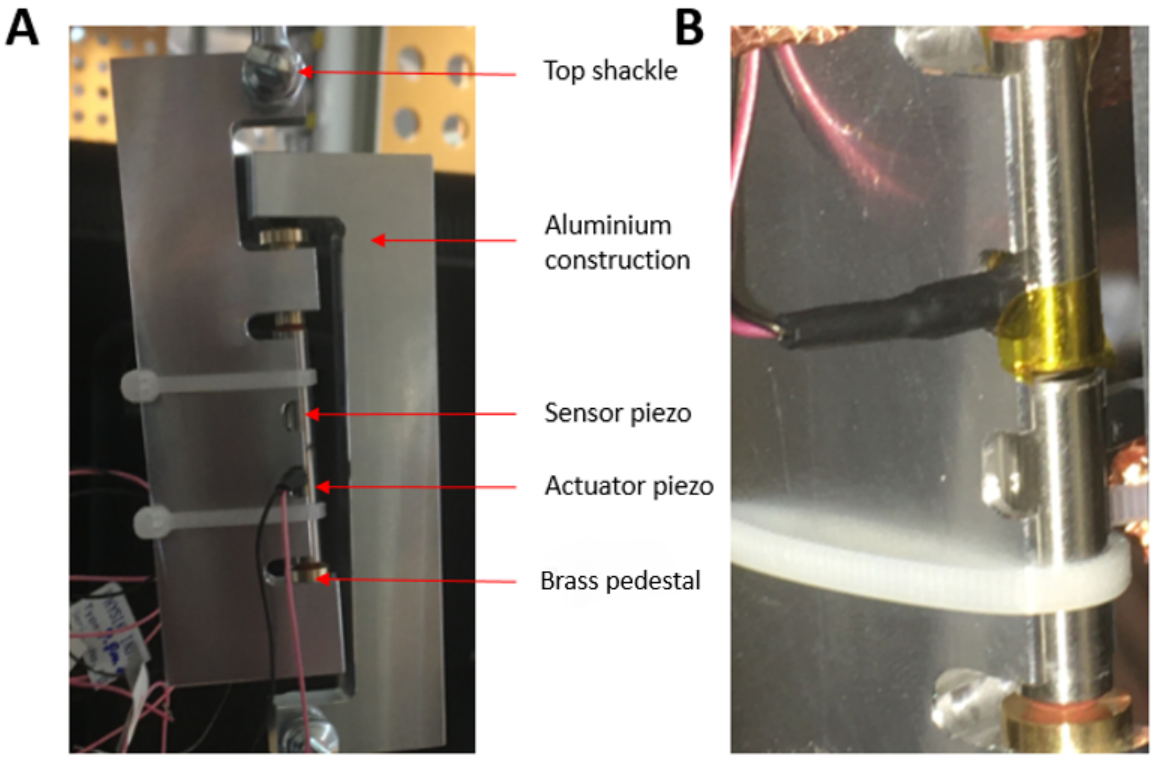

Figure 4.1: *a) A picture of the two piezos embedded in a home-designed base construction to accommodate suspension of the four-stage mass-spring system. The bottom piezo rests on a brass screw, while the top piezo is connected through another brass screw to the suspension weight. A shackle is used to attach the construction to the bottom plate of the cryostat. b) A zoom-in of the stacked piezos.*

points. One for a vibrating mass (the target mass is the four-stage mass-spring system) and another for the attachment to a fixed point (the target point is the bottom plate of the cryostat). This structure was *ad hoc* invented for its quick and cheap production, and its readiness to facilitate various test experiment that require different suspension forms and test masses. Once the double-piezo concept has proven its applicability, a more permanent design could be realized.
In our experiments we used one set of commercially available piezos, namely the P-810.10.[209] The P-810.10 was used in several proof-of-principle experiments, while the P-830.10 was initially meant to be used in the final design due to its larger push force capacity. As we will show later, a piezo with a larger travel range is preferred. For the purpose of discussing the experimental results, a list of the piezo's pertinent specifications is presented in Tab. 4.1.

4.1.3 Attenuation mechanism

Some dielectric materials, including piezos, exhibit the piezoelectric effect[211–213] that links the polarization in electrical domains to the lattice strain. These materials generate an electrically charged surface when they are subjected to a mechanical stress. The converse effect does also exist: a piezo exposed to an external electric field leads to a spontaneous change in the polarization and, subsequently, to a geometrical deformation.
The electric dipole moments in a material are inclined to be locally aligned in so-called Weiss domains, which in general have a random direction. Upon applying an external electric field, the dipoles tend to arrange themselves in a random order to neutralize the effect of the electric field. Some materials, however, are amenable to a permanent change of their dipole orientations through 'poling'. In this process, a material is exposed to a strong electric field

and the temperature is raised above its characteristic Curie temperature. Above the Curie point the material loses its intrinsic electric (and magnetic) orientation. The direction of the external electric field redirects the dipoles and thereby provides a non-vanishing polarization.
Poled materials, e.g. piezos, can provide macroscopic responses to an external electric field, because the dipoles collaborate as a collective instead of canceling each other. This holds only if the field does not exceed the poling electrical field and the operating temperature is not elevated above the Curie temperature. The expansion is pointed parallel to the poling axis (along the polarization direction) and as a result of the Poisson effect, a contraction unfolds in the perpendicular directions.
If a piezo is mechanically connected to a base structure, the piezo's geometrical deformation can be utilized to alter the dimensions of the base structure and as such, for example, to alleviate the influence of environmental vibrations. Since the electromechanical equations describing the relation between the strain, stress and electric field properties of such a composite structure can become rather complex, a computational model that incorporates all dynamics provides more insight.

4.1.4 Control feedback

A broad range of different piezo-based vibration control feedback mechanisms exists. Most forms are described by Moheimani[214] and in references within. Since most feedback variations are either hybrid or niche techniques, we focus on the more commonly used passive feedback[214–216] and active feedback,[212,214,217] i.e. passive and powered shunted piezoelectric control.
Similar to Eddy-current dampers that dissipate transformed mechanical-to-magnetic energy, shunted piezo damping is based on energy conversion. This feedback technique involves a piezo bonded to a vibrating structure and an electrical impedance circuit connected to the piezo electrodes. Each mechanical vibration of the structure is converted to an electrical signal through the piezoelectric effect and conveyed to the shunt circuit where it is dissipated as electrical energy. If this method is applied passively, the shunt is commonly operated with passive components, such as diodes, resistors, capacitors and inductors. Active control feedback, on the other hand, requires an external power source. The main performance discrepancy between the two methods is related to the number of vibration modes that can be effectively suppressed.

In a passive circuit the resonance frequency is tuned to match the (or a) resonance frequency of the composite structure. The precise value and type of shunt components greatly affects the behaviour around the resonance frequency and the experienced dissipation. For this reason, optimization plays a vast role in the performance, hence various studies were devoted to obtaining systematic methods to deduce the optimal parameters.[218] Since most practical situations require attenuation of multiple modes, multimodal vibration control methods were developed. This is typically realized by expanding the shunt circuit with additional components, either connected in series or parallel. Despite continuous efforts, the efficiency of passive multimode shunt circuits is often limited to a few resonance frequencies.[214] An easy solution would be to use multiple single-mode circuits, however, in practice, the space to implement anti-vibration devices is limited.
In active shunt circuits the impedance can be arbitrarily altered by manipulating the voltage or current. By constructing a circuit with an external power source such that the electrical resonance frequency can be modified to equal any resonance frequency of the composite structure and capitalizing on the fast response time of piezos, multiple frequencies can be

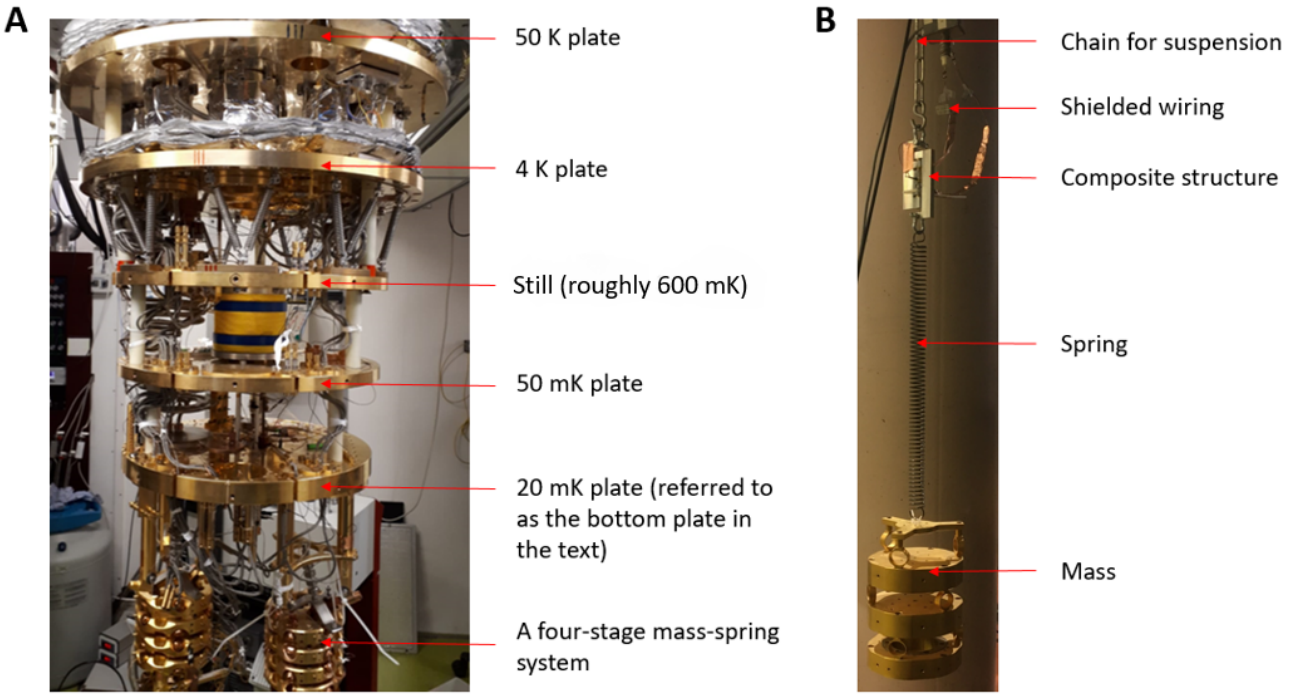

Figure 4.2: *Photograph of the cryostat in which the dissipation experiment was performed (a) and the setup during feedback experiments (b). Different configurations of the setup were used during various feedback attempts by changing the mass and the spring.*

effectively suppressed. These properties make active control particularly well-suited for multimode damping, i.e. this method tackles the problem of experiencing a frequency band as our device does. Drawbacks of active feedback could be related to stabilization or something specific to the situation.

We attempted to accomplish active feedback control on a vibrating mass of 13 kg with the device introduced in Sec. 4.1.2. Although we succeeded in driving the structure at its resonance frequency, the extremely large cross-talk capacitance of unknown origin between the piezos deteriorated the signal and made it impossible to perform adequate feedback. This issue remains the major obstacle that needs to be solved to achieve a fully functioning anti-vibration device. In Sec. 4.4 we discuss several suggestions that could disclose the source of the cross-talk and we expand on our efforts in Sec. 4.3.2.

4.2 Experimental setup

The goal of our dissipation experiment is to determine the maximal released heat, i.e. dissipation, of an expanding piezo without heating up the cryostat. Since the expansion is related to the voltage, it is a measure of the piezo's maximal obtainable displacement and hence, an indication of the amount of vibration attenuation we can achieve.
This experiment was performed in a dilution refrigerator (referred to as the cryostat) at roughly 12 mK, displayed in Fig. 4.2a. The physics of cooling a cryostat to mK temperatures are extensively described by Pobell in Ref. 219. A single piezo of the type P-810.10 was glued along its rotational-axis on the underside of the bottom plate. Both ends were free so the piezo could shrink and expand unimpeded. The piezo's electrodes were wired to a 24 pin connector, which is connected to the cryostat wiring.
Read-out of the cryostat temperature happened with resistive thermometers from Wim Bosch of HDL in Leiden[220] that allow an accurate resistance-temperature conversion. A voltage

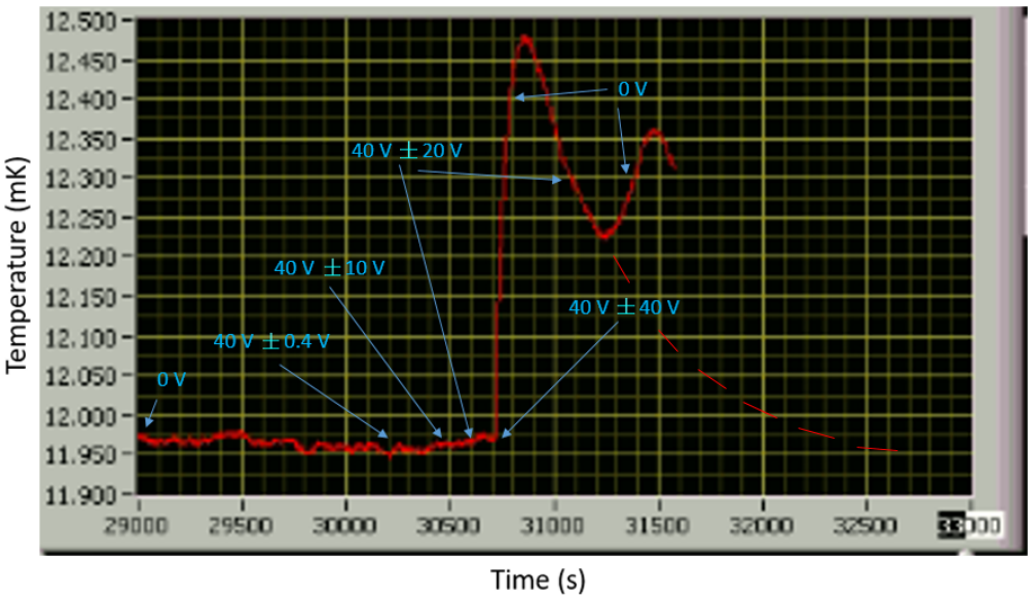

Figure 4.3: *The cryostat's bottom plate temperature as function of time. The arrows indicate the fluctuating voltage created over the piezo at the corresponding time. There were several intermediate voltages set between 40 V ± 0.4 V and 40 V ± 10 V, but they have been left out for clarity. The dashed line indicates the expected future course of the cooling curve. All signals were sent at a frequency of 1.4 Hz.*

difference across the piezo was created using a Zurich Instrument lock-in amplifier. During this experiment we used an offset voltage of 40 V to not negatively overload the piezo with a post amplifier that multiplies the input voltage by 20. The maximally tolerated dissipation was found by increasing the voltage till the released heat increased the cryostat's temperature.

The feedback experiments were performed at room temperature with a piezo type P-810.10. The device was attached to a ceiling mounted on an anti-vibration structure and at the bottom of the composite structure we suspended a spring, which was connected to a mass (Fig. 4.2b). The electrical circuit consisted of standard coax wiring, a Zurich Instrument lock-in amplifier and additional resistors and amplifiers that were connected in some configurations of the experiments.

4.3 Experimental results

In order to provide successors a complete overview of our control feedback endeavors, we report on our findings. These results are in no case satisfactory, but rather divulge our narrow insight in piezo-physics.
We start this section with the results from our piezo dissipation experiment, which are more conclusive. Furthermore, we briefly touch upon piezo hysteresis effects.

4.3.1 Piezo dissipation at millikelvin temperatures

The cooling power of the cryostat scales with the temperature squared. As mentioned in Sec. 2.3, the cooling power is 1.2 mW at 100 mK so $P_{cooling} \simeq 20\ \mu$W at 12 mK.
The results are showcased in Fig. 4.3, where the arrows indicate the voltage across the piezo as function of time. All signals were sent at a frequency of 1.4 Hz.

The fact that the temperature does not drop below 12 mK, while the base temperature of the cryostat is 8 mk, indicates that a heat leak is present.[2] This heat leak is roughly 20 μW. According to the dashed line in Fig. 4.3 it took ~27 minutes to return to ~12 mK after the piezo was turned off so the piezo dissipation as a result of 1.5 minute of expanding and shrinking at 40 V $\pm$ 40 V is $27 \cdot \left[\left(\frac{12.5}{12}\right)^2 \cdot 20 - 20\right] \simeq 45$ μW.
The highest voltage we sent that did not exceed the cooling power was 40 V $\pm$ 10 V. While 40 V $\pm$ 20 V led to some heating, which is tolerable, the heating at 40 V $\pm$ 40 V was so large that we stopped before waiting to see the cryostat's temperature reach an equilibrium. An additional dissipation experiment should be performed to give a more decisive answer of dissipation under load.

Now, let us calculate the displacement of a mass of 10 kg (comparable to the mass of the four-stage mass-spring system) due to pulse tube vibrations, and examine whether this movement can be reduced by piezo feedback. The pulse tube induced motion is approximately the speed of an incident vibration times its period, hence $\Delta x \simeq 10^{-5}/1.4 \simeq 7.1 \mu m$ (Sec. 2.6). Note that the speed is an upper bound, because we used the speed of fluctuations in the vicinity of the pulse tube and assumed no further attenuation throughout the cryostat. The change in piezo length as a result of gravity is given by $\Delta l_g = \frac{mg}{k}$. Using the values in Tab. 4.1, l_g = 28 μm for P-810.10 and l_g = 6.9 μm for P-830-10.
Given that the volumes of P-810.10 and P-830.10 are almost equal (Tab. 4.1) we expect their heat dissipation to be similar as well. Assuming V_{max} = 50 V: this translates to a maximal obtainable piezo displacement of 7.5 μm (Tab. 4.1). With a push force capacity of 50 N the P-810.10 can generate roughly 14.3 μm motion and the P-830.10 can even produce a movement of 70 μm so both piezos can reach the maximal achievable displacement of 7.5 μm.
Since neither the P-810.10 or the P-830.10 is expected to fully annihilate the effect of pulse tube vibrations under load, because the maximal tolerable voltage would be lower, a piezo with a larger traveling range is preferred, provided that its lower spring constant does not exacerbate the attenuation. Alternatively, let Δs be the travel range and k the spring constant. The feedback capacity scales with $k\Delta s$ so any piezo with a higher value of $k\Delta s$ provides more attenuation as long as its push capacity is large enough to reach its maximal obtainable displacement. Furthermore, the other properties of the piezo should meet the criteria outlined in Sec. 4.1.1. Importantly, the dissipation should be low enough to not significantly increase the refrigerator's temperature.

As a conclusion of this section: the dissipation is ~45 μW at the full range of piezo extension. The toleration limit is found to be 50 V and might even be higher, however this requires further investigations into the regime between 50 V and 60 V. Nonetheless, 50 V is sufficient to contribute a considerable amount of mechanical attenuation if a P-830-10 is used.

4.3.2 Active feedback attempts

The main objective of this section is to provide insight in our attempts to achieve active control feedback and to present our main findings. Due to the amount of different electrical circuits and mechanical configurations that were used during the experiments, the specific setup is delineated per case we explicitly discuss.
In order to demonstrate positive, active feedback and address the issue of cross-talk capa-

[2] There is always a heat leak present due to wires and the four-stage mass-spring system.

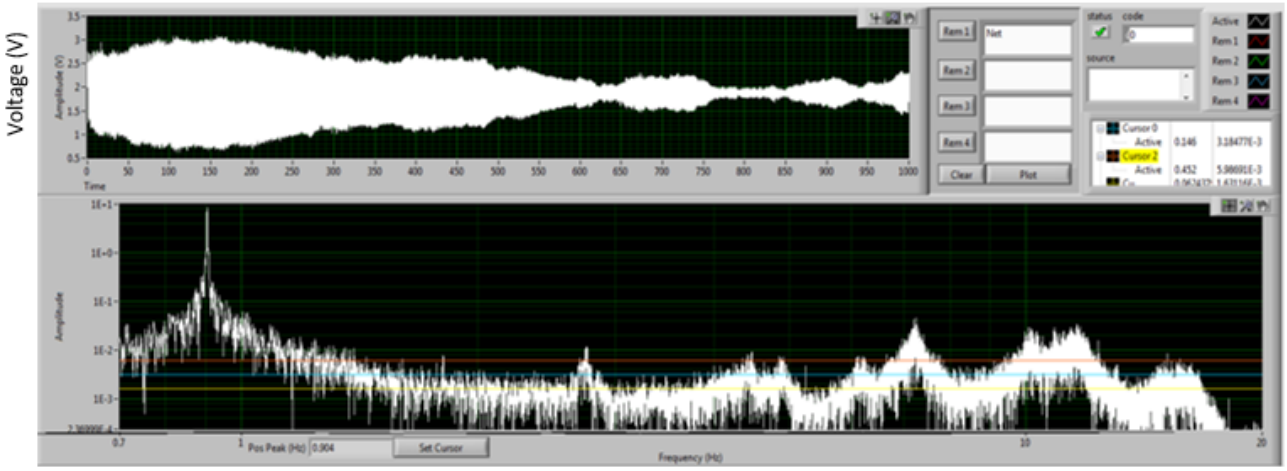

Figure 4.4: *Screenshot of a feedback experiment. The background signal is ~2 V_{RMS} ± 0.1 V_{RMS} (no external voltage set) and the V_{peak} signal that exceeds the background showcases a successful driving of the structure at its resonance frequency by creating a voltage difference of 2 V_{RMS} ± 0.1 V_{RMS}. The details of the setup are as stated in the text.*

citance, we consider two experiments (Fig. 4.4 and Fig. 4.6). Note that we use the pre-amplified value of the voltage in this section, which differs by a factor 20 from the amplified voltages.

4.3.2.1 Driven oscillations

For brevity we enumerate the important components used in this experiment.

- *Mechanical*: A mass of 13 kg and 1 spring (400 N/m).
- *Electrical*: A Zurich Instrument lock-in amplifier, a LPM driver (20x amplifier), a PXI, a SRS amplifier (gain = 2, 100 MΩ input impedance) and standard coax cables.

To avoid overloading the piezo with large negative voltages we added an offset voltage of 2 V_{RMS} to the Zurich Instrument lock-in signal. The electrical circuit used during this experiment is displayed in Fig. 4.5.
As visible in Fig. 4.4, when no voltage is set, the background peak voltage is roughly 0.1 V (e.g. between t = 770 and t = 830) due to environmental vibrations. This is the output signal from our sensor piezo without external input. By creating a voltage difference the size of

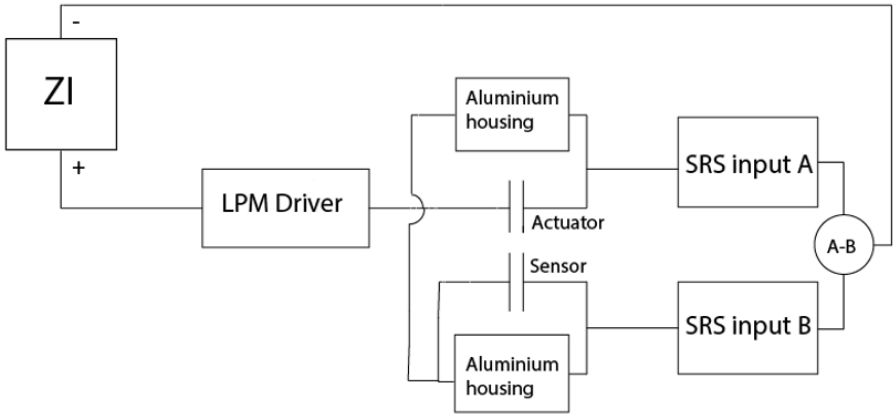

Figure 4.5: *The electrical circuit used during the experiment showcased in Fig. 4.4.*

the background signal, thus 2 $V_{RMS} \pm 0.1\ V_{RMS}$, at the resonance frequency (~0.9 Hz, see the peak at 0.9 Hz in the bottom graph of Fig. 4.4) between t = 650 and t = 750 we exceeded the background voltage and thus accomplished positive feedback. Between t = 0 and t = 200 we created 0.5 V_{RMS} and at t = 800 we briefly set 0.1 V_{RMS} again.
It has proven to be significantly more difficult to perform negative feedback than positive feedback. A possible reason could be the fast phase modulation that prevents feedback at a constant phase.

4.3.2.2 Cross-talk capacitance

Similarly as in the previous section we enumerate the relevant components used in this experiment.

- *Mechanical*: A mass of 13 kg and 4 springs (total 1600 N/m).
- *Electrical*: A Zurich Instrument lock-in amplifier, a LPM driver (20x amplifier), a PXI, a SRS amplifier (gain = 2, 100 MΩ input impedance) and standard coax cables.

All the wires in the proximity of the piezos or each other were shielded with copper tape. This resulted in a cross-talk reduction of roughly 6-8%. In addition, isolating the piezos from the aluminium base structure with poor electrically conducting kapton tape culminated in another decrease of about 80%.
The amount of cross-talk capacitance is related to the discrepancy between the measured voltage and the induced motion expressed in voltage. To start with the latter mentioned item; the width of the resonance 'circle' in Fig. 4.6a is approximately the movement of the piezos.
Driving the piezos at 1.766 Hz with 100 mV_{RMS} resulted in a measured voltage of 660 mV_{RMS} of which 75 mV_{RMS} was used to create a movement so the cross-talk voltage is 585 mV_{RMS}.
The cross-talk capacitance can be calculated from

$$C = \frac{I}{\omega V_{set}}, \tag{4.1}$$

where V_{set} is the created voltage and I the current $I = \frac{V_{measured}}{Z_c}$ with Z_c the impedance. Converting V_{RMS} to V_{peak} and $V_{pre-amplified}$ to $V_{amplified}$ gives C = 0.37 nF.

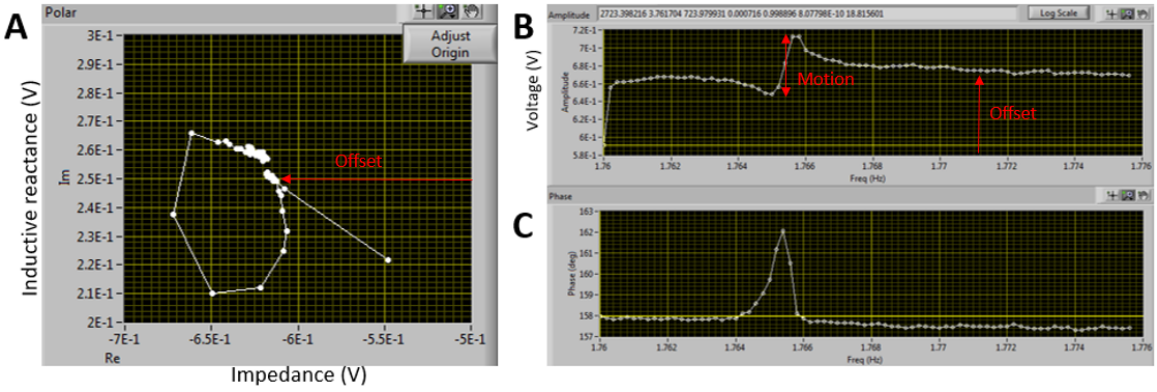

Figure 4.6: *A polar plot of the induced motion by driving the structure at its resonance frequency with 2 V_{RMS} (a) and diagrams of the amplitude (b) and phase (c) as function of the resonance frequency. The offset equals the cross-talk capacitance as discussed in the text. Each data point is calculated after a waiting time of 690 s. The details of the setup are as stated in the text.*

As a reference, the cross-talk capacitance of the composite structure with a load of 1.75 kg without shielding is about 3 nF. This implies that the cross-talk mainly arises from a capacitance between the piezos and between a piezo and the aluminium base structure. Even though our measures already led to a significant drop in the cross-talk, it is still several times larger than the piezo motion.
Let us calculate the cross-talk capacitance due to pulse tube vibrations to examine whether the measured capacitance might result from environmental fluctuations. Even though this experiment was operated at room temperature and under different isolation vibration circumstances than in a cryostat, we assume the same I as in Fig. 4.6, namely 6.6 nA, and the same amplitude of incident forces as pulse tube vibrations exhibit. The induced voltage across a piezo as a result of a single pulse tube vibration is roughly 50 V (Sec. 4.3.1) so the cross-talk capacitance is ~0.1 nF. This is of the same order as the measured capacitance so it is presumably that the measured cross-talk capacitance originates from environmental vibrations.

The Q-factor of the composite structure is $Q = \frac{FWHM}{f_0} \simeq 3000$ (Fig. 4.6b). This is in all likelihood an overestimation, because most other experiments yielded $Q \simeq 1000$, calculated from ring downs.

4.3.3 Hysteresis behaviour

We examined whether the piezos exhibited hysteresis effects, because this could alter their performance. In short, if a material experiences electrical hysteresis behaviour its macroscopic state value, e.g. the geometry if it concerns piezos, influenced by the hysteresis depends on the previously applied electrical field and its direction.
So far we did not encounter considerable hysteresis behaviour, nor was this expected, since the drives did not approach the poling field.

4.4 Improvement suggestions

There remain several pressing questions to be answered. To name a few: How to reduce the cross-talk capacitance further? Is the capacitance between the piezos and the base structure the only source of cross-talk? How much do the piezos 'see' each other and to what extent does that deteriorate their performance? How to maintain the phase at an arbitrarily fixed value? Is it possible to perform negative feedback with this design? Do the piezos show hysteresis behaviour at high drives?
It might be advantageous to tackle the aforementioned questions with a more systematic approach by exploiting the results presented in this chapter, rather than continuing with *ad hoc* trial-and-error experiments as we did, which required frequent and time-consuming debugging. To accommodate future research on this topic we suggest several improvements that are worth considering:

- *Reducing cross-talk between the piezos*: In our most recent experiments we shielded the piezos with a single layer of kapton tape, which is known for its exquisite electrical isolation properties at cryogenic temperatures. Supplementary layers will improve the total resistance and it is worthwhile to investigate the effect of other materials.
- *Reducing cross-talk between the base structure and piezos*: There is a cross-talk capacitance between the base structure and the piezos as we demonstrated in Sec. 4.3.2.2. This

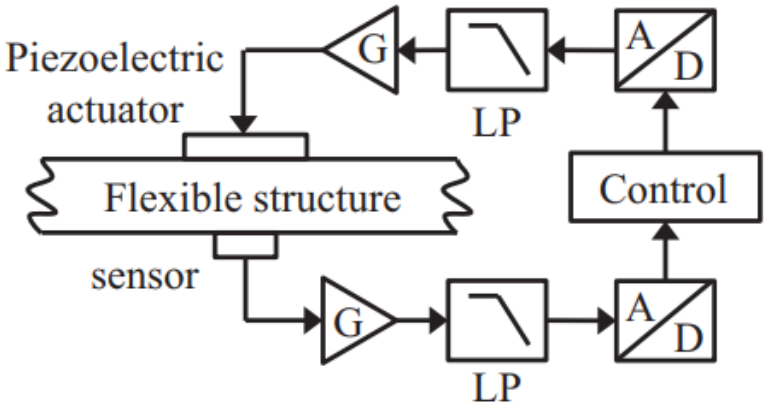

Figure 4.7: *Scheme of a standard piezo-based anti-vibration feedback device. G, LP and A/D represent amplifiers, filters and alternating-direct current converters, respectively. Figure reprinted from Gripp et al..*[216]

can be lowered by manufacturing a base structure of a high resistance material. Such a material prevents a variable current to connect the piezos via the base structure. Additionally, the material of screws that are being contacted by the piezos should also be fabricated with resistive material. Furthermore, the capacitance scales with the distance between a piezo and the base structure so increasing the separation would further decrease the cross-talk.

- *Separated circuits*: In order to fully understand and delineate the behaviour of the sensor and actuator piezo, their electrical circuits have to be separated. Once the effect of each component on the observed signal is known, their circuits can be combined to attempt feedback.
- *Flexible structure in-between two piezos*: To the authors knowledge, a damping system based on a stacked sensor and actuator piezo is uncommon. Generally, the basics of a piezo based anti-vibration device can be reduced to a compressible structure bounded by a pair of collocated piezos (Fig. 4.7). One of the piezos then serves as a sensor and upon each bending or expansion the actuator piezo behaves the opposite. Although the principles remain the same, the efficacy might be different than in our case.

Chapter 5

Conclusions and Outlook

Prologue to the Chapter

In this thesis, we examined whether single-spin detection at millikelvin temperatures with our current setup is achievable by setting up the requirements such an experiment has to satisfy. It turned out that this feat is not feasible under present conditions, therefore we investigated several improvements that bring single-spin detection within reach.
To conclude this work, we present a terse summary of each chapter. Thereafter we state the main conclusions of each chapter in bullet form and give an outlook on future steps towards single-spin detection.

5.1 Global thesis summary

Chapter 1: in this chapter we introduced MRFM and accompanying key concepts, such as force and force-gradient based detection, polarization and the resonant slice. We also presented various crucial aspects of our setup that have profound consequences for a measurement. Most issues can be traced back to the stringent demands to realize millikelvin temperatures.
Furthermore, we compared MRFM among other nanoMRI techniques and established that it is the only viable method to bridge the imaging gap, because it does not suffer from fundamental sensing restrictions. At last, we shed light on the quantum dynamics of a single-spin measurement and showed how, among other things, the magnetization direction of an individual spin can be opposed to the field direction, while the magnetization of an ensemble of spins is always aligned along the field.

Chapter 2: this chapter was devoted to the requirements of single-spin detection. These are the conditions that have to be satisfied to enable single-spin detection:

i) The relaxation times of the specific spin have to be sufficiently long to enable detection (Sec. 2.1 and Sec. 2.2).

ii) The minimal detectable magnetic moment in the setup has to be smaller than the electron magnetic moment (Sec. 2.2).

iii) Although there is no pre-determined value the SNR has to exceed to enable single-spin detection, the SNR of the measurement protocol has to be as high as possible to ease the detection of a single-spin signal (Sec. 2.2).

iv) The amplitude of the B_1 field has to satisfy the adiabatic condition without degrading the signal (Sec. 2.3).

v) The cantilever noise due to thermal fluctuations has to be smaller than the displacement induced by an individual spin or control feedback (Sec. 2.4).

vi) The resonant slice has to accommodate with great certainty at most a single spin (Sec. 2.5).

vii) The stability of the apparatus has to prevent fluctuations in the relative tip-sample distance to exceed the resonant slice thickness (Sec. 2.6).

Besides setting up the above requirements, we calculated the frequency shift as a result of various ARP pulse trains, which we suggest to perform as an intermediate step.

Chapter 3: in this chapter we investigated several improvements of the setup that, if implemented successfully, enable single-spin detection. The different enhancements that could facilitate a single-spin measurement are an external, static magnetic field sufficiently large to increase the polarization and fix the magnetization of both the spins and the probe magnet, a sample with a lower spin density than our current specimen, high-gradient nanomagnets and a nanocantilever with a high Q-factor.
We extended a previous study in our group of a double-magnet cantilever with two NdFeB micrometer-sized magnets by considering the combination of a cobalt nanometer-scale tip magnet in conjunction with a NdFeB micrometer-sized coupling magnet. The polarization, combined magnetic field and gradient field, and the magnetization as a result of this configuration were numerically studied.

Chapter 4: in this standalone chapter we reported on a novel piezo based damping device that should isolate the sample chamber from impeding environmental vibrations through active feedback. The main incentive to start this project is to lower the bounds on CSL parameters and achieve a macroscopic superposition.
This project is still in the early stages of testing, however we managed to measure the heat dissipation of the P-810.10 piezo and address several issues the prototype anti-vibration device experiences that prevent active feedback control. Most notable is the problem of cross-talk of capacitive nature between the piezos, and between a piezo and the base structure.

5.2 Conclusions

In this section we accumulate the main conclusions scattered throughout this thesis.

Chapter 2:

- The flip-flop time in our current sample is ~55 ms at a tip-sample distance of ~200 nm. For this calculation we modified the approach of Cardellino *et al.*[23] to be suitable for our situation that lacks certain experimental values. This yields a diffusion length of ~3 nm and a T_2 of ~250 μs, which is in accordance with a previous calculation performed by de Voogd[10] (Sec. 2.1.3.1).
- The minimal detectable magnetic moment in a 1 Hz bandwidth at 20 mK and at a tip-sample separation of ~200 nm is ~$8{\cdot}10^{-24}$ J/T, which is below $\mu_{electron} = 9.28 \cdot 10^{-24}$ J/T (Sec. 2.2).

- A force based method consisting of ARP pulses that have a HSn wave form provides the highest single-spin SNR if a micrometer-sized magnet is used. If a nanometer-scale magnet is used and a small or no external magnetic field is present piOSCAR yields the highest SNR (Sec. 2.2.2.2).
- A B_1 field strength of roughly 3 μT is required to adiabatically flip a spin (Sec. 2.3).
- The displacement of the cantilever caused by a fluctuating magnetic force produced by a single spin at a tip-sample spacing of 200 nm is ~0.45 nm. This is considerably larger than the RMS of the cantilever's thermal fluctuations at 20 mK: x_{RMS} = 20 pm (Sec. 2.4.4).
- The spin density (0.4 ppm) in our current sample is too high to enable the detection of a single spin. Our semi-arbitrarily chosen requirement that the resonant slice should with a 90% certainty contain at most a single spin is supported by the fact that Rugar *et al.*[8] measured a single spin in a resonance slice of 25 nm thickness and a sample with a spin density of ~0.4 ppb, which translates to a 97% certainty that a 25 nm thick slice houses at most a single spin (Sec. 2.5.2).
- The size of fluctuations in the relative tip-sample distance is ~1 pm. This is far below a typical resonant slice thickness (Sec. 2.6).

Chapter 3:

- Single-spin detection becomes attainable if a nanomagnet is employed and a sample with a spin density of 5 ppb is used. To enable single-spin detection with a micrometer-sized magnet, an even lower spin density is required (Sec. 3.2).
- In the double-magnet cantilever geometry: a cobalt tip nanomagnet with a diameter of 400 nm results in the optimal balance between size-reduction and left-over magnetization if no external field is present, while a cobalt tip magnet with a diameter of 200 nm provides the best result if an external field is present (Sec. 3.3.2).
- Using the previously mentioned nanomagnet with a diameter of 400 nm results in a polarization of ~0.5 of the spins within 100 nm of the tip magnet if no external field is present (Sec. 3.3.3.1).
- In the presence of a cobalt nanomagnet with a diameter of 400 nm and in the absence of an external field the field gradient is 1.5 MT/m at a tip-sample separation of 50 nm. This results in a diffusion length < 1 nm and a flip-flop time > 0.55 s in our current sample. Even more propitious values are reached in the Qnami sample (Sec. 3.3.4).
- Nanoladder cantilevers are preferred over nanowires due to their direct applicability in our current setup (Sec. 3.4.1). Moreover, they provide a higher SNR than our regular micrometer-scale cantilevers (Sec. 3.4.3).

Chapter 4:

- The maximal tolerable voltage across a piezo type P-810.10 without heating up the environment lies between 50 V and 60 V (Sec. 4.3.1).
- The heat dissipation of a piezo type P-810.10 is less than ~20 μW at 40 V $\pm$ 10 V (Sec. 4.3.1).
- The obtainable amount of mechanical attenuation without heating up the environment of a piezo type P-830.10 is over 50% of the expected fluctuation size (Sec. 4.3.1).

- There exists a capacitive cross-talk between the piezos that prevents active, negative feedback control. Isolating the piezos from each other and the environment with a high resistance material reduces the cross-talk with roughly 80% (Sec. 4.3.2).

5.3 Outlook

Throughout this thesis we suggested several follow-up experiments and improvements of the current setup of which most are summarized in Sec. 2.2.3, Sec. 3.5 and Sec. 4.4. Further research towards single-spin detection should be directed at the implementation of a sample with a lower spin density, testing various wave forms and protocols, studying the dissipation as a result of the double-magnet cantilever and the realization of a nanometer-sized tip magnet.
Several issues remain to be solved. To name a few: the rather short T_2 time in our current sample (which is not expected to differ much in a sample with a lower spin density, see Sec. 3.3.4) could be troublesome in experiments as experienced and explained by de Voogd[10] and the SNR might be so low that numerous hours of averaging are required to distinguish a spin signal from noise.
Altogether, single-spin detection at ~20 mK appears to be feasible provided that several technical improvements are carried out. This feat paves the way towards new exciting applications (Sec. 1.1).

ACKNOWLEDGEMENTS

I would like to thank Tjerk for supervising me during this project. I really enjoyed your motivation and our discussions from which I learned a lot. I also want to thank Freek for his never ending enthusiasm, fun conversation topics during lunch and helping me out with numerous questions. Furthermore, I also want to express my gratitude to Gesa for helping me understand some of the finer details of various topics studied in our group, and to Tim for helping me out with various small problems I faced, e.g. not knowing where to find a certain object or what device to use for a certain task.
I am also grateful to the other people in our group (Victor, Ruben, Jaimy, Çağan, Jean-Paul and Ilse) and the other people in the meethal for providing a pleasant atmosphere. Special thanks to Kier for giving me more insight in electromechanics, helping with the piezo experiments and the fun stories. Finally, I would like to thank the people from the FMD and the ELD for fabricating the piezo base structure and helping with various other questions.

This research was made possible by financial support from the Dutch Association for Scientific Research (NWO) and the Foundation for Fundamental Research of Matter (FOM).

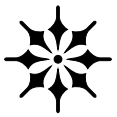

BIBLIOGRAPHY

[1] Sidles, J. A. Noninductive detection of single-proton magnetic resonance. *Appl. Phys. Lett.* **58**, 2854–2856 (1991).

[2] Sidles, J. *et al.* Magnetic Resonance Force Microscopy. *Rev. Mod. Phys.* **67**, 249–265 (1995).

[3] Poggio, M. *et al.* Force-detected nuclear magnetic resonance. Tech. Rep., Basel University (2017).

[4] Berman, G. P. *et al. Magnetic Resonance Force Microscopy and a Single-Spin Measurement* (World Scientific Publishing, 2006).

[5] Kuehn, S. *et al.* Advances in mechanical detection of magnetic resonance. *J. Chem. Phys.* **128**, 052208 (2008).

[6] Poggio M, D. C. Magnetic Resonance Force Micrsocopy (2012).

[7] Poggio, M. *et al.* Force-detected nuclear magnetic resonance: Recent advances and future challenges. *Nanotechnology* **21**, 1–13 (2010).

[8] Rugar, D. *et al.* Single spin detection by magnetic resonance force microscopy. *Nature* **430**, 329–332 (2004).

[9] de Wit, M. *Advances in SQUID-detected magnetic resonance force microscopy*. Ph.D. thesis, Leiden University (2019).

[10] de Voogd, M. *Magnetic Resonance Force Microscopy and the spin bath : towards single-spin massive-resonator entanglement and the spoiling influence of the spin bath*. Ph.D. thesis, Leiden University (2018).

[11] Haan, A. *Nuclear magnetic resonance force microscopy at millikelvin temperatures*. Ph.D. thesis, Leiden University (2016).

[12] Wagenaar, J. *Magnetic resonance force microscopy for condensed matter*. Ph.D. thesis, Leiden University (2017).

[13] Wijts, G. *Magnetic resonance force microscopy at milliKelvin temperatures*. Ph.D. thesis, Leiden University (2013).

[14] Rugar, D. *et al.* Mechanical detection of magnetic resonance. *Nature* **360**, 563–562 (1992).

[15] Rugar, D. *et al.* Force Detection of Nuclear Magnetic Resonance. *Science (80-.).* **264**, 1560–1563 (1994).

[16] Degen, C. L. *et al.* Nanoscale magnetic resonance imaging. *PNAS Febr.* **3**, 1313–1317 (2009).

[17] Grob, U. *et al.* Magnetic resonance force microscopy with a one-dimensional resolution of 0.9 nanometers. *Arxiv* (2019).

[18] Stipe, B. C. *et al.* Electron Spin Relaxation Near a Micron-Size Ferromagnet. *Phys. Rev. Lett.* **87**, 277602 (2001).

[19] De Wit, M. *et al.* Density and T1 of Surface and Bulk Spins in Diamond in High Magnetic Field Gradients. *Phys. Rev. Appl.* **10**, 1 (2018).

[20] Wagenaar, J. J. *et al.* Probing the Nuclear Spin-Lattice Relaxation Time at the Nanoscale. *Phys. Rev. Appl.* **6**, 014007 (2016).

[21] Degen, C. L. *et al.* Role of spin noise in the detection of nanoscale ensembles of nuclear spins. *Phys. Rev. Lett.* **99**, 250601 (2007).

[22] Budakian, R. *et al.* Suppression of Spin Diffusion near a Micron-Size Ferromagnet. *Phys. Rev. Lett.* **92**, 4 (2004).

[23] Cardellino, J. *et al.* The effect of spin transport on spin lifetime in nanoscale systems. *Nat. Nanotechnol.* **9**, 343–347 (2014).

[24] Den Haan, A. M. *et al.* Spin-mediated dissipation and frequency shifts of a cantilever at milliKelvin temperatures. *Phys. Rev. B - Condens. Matter Mater. Phys.* **92**, 235441 (2015).

[25] de Wit, M. *et al.* Feasibility of imaging using Boltzmann polarization in nuclear Magnetic Resonance Force Microscopy. *J. Appl. Phys.* **125**, 083901 (2019).

[26] Budakian, R. *et al.* Creating Order from Random Fluctuations in Small Spin Ensembles. *Science (80-.).* **307**, 408–411 (2005).

[27] Mamin, H. J. *et al.* Detection and manipulation of statistical polarization in small spin ensembles. *Phys. Rev. Lett.* **91**, 207604 (2003).

[28] Poggio, M. *et al.* Nuclear double resonance between statistical spin polarizations. *Phys. Rev. Lett.* **102**, 087604 (2009).

[29] Lee, I. *et al.* Nanoscale scanning probe ferromagnetic resonance imaging using localized modes. *Nature* **466**, 845–848 (2010).

[30] Zhang, Z. *et al.* Observation of ferromagnetic resonance in a microscopic sample using magnetic resonance force microscopy. *Appl. Phys. Lett.* **68**, 2005–2007 (1996).

[31] Kinoshita, Y. *et al.* Magnetic resonance force microscopy using ferromagnetic resonance of a magnetic tip excited by microwave transmission via a coaxial resonator. *Nanotechnology* **29**, 485709 (2018).

[32] Obukhov, Y. *et al.* Local ferromagnetic resonance imaging with magnetic resonance force microscopy. *Phys. Rev. Lett.* **100**, 197601 (2008).

[33] Wago, K. *et al.* Paramagnetic and ferromagnetic resonance imaging with a tip-on-cantilever magnetic resonance force microscope. *Appl. Phys. Lett.* **72**, 2757–2759 (1998).

[34] Vinante, A. *et al.* Magnetic resonance force microscopy of paramagnetic electron spins at millikelvin temperatures. *Nat. Commun.* **2** (2011).

[35] Abragam, A. *Principles of Nuclear Magnetism* (Oxford University Press, 1961).

[36] Slichter, C. *Principles of Magnetic Resonance* (Springer, 1990).

[37] Rugar, D. *et al.* Atomic Force Microscopy. *Phys. Today* 23–30 (1990).

[38] Giessibl, F. J. Advances in atomic force microscopy. *Rev. Mod. Phys.* **75**, 949–983 (2003).

[39] Sidles, J. *et al.* Signal-To-Noise Ratios in Inductive and Mechanical Detection of Magnetic Resonance. *Phys. Rev. Lett.* **70**, 3506–3509 (1993).

[40] Ciobanu, L. *et al.* Ciobanu - 3D MR microscopy with resolution 3,7um by 3,3um by 3,3um. *J. Magn. Reson.* 178–182 (158).

[41] Berman, P. *et al.* Spin relaxation caused by thermal excitations of high-frequency modes of cantilever vibrations. *Phys. Rev. B - Condens. Matter Mater. Phys.* **68**, 094402 (2003).

[42] Clarke, J. *et al. The SQUID Handbook* (Wiley-VCH, 2006).

[43] Stroscio, J. *et al. Scanning Tunneling Microscopy* (Academic Press, 1993).

[44] Jelezko, F. *et al.* Single spin states in a defect center resolved by optical spectroscopy. *Appl. Phys. Lett.* **81**, 2160–2162 (2002).

[45] Elzerman, J. M. *et al.* Single-shot read-out of an individual electron spin in a quantum dot. *Nature* **430**, 431–435 (2004).

[46] Durkan, C. *et al.* Electronic spin detection in molecules using scanning-tunneling- microscopy-assisted electron-spin resonance. *Appl. Phys. Lett.* **80**, 458–460 (2002).

[47] Schirhagl, R. *et al.* Nitrogen-Vacancy Centers in Diamond: Nanoscale Sensors for Physics and Biology. *Annu. Rev. Phys. Chem.* **65**, 83–105 (2014).

[48] Jelezko, F. *et al.* Molecules Spectroscopy of Single N-V Centers in Diamond. *Single Mol.* **2**, 255–260 (2001).

[49] Rondin, L. *et al.* Magnetometry with nitrogen-vacancy defects in diamond. *Reports Prog. Phys.* **77**, 056503 (2014). `1311.5214`.

[50] Childress, L. *et al.* Diamond NV centers for quantum computing and quantum networks. *MRS Bull.* **38**, 134–138 (2013).

[51] Gordon, L. *et al.* Quantum computing with defects. *MRS Bull.* **38**, 802–808 (2013).

[52] Subramaniam, S. Bridging the imaging gap: Visualizing subcellular architecture with electron tomography. *Curr. Opin. Microbiol.* **8**, 316–322 (2005).

[53] Hanson, L. G. Is quantum mechanics necessary for understanding magnetic resonance? *Concepts Magn. Reson. Part A Bridg. Educ. Res.* **32**, 329–340 (2008).

[54] Feynman, R. P. *et al.* Geometrical Representation of the Schrödinger Equation for Solving Maser Problems. *J. Appl. Phys.* **28**, 49–52 (1957).

[55] Bloch, F. Nuclear Induction. *Phys. Rev.* **70**, 460–474 (1946).

[56] Berman, G. P. *et al.* A Model for Quantum Jumps in Magnetic Resonance Force Microscopy. *Phys. Lett. A* **337**, 161–165 (2005).

[57] Nguyen, H. L. *et al.* Reverse Monte Carlo reconstruction of electron spin-label coordinates from scanned-probe magnetic resonance microscope signals. *Arxiv* (2018).

[58] Anahory, Y. *et al.* SQUID-on-tip with single-electron spin sensitivity for high-field and ultra-low temperature nanomagnetic imaging. *Arxiv* (2020).

[59] Gridneva, I. V. *et al.* Phase Transition in Diamond-Structure Crystals during Hardness Measurements. *Phys. status solidi a* **14**, 177–182 (1972).

[60] Loubser, J. H. N. *et al.* Electron spin resonance in the study of diamond. *Reports Prog. Phys.* **41**, 1201–1248 (1978).

[61] Danilenko, V. On the History of the Discovery of Nanodiamond Synthesis. *Phys. Solid State* **46**, 581–584 (2004).

[62] Lee, S.-T. *et al.* CVD diamond films: nucleation and growth. *Mater. Sci. Eng.* **25**, 123–154 (1999).

[63] Coe, S. E. *et al.* Optical, thermal and mechanical properties of CVD diamond. *Diam. Relat. Mater.* **9**, 1726–1729 (2000).

[64] Osswald, S. *et al.* Control of sp2/sp3 carbon ratio and surface chemistry of nanodiamond powders by selective oxidation in air. *J. Am. Chem. Soc.* **128**, 11635–11642 (2006).

[65] Zhang, Q. *et al.* Fluorescent PLLA-nanodiamond composites for bone tissue engineering. *Biomaterials* **32**, 87–94 (2011).

[66] Mochalin, V. N. *et al.* The properties and applications of nanodiamonds. *Nat. Nanotechnol.* **7**, 11–23 (2012).

[67] Longenecker, J. G. *et al.* High-gradient nanomagnets on cantilevers for sensitive detection of nuclear magnetic resonance. *ACS Nano* **6**, 9637–9645 (2012).

[68] Su, D. *et al.* Oxidative dehydrogenation of ethylbenzene to styrene over ultra-dispersed diamond and onion-like carbon. *Carbon N. Y.* **45**, 2145–2151 (2007).

[69] Chow, E. K. *et al.* Nanodiamond Therapeutic Delivery Agents Mediate Enhanced Chemoresistant Tumor Treatment. *Sci. Transl. Med.* **3**, 73–82 (2011).

[70] Hornstra, J. Dislocations in the Diamond Lattice. *J. Phys. Chem. Solids* **5**, 129–141 (1958).

[71] Davies, G. *et al.* Vacancy-related centers in diamond. *Phys. Rev. B* **46**, 13157–13170 (1992).

[72] Breuer, S. J. *et al.* Ab initio investigation of the native defects in diamond and self-diffusion. *Pysical Rev. B* **51**, 6984–6994 (1995).

[73] Breeding, C. M. *et al.* The "Type" Classification System of Diamonds and its Importance in Gemology. *Gems Gemol.* **45**, 96–111 (2009).

[74] Briddon, P. R. *et al.* Theory of impurities in diamond. *Phys. B* **185**, 179–189 (1993).

[75] Kajihara, S. A. *et al.* Nitrogen and Potential n-Type Dopants in Diamond. *Phys. Rev. Lett.* **66**, 2010–2013 (1991).

[76] Briddon, P. *et al.* Hydrogen in diamond. *J. Phys. C Solid State Phys* **21**, 1027–1058 (1988).

[77] Kajihara, S. A. *et al.* Impurity incorporation and doping of diamond. *Phys. B* **185**, 144–149 (1993).

[78] Rohrer, E. *et al.* Nitrogen-related dopant and defect states in CVD diamond. *Phys. Rev. B* **54**, 7874–7880 (1996).

[79] Iakoubovskii, K. *et al.* Optical transitions at the substitutional nitrogen centre in diamond. *J. Phys. Condens. Matter* **12**, 77–81 (2000).

[80] Farrer, R. On the substitutional nitrogen donor in diamond. *Solid State Commun.* **7**, 685–688 (1969).

[81] Walker, A. B. *et al.* Electronic properties of CVD diamond. *Semicond. Sci. Technol.* **18**, 1–11 (2003).

[82] Bower, H. *et al.* Electron Spin Resonance Spectra associated with Nitrogen in Diamonds. *Nat. Publ. Gr.* **210**, 1037–1038 (1966).

[83] Smith, W. *et al.* Electron Spin Resonance of Acceptor States in Diamond. *J. Appl. Phys.* **27**, 5 (1956).

[84] Van Wyk, J. A. *et al.* The dependences of ESR line widths and spin -spin relaxation times of single nitrogen defects on the concentration of nitrogen defects in diamond. *J. Phys. D Appl.* **30**, 78961–78968 (1997).

[85] Cook, R. J. *et al.* Electron nuclear double resonance study of a nitrogen centre in diamond. *Proc. R. Soc. A* **295**, 99–106 (1966).

[86] Cox, A. *et al.* C13, N14 and N15 ENDOR measurements on the single substitutional nitrogen centre (P1) in diamond. *Phys. J. Condens. Matter* **6**, 551–563 (1994).

[87] Loubser, J. H. N. *et al.* New lines in the electron spin resonance spectrum of substitutional nitrogen donors in diamond Related content Electron spin resonance in the study of diamond. *Br. J. Appl. Phys.* **16**, 457–462 (1965).

[88] Gimarc, B. M. Applications of Qualitative Molecular Orbital Theory. *Acc. Chem. Res.* **7**, 384–392 (1974).

[89] Smith, D. W. The Antibonding Effect. *J. Chem. Educ.* **77**, 30 (2000).

[90] Pople, J. *et al. Approximate Molecular Orbital Theory* (McGraw-Hill book company, 1970).

[91] Molecular orbitals and covalent bonding. URL https://chem.libretexts.org/Bookshelves/Organic_Chemistry/Map%3A_Organic_Chemistry_(Vollhardt_and_Schore)/01._Structure_and_Bonding_in_Organic_Molecules/1.7%3A_Molecular_Orbitals_and__Covalent_Bonding. Accessed on: 12-02-2020.

[92] Bersuker, I. B. *The Jahn-Teller Effect* (Cambridge University Press, 2006).

[93] Bachelet, G. B. *et al.* Defects in diamond: The unrelaxed vacancy and substitutional nitrogen. *Phys. Rev. B* **24**, 4736–4744 (1981).

[94] Takahashi, S. *et al.* Quenching spin decoherence in diamond through spin bath polarization. *Phys. Rev. Lett.* **101**, 047601 (2008).

[95] Kutter, C. *et al.* Electron-Spin Echoes at 604 GHz Using Far Infrared Lasers. *Phys. Rev. Lett.* **74**, 2925–2928 (1995).

[96] Childress, L. *et al.* Coherent Dynamics of Coupled Electron and Nuclear Spin Qubits in Diamond. *Science (80-.).* **324**, 281–285 (2009).

[97] Jarmola, A. *et al.* Temperature- and magnetic-field-dependent longitudinal spin relaxation in nitrogen-vacancy ensembles in diamond. *Phys. Rev. Lett.* **108**, 197601 (2012).

[98] Chudnovsky, E. M. *et al.* Universal mechanism of spin relaxation in solids. *Phys. Rev. B - Condens. Matter Mater. Phys.* **72** (2005).

[99] Reynhardt, E. C. *et al.* Temperature dependence of spin-spin and spin-lattice relaxation times of paramagnetic nitrogen defects in diamond. *J. Chem. Phys.* **109**, 8471–8477 (1998).

[100] Sorokin, P. *et al.* Cross Relaxation Studies in Diamond. *Phys. Rev.* **118**, 939–945 (1960).

[101] Bloembergen, N. *et al.* Cross-Relaxation in Spin Systems. *Phys. Rev.* **114**, 445–459 (1959).

[102] Burk, D. *et al.* Atomic Heat of Diamond from 11 to 200 K. *Phys. Rev.* **111**, 1275–1282 (1958).

[103] Herzog, B. E. *et al.* Boundary between the thermal and statistical polarization regimes in a nuclear spin ensemble. *Appl. Phys. Lett.* **105**, 043112 (2014).

[104] Mamin, H. J. *et al.* Magnetic resonance force microscopy of nuclear spins: Detection and manipulation of statistical polarization. *Phys. Rev. B - Condens. Matter Mater. Phys.* **72**, 024413 (2005).

[105] Xue, F. *et al.* Measurement of statistical nuclear spin polarization in a nanoscale GaAs sample. *Phys. Rev. B - Condens. Matter Mater. Phys.* **84** (2011).

[106] Vugmeister, B. E. Spin Diffusion and Spin-Lattice Relaxation in Paramagnetic Crystals. *Basic Solid State Phys.* **90**, 711–718 (1978).

[107] Cardellino, J. *et al.* Supplementary Information: The effect of spin transport on spin lifetime in nanoscale systems. *Nat. Nanotechnol.* **9**, 343–347 (2014).

[108] De Voogd, J. M. *et al.* Dissipation and resonance frequency shift of a resonator magnetically coupled to a semiclassical spin. *Sci. Rep.* **7** (2017).

[109] Hao, Z. *et al.* An analytical model for support loss in micromachined beam resonators with in-plane flexural vibrations. *Sensors Actuators, A Phys.* **109**, 156–164 (2003).

[110] Chudnovsky, E. M. *et al.* Damping of a nanocantilever by paramagnetic spins. *Phys. Rev. B - Condens. Matter Mater. Phys.* **89** (2014).

[111] Stipe, B. C. *et al.* Noncontact friction and force fluctuations between closely spaced bodies. *Phys. Rev. Lett.* **87**, 968011–968014 (2001).

[112] Kuehn, S. *et al.* Dielectric fluctuations and the origins of noncontact friction. *Phys. Rev. Lett.* **96** (2006).

[113] Moore, E. W. *et al.* Evading surface and detector frequency noise in harmonic oscillator measurements of force gradients. *Appl. Phys. Lett.* **97**, 044105 (2010).

[114] Rugar, D. *et al.* Mechanical Parametric Amplification and Thermomechanical Noise Squeezing. *Phys. Rev. Lett.* **67**, 699–702 (1991).

[115] Bruland, K. J. *et al.* Anharmonic modulation for noise reduction in magnetic resonance force microscopy. *Rev. Sci. Instrum.* **66**, 2853–2856 (1995).

[116] Marohn, J. A. *et al.* Mechanical modulation of sample magnetization in magnetic resonance force microscopy. *J. Appl. Phys.* **86**, 4619–4625 (1999).

[117] Garbini, J. L. *et al.* Optimal control of force microscope cantilevers. I. Controller design. *J. Appl. Phys.* **80**, 1951–1958 (1996).

[118] Mertz, J. *et al.* Regulation of a microcantilever response by force feedback. *Appl. Phys. Lett.* **62**, 2344–2346 (1993).

[119] Wago, K. *et al.* Force-detected electron-spin resonance:Adiabatic inversion, nutation, and spin echo. *Phys. Rev. B* **57**, 108–1114 (1998).

[120] Meiboom, S. *et al.* Modified spin-echo method for measuring nuclear relaxation times. *Rev. Sci. Instrum.* **29**, 688–691 (1958).

[121] Leibovich, N. *et al.* Aging Wiener-Khinchin Theorem. *Phys. Rev. Lett.* **115**, 080602 (2015).

[122] Poggio, M. *et al.* Nuclear magnetic resonance force microscopy with a microwire rf source. *Appl. Phys. Lett.* **90**, 263111 (2007).

[123] Tannús, A. *et al.* Adiabatic Pulses. *NMR Biomed* **10**, 423–434 (1997).

[124] Redfield, A. Nuclear Magnetic Resonance Saturation and Rotary Saturation in Solids*. *Phys. Rev.* **98**, 1787–1809 (1955).

[125] Miller, C. W. *et al.* Quantitative determination of the adiabatic condition using force-detected nuclear magnetic resonance. *Phys. Rev. B - Condens. Matter Mater. Phys.* **72**, 224402 (2005).

[126] Berman, G. P. *et al.* Single-spin measurement and decoherence in magnetic-resonance force microscopy. *Phys. Rev. B - Condens. Matter Mater. Phys.* **67**, 094425 (2003).

[127] Levitt, M. *et al.* NMR Population Inversion Using a Composite Pulse. *J. Magn. Reson.* **33**, 473–476 (1969).

[128] Shaka, A. *et al.* Symmetric Phase Alternating Composite Pulses. *J. Magn. Reson.* **71**, 495–503 (1987).

[129] Emsley, L. *et al.* Self-refocusing effect of 270 deg gaussian pulses: applications to selective two-dimensional exchange spectroscopy. *Journal of Magnetic Resonance* **82**, 211–218 (1989).

[130] Baum, J. *et al.* Broadband and adiabatic inversion of a two-level system by phase-modulated pulses. *Phys. Rev. A* **32**, 3435–3447 (1985).

[131] Norris, D. *et al.* An Analysis of the Effects of Short T2 Values on the Hyperbolic-Secant Pulse. *J. Magn. Reson.* **92**, 94–101 (1991).

[132] Hajduk, P. *et al.* Theoretical analysis of relaxation during shaped pulses. I. The effects of short T1 and T2. *J. Magn. Reson.* **103**, 40–52 (1993).

[133] Horita, D. *et al.* Theoretical analysis of relaxation during shaped pulses II The effects of cross relaxation. *J. Magn. Reson.* **103**, 53–60 (1993).

[134] Silver, M. S. *et al.* Selective spin inversion in nuclear magnetic resonance and coherent optics through an exact solution of the Bloch-Riccati equation. *Phys. Rev. A* **31**, 2753–2755 (1985).

[135] Peddibhotla, P. *et al.* Harnessing nuclear spin polarization fluctuations in a semiconductor nanowire. *Nat. Phys.* **9**, 631–635 (2013).

[136] Tomka, I. T. *et al.* Spatio-chemical characterization of a polymer blend by magnetic resonance force microscopy. *R. Soc. Chem.* **15**, 3438–3441 (2013).

[137] Berman, G. P. *et al.* Theory of frequency shifts in the oscillating cantilever-driven adiabatic reversals technique as a function of the spin location. *Phys. Rev. B - Condens. Matter Mater. Phys.* **72** (2005).

[138] Lee, S. *et al.* Unified picture of cantilever frequency shift measurements of magnetic resonance. *Phys. Rev. B - Condens. Matter Mater. Phys.* **85**, 165447 (2012).

[139] Mamin, H. J. *et al.* Nuclear magnetic resonance imaging with 90-nm resolution. *Nature Nanotechnology* **2**, 301–306 (2007).

[140] Bloembergen, N. *et al.* Bloembergen - Relaxation Effects in Nuclear Magnetic Resonance Absorytion. *Phys. Rev.* **73** (1948).

[141] Yazdanian, S. M. *et al.* Quantifying electric field gradient fluctuations over polymers using ultrasensitive cantilevers. *Nano Lett.* **9**, 2273–2279 (2009).

[142] Isaac, C. E. *et al.* Dynamic nuclear polarization in a magnetic resonance force microscope experiment. *Phys. Chem. Chem. Phys.* **18**, 8806–8819 (2016). 1601.07253.

[143] Yazdanian, S. M. *et al.* Dielectric fluctuations in force microscopy: Noncontact friction and frequency jitter. *J. Chem. Phys.* **128**, 224706 (2008).

[144] Bruland, K. J. *et al.* Optimal control of force microscope cantilevers. II. Magnetic coupling implementation. *J. Appl. Phys.* **80**, 1959–1964 (1996).

[145] Prost, J. *et al.* Generalized fluctuation-dissipation theorem for steady-state systems. *Phys. Rev. Lett.* **103**, 090601 (2009).

[146] Kubo, R. The fluctuation-dissipation theorem. *Reports Prog. Phys.* **29**, 255–284 (1966).

[147] Bochkov, G. N. *et al.* Nonlinear Fluctuation-Dissipation Relations and Stochastic Models in Nonequilibrium Thermodynamics. *Physica* **106a**, 443–479 (1981).

[148] Nyquist, B. H. Thermal Agitation of Electric Charge in Conductors. *Phys. Rev.* **3**, 110–113 (1928).

[149] Johnson, J. B. Thermal Agitation of Electricity in Conductors. *Phys. Rev.* **32**, 97–109 (1928).

[150] Callen, H. *et al.* Irreversibility and Generalized Noise. *Phys. Rev.* **83**, 34–40 (1951).

[151] Crawford, F. S. Elementary derivation of the law of equipartition of energy. *Am. J. Phys.* **55**, 180–182 (1987).

[152] Parr, R. Derivation of a Local Formula for Electron-Electron Repulsion Energy. *J. Phys. Chem.* **92**, 3060–3061 (1988).

[153] Hall, M. Valence Shell Electron Pair Repulsions and the Pauli Exclusion Principle. *Am. Chem. Soc.* **33**, 116–121 (1968).

[154] Riley, D. Lattice Constant of Diamond and the C-C Single Bond. *Nature* **155**, 587–588 (1944).

[155] Warren, R. *et al.* Spin-Lattice Relaxation of F Centers in KCl: Interacting F Centers. *Phys. Rev.* **136**, 1347–1358 (1964).

[156] Castle, J. G. *et al.* Temperature dependence of paramagnetic relaxation at point defects in vitreous silica. *J. Appl. Phys.* **36**, 124–128 (1965).

[157] Qnami diamond. URL https://qnami.ch/.

[158] Jong, T. Analysis of Nuclear Magnetic Resonance Force Microscopy. Tech. Rep., Leiden University (2014).

[159] Misra, S. *et al.* Design and performance of an ultra-high vacuum scanning tunneling microscope operating at dilution refrigerator temperatures and high magnetic fields. *Rev. Sci. Instrum.* **84**, 103903 (2013).

[160] Marz, M. *et al.* A scanning tunneling microscope for a dilution refrigerator. *Rev. Sci. Instrum.* **81**, 045102 (2010).

[161] Singh, U. R. *et al.* Construction and performance of a dilution-refrigerator based spectroscopic-imaging scanning tunneling microscope. *Rev. Sci. Instrum.* **84**, 013708 (2013).

[162] Pelekhov, D. V. *et al.* Ultralow-temperature atomic force microscopy for the investigation of mesoscopic systems. *Appl. Phys. Lett.* **72**, 993–995 (1998).

[163] Pelekhov, D. V. *et al.* Atomic force microscope for operation in high magnetic fields at millikelvin temperatures. *Rev. Sci. Instrum.* **70**, 114–120 (1999).

[164] De Wit, M. *et al.* Vibration isolation with high thermal conductance for a cryogen-free dilution refrigerator. *Rev. Sci. Instrum.* **90** (2019).

[165] Von Allwörden, H. *et al.* Design and performance of an ultra-high vacuum spin-polarized scanning tunneling microscope operating at 30 mK and in a vector magnetic field. *Rev. Sci. Instrum.* **89**, 033902 (2018).

[166] Ungar, E. E. *et al.* High-Frequency Vibration Isolation. *J. Sound Vib.* **4**, 224–241 (1966).

[167] van Waarde, B. *et al.* A magnetic persistent current switch at milliKelvin temperatures. *Cryogenics (Guildf).* **78**, 74–77 (2016).

[168] Hoekstra, F. Fridge Magnets. Tech. Rep., Leiden University (2018).

[169] Wagenaar, J. J. T. Magnetic Force Microscopy of paramagnetic electron spins in the presence of an external magnetic field. Tech. Rep., Leiden University (2013).

[170] Kerchner, H. R. *et al.* Critical fields Hc and Hc2 of superconducting niobium. *Phys. Rev. B* **24**, 1200–1204 (1981).

[171] Berman, G. P. *et al.* Quantum Dynamics of the Oscillating Cantilever-Driven Adiabatic Reversals in Magnetic Resonance Force Microscopy. *Arxiv* (2003).

[172] Hickman, S. A. *et al.* Batch-fabrication of cantilevered magnets on attonewton-sensitivity mechanical oscillators for scanned-probe nanoscale magnetic resonance imaging. *ACS Nano* **4**, 7141–7150 (2010).

[173] Sangiao, S. *et al.* Magnetic properties of optimized cobalt nanospheres grown by focused electron beam induced deposition (FEBID) on cantilever tips. *Beilstein J. Nanotechnol.* **8**, 2106–2115 (2017).

[174] Majetich, S. A. *et al.* Magnetic Nanoparticles and Magnetocrystalline Anisotropy. *Nanostructured Mater.* **9**, 291–300 (1997).

[175] Klein, O. *et al.* Ferromagnetic resonance force spectroscopy of individual submicron-size samples. *Phys. Rev. B - Condens. Matter Mater. Phys.* **78**, 144410 (2008).

[176] Kittel, C. Theory of the Structure of Ferromagnetic Domains in Films and Small Particles. *Phys. Rev.* **70**, 965–971 (1946).

[177] Kneller, E. F. *et al.* Particle size dependence of coercivity and remanence of single-domain particles. *J. Appl. Phys.* **34**, 656–658 (1963).

[178] Bean, C. P. *et al.* Superparamagnetism. *J. Appl. Phys.* **30**, 120–129 (1959).

[179] Frenkel, J. *et al.* Spontaneous and Induced Magnetization in Ferromagnetic Bodies. *Nature* **126**, 274–275 (1930).

[180] Gubin, S. *Magnetic Nanoparticles* (Wiley-VCH, 2009).

[181] Barbara, B. Single-particle nanomagnetism. *Solid State Sci.* **7**, 668–681 (2005).

[182] Longenecker, J. *et al.* Rapid serial prototyping of magnet-tipped attonewton-sensitivity cantilever by focused ion beam manipulation. *Journal of Vacuum Science & Technology B* **29**, 032001 (2011).

[183] Bautin, V. A. *et al.* Magnetic properties of polycrystalline cobalt nanoparticles. *AIP Adv.* **7**, 045103 (2017).

[184] Degen, C. L. *et al.* Nuclear spin relaxation induced by a mechanical resonator. *Phys. Rev. Lett.* **100** (2008).

[185] Braakman, F. R. *et al.* Force sensing with nanowire cantilevers. *Nanotechnology* **30**, 332001 (2019).

[186] Schmid, S. *et al. Fundamentals of Nanomechanical Resonators* (Springer, 2016).

[187] Eom, K. *et al.* Nanomechanical resonators and their applications in biological/chemical detection: Nanomechanics principles. *Phys. Rep.* **503**, 115–163 (2011).

[188] Mamin, H. J. *et al.* Sub-attonewton force detection at millikelvin temperatures. *Appl. Phys. Lett.* **79**, 3358–3360 (2001).

[189] Stowe, T. D. *et al.* Attonewton force detection using ultrathin silicon cantilevers. *Appl. Phys. Lett.* **71**, 288–290 (1997).

[190] Héritier, M. *et al.* Nanoladder Cantilevers Made from Diamond and Silicon. *Nano Lett.* **18**, 1814–1818 (2018).

[191] Rossi, N. *et al.* Supporting Information: Magnetic sensing with a self-assembled nanowire. *Nano Lett.* **19**, 930–936 (2019).

[192] Poggio, M. Sensing from the bottom up. *Nat. Nanotechnol.* **8**, 482–483 (2013).

[193] Rossi, N. *et al.* Magnetic Force Sensing Using a Self-Assembled Nanowire. *Nano Lett.* **19**, 930–936 (2019).

[194] Rossi, N. *et al.* Vectorial scanning force microscopy using a nanowire sensor. *Nat. Nanotechnol.* **12**, 150–155 (2017).

[195] Moser, J. *et al.* Ultrasensitive force detection with a nanotube mechanical resonator. *Nat. Nanotechnol.* **8**, 493–496 (2013).

[196] Chaste, J. *et al.* A nanomechanical mass sensor with yoctogram resolution. *Nat. Nanotechnol.* **7**, 301–304 (2012).

[197] Perisanu, S. *et al.* High Q factor for mechanical resonances of batch-fabricated SiC nanowires. *Appl. Phys. Lett.* **90** (2007).

[198] Nichol, J. M. *et al.* Nanomechanical detection of nuclear magnetic resonance using a silicon nanowire oscillator. *Phys. Rev. B - Condens. Matter Mater. Phys.* **85**, 054414 (2012).

[199] Ghirardi, G. C. *et al.* Relativistic Dynamical Reduction Models: General Framework and Examples. *Found. Phys.* **20**, 1271–1316 (1990).

[200] Ghirardi, G. C. *et al.* Describing the Macroscopic World: Closing the Circle within the Dynamical Reduction Program. *Found. Phys.* **25**, 5–38 (1995).

[201] Bassi, A. *et al.* Models of wave-function collapse, underlying theories, and experimental tests. *Rev. Mod. Phys.* **85**, 471–527 (2013).

[202] Ghirardi, G. C. *et al.* Unified dynamics for microscopic and macroscopic systems. *Phys. Rev. D* **34**, 470–491 (1986).

[203] Pearle, P. Combining stochastic dynamical state-vector reduction with spontaneous localization. *Phys. Rev. A* **39**, 2277–2289 (1989).

[204] McMillen, S. *et al.* Quantum-limited estimation of continuous spontaneous localization. *Phys. Rev. A* **95** (2017).

[205] Diósi, L. Testing spontaneous wave-function collapse models on classical mechanical oscillators. *Phys. Rev. Lett.* **114**, 050403 (2015).

[206] Vinante, A. *et al.* Upper Bounds on Spontaneous Wave-Function Collapse Models Using Millikelvin-Cooled Nanocantilevers. *Phys. Rev. Lett.* **116**, 090402 (2016).

[207] Collett, B. *et al.* Wavefunction Collapse and Random Walk. *Found. Phys.* **33**, 1495–1541 (2003).

[208] Cañate, P. *et al.* Continuous spontaneous localization wave function collapse model as a mechanism for the emergence of cosmological asymmetries in inflation. *Phys. Rev. D - Part. Fields, Gravit. Cosmol.* **87**, 104024 (2013).

[209] Physik instrumente. URL https://www.physikinstrumente.com/en/products/piezoelectric-transducers-actuators/p-810-p-830-piezo-actuators-100400/#description.

[210] Leo, D. *Engineering Analysis of Smart Material Systems* (Wiley, 2007).

[211] Rosen, C. *et al. Piezoelectricity* (American Institute of Physics, 1992).

[212] Fuller, C. *et al. Active Control of Vibration* (Academic Press, 1996).

[213] Martin, R. M. Piezoelectricity. *Phys. Rev. B* **5**, 1607–1613 (1972).

[214] Moheimani, S. O. A survey of recent innovations in vibration damping and control using shunted piezoelectric transducers. *IEEE Trans. Control Syst. Technol.* **11**, 482–494 (2003).

[215] Yan, B. *et al.* Shunt Damping Vibration Control Technology: A Review. *Appl. Sci.* **7**, 1–31 (2017).

[216] Gripp, J. A. *et al.* Vibration and noise control using shunted piezoelectric transducers: A review. *Mech. Syst. Signal Process.* **112**, 359–383 (2018).

[217] Aridogan, U. *et al.* A review of active vibration and noise suppression of plate-like structures with piezoelectric transducers. *J. Intell. Mater. Syst. Struct.* **26**, 1455–1476 (2015).

[218] Hagood, N. W. *et al.* Damping of structural vibrations with piezoelectric materials and passive electrical networks. *J. Sound Vib.* **146**, 243–268 (1991).

[219] Pobell, F. *Matter and methods at low temperatures* (Springer-Verlag, 1996).

[220] Hightech development leiden. URL https://hdleiden.home.xs4all.nl/index.html.